CZECH TECHNICAL UNIVERSITY IN PRAGUE

Brittle fracture of laminated glass structural elements

by

Jaroslav Schmidt

A thesis submitted in fulfillment for the
degree of Doctor of Philosophy

in the
Faculty of civil engineering
Department of mechanics

June 2023

Declaration of Authorship

I, Jaroslav Schmidt, declare that this thesis titled *Brittle fracture of laminated glass structural elements* and the work presented in it are my own. I confirm that:

- This work was done wholly or mainly while in candidature for a research degree at this University.
- Where any part of this thesis has previously been submitted for a degree or any other qualification at this University or any other institution, this has been clearly stated.
- Where I have consulted the published work of others, this is always clearly attributed.
- Where I have quoted from the work of others, the source is always given. With the exception of such quotations, this thesis is entirely my own work.
- I have acknowledged all main sources of help.
- Where the thesis is based on work done by myself jointly with others, I have made clear exactly what was done by others and what I have contributed myself.

Signed: _____

Date: _____

CZECH TECHNICAL UNIVERSITY IN PRAGUE

Abstract

Faculty of civil engineering
Department of mechanics

Doctor of Philosophy

by Jaroslav Schmidt

Many damage models have been developed over the past decades, but most of them still struggle to simulate damage without additional ad-hoc criteria or the need for difficult implementation. In particular, brittle fracture models that represent a mathematical singularity are not easy to be simulate correctly. Recently discovered phase field models prove to be advantageous in many ways. These are variationally consistent models that show a high degree of robustness. Problems such as tensile cracking, cracking of a specialized structure in 3D, crack branching or crack initiation are all described by the same set of equations. Since the model uses a regularized damage field, its implementation is also efficient. Laminated glass is a material that needs to be investigated even after cracks appear. Undamaged laminated glass is a stunning material itself, but its undisputed advantage is its cohesiveness and load-bearing capacity even in post-breakage domain. And phase-field models are suitable for simulating this residual load capacity, which allow investigating both the initiation of cracks and their branching and the impact on the structural response. This work is supposed to bring the combination of such phenomena - the simulation of laminated glass before and after the appearance of cracks. Models of different degrees of spatial reduction and structures under different loading are investigated. The work first investigates the quasi-static response of the beams, then stochastically investigates the response when the strength changes and is concluded by investigating the low-velocity impact. The paper primarly tries to create fully applicable approaches for engineering practice and reveals the benefits and shortcomings of such an approach for glass modeling.

Acknowledgements

I would like to thank a several people. Their order is chosen randomly.

I would like to thank my thesis advisor Ing. Tomáš Janda, Ph.D. The door to his office was always opened.

I would like to acknowledge unofficial supervisor-specialist Ing. Alena Zemanová, Ph.D. for her guidance through each stage of the process.

I thanks also to Prof. Ing. Jan Zeman, Ph.D. for his help with higher mathematics.

Thank to my extraordinary wife and of course this work would not have been done without the support of our guinea-pigs Chica, Missy and Minnie (which govern the household).

Finally support from by the Czech Science Foundation, the grant No. 19-15326S, is highly acknowledged.

https://doi.org/10.14311/dis.fsv.2023.008

Contents

Abbreviations

LG	**L**aminated **G**lass
FEM	**F**inite **E**lement **M**ethod
PF	**P**hase **F**ield
PF-B	**P**hase **F**ield **B**ourdin model
PF-P	**P**hase **F**ield **P**ham model
PVB	**P**oly**V**inyl **B**utyral
EVA	**E**thylene-**V**inyl **A**cetate
ODE	**O**rdinary **D**ifferential **E**quation
PDE	**P**artial **D**ifferential **E**quation
DoF	**D**egree **o**f **F**reedom
CD	**C**entral **D**ifferences
WLF	**W**illiams **L**andel **F**erry
CDM	**C**ontinuum **D**amage **M**echanics
CZM	**C**ohesive **Z**one **M**odel
VD	**V**olumetic **D**eviatoric
SD	**S**pectral **D**ecomposition
TLS	**T**hick **L**evel **S**et

Dedicated to my wife.

Chapter 1

Introduction

The aim of the thesis is the numerical investigation of the laminated glass under impact load. The topic partially follows objectives of Czech Science Foundation grant No. 19-15326S: Design and advanced modeling of forced-entry and bullet resistant glass structures. The author of thesis aims to numerically predict the post-breakage behaviour of laminated glass beams and plates and partly predict fracture patterns. Using the nowadays popular phase-field damage model seems appropriate for our goal. In the next section concept of the laminated glass is presented together with the model requirements.

1.1 What is laminated glass

Solid glass is almost perfectly elastic material suffering from fragility and practically zero post-breakage strength. The absence of the plastic yielding leads to a high stress concentration near the flaws in material under tension. It causes experimentally unpredictable strength in tension which is one order of magnitude lower than strength in compression. To improve the behavior of solid glass, especially in the post-breakable regime, and preserve the aesthetic aspect of the material, laminated glass was invented.

The laminated glass (LG) in the simplest composition consists of two glass plates and a polymer interlayer which bonds the plates together, see schematic Figure 1.1. The polymer ply transfers shear stress from one glass plate to another. With low polymer stiffness compared to glass, the result is a sandwich structure whose response ranges between the monolithic plate (two glass layers rigidly connected) and loosely stacked two plates. The improved behavior in the post-failure mode is the main advantage of the composite. Structure from solid glass is fragile and suffers from progressive collapse. LG structures have more acceptable breakdown mechanism. After breakage, contact stress between shards together with tension in undamaged ductile ply still form an integral structure which transfers the load until the damaged element is replaced. Moreover

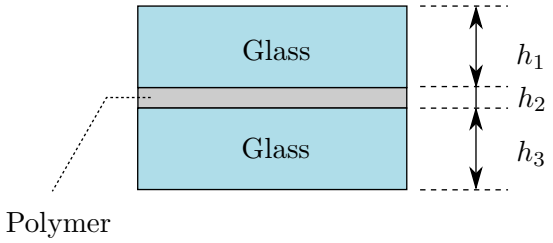

FIGURE 1.1: Schematic representation of laminated glass sample

cohesion between glass and polymer ensures integrity of the broken glass plate and thus improves safety and security of glass structure.

Despite the favorable behavior of laminated glass, it is difficult to model the behavior numerically. The most commonly used interlayer materials are PolyVinyl Butyral (PVB) or Ethylene-Vinyl Acetate (EVA), the materials with strong dependence on temperature and time. In a dynamic regime it implies angular frequency dependence and high (in comparison to glass) damping behavior. The glass also brings numerical difficulties. It is elastic material, but the microscopic flaws and defects on the surface cause stress concentration and large variation of material strength as a consequence. Moreover the glass is fragile material with almost zero process zone. These effects are not manageable by classic macroscopic FEM analysis.

1.2 Topics concerned

For modeling pre- and post-breakage response of laminated glass it is necessarily to understand several topics. Following list brings fields of interest whose state of the arts are presented in next section:

- Viscoelasticity – Glass is an almost perfectly elastic material, but unfortunately the interlayer is more complicated material. Time and temperature dependent mechanical models must be examined with focusing on the model simplicity, efficiency of implementation and possibility of extending to damage. It is also necessary to utilize experimental methods to obtain material parameters for polymer ply materials.

- Fracture – We assume that the fracture appears in the glass layers only. Cracks in brittle materials like glass have very small width of the process zone and behave as singularity without cohesion. To overcome this issue we plan to model the fracture using variationally consistent phase-field damage models. Basic idea is the regularization of the crack by spreading to an auxiliary thickness without physical meaning.

- Dynamics – Crucial aspect for the direct integration of the equations of motion is the time discretization type. The goal is to use variational integrators, which discretize the integral of action instead of governing ODE's or PDE's.
- Contact – The most critical part of modeling. To facilitate the dynamic impact simulations we plan to employ Hertz contact only. It is a simplifying assumption which generates reduction of implementation effort. Moreover, its implementation is straightforward in explicit algorithms.
- Implementation – The simulation of the laminated glass beams and plates with the fracture propagation during complex impact experiments is implemented in the finite element library FEniCS.

It is a numerically demanding process to take into account all mentioned phenomena. Therefore we restrict our attention to the dynamic regime only by considering the influence of inertia forces. The quasi-static response can be seen as a special case of the dynamic one. However, in the dynamic regime second derivatives of unknowns appear. As a consequences a different time integrators can be used and sometimes time-discrete dynamic model can be even simpler than the quasi-static one.

Chapter 2

State of the art

2.1 Laminated glass model

Although the polymer interlayer stiffness is significantly lower than that of glass, still it has a significant influence on laminated glass response. This applies in both pre- and post-breakage stages, see for example [19] on experimental investigation of different interlayers and their impact on behavior after fracture. An interesting article comparing laminated glass and solid glass with respect to reliability is presented in [21]. It is evident that the effect of interlayer in LG is crucial. In this section, the state of the art of mechanical models for layered structures is presented starting by an overview of mathematical models of the individual materials: the glass and the polymer ply.

Glass. Solid glass in pre-breakable phase is almost perfectly elastic material and it can be described by two elastic constants, for example Young's modulus E and Poisson's ratio ν. The Fracture involvement is discussed in section 2.2.

Interlayer. Polymer ply is more complex material. Its behavior in time domain is efficiently described by the theory of linear viscoelasticity [136]. The generalized Maxwell chain [17, Appendix A] is mostly employed, but it depends on interlayer material in general. The temperature dependence is more challenging, however for reasonable temperature range time-temperature superposition principle [42, Chapter 11] can be applied. The concept presumes that material has some property $\mu(t, T)$, which is time and temperature dependent. The concept binds time and temperature via multiplicative factor a expressed for reference temperature T_{R}, formally written $\mu(t, T) = \mu(a(T)t, T_{\mathrm{R}})$. Parameter $a(T)$ is a function of temperature and material constants. Experimental procedures to obtain Maxwell chain parameters of laminated glass interlayer was presented by Andreozzi in [12] or summarized in [59]. Hána, Janda et al. in [63] presented monolithic calibration of both - parameters of Maxwell chain and material constants of $a(T)$ function, where Williams–Landel–Ferry (WLF) equation [149] was employed.

Investigation of the laminated glass structures can still be a challenging process despite using the above simplifications. Analytical exact solutions appear exceptionally for their immense complexity and therefore we need to introduce further simplifications and restrictions or use numerical methods. Fortunately for some particular boundary conditions analytical solution exists. Worth mentioning as representatives is work Galuppi and Royer-Carfagni [48, 50], who presented the exact solution of a simply supported three-layer Euler-Bernoulli beam with Maxwell chain interlayer. Later they extended the same approach to study stability of columns from laminated glass [51] and behavior of cold-bent beams [52]. Also noteworthy is the recent work of Pei et al. [117]. They present similar solution as Galuppi and Royer-Carfagni but he assumes Mindlin-Reissner beam theory (first-order shear deformation theory). To our knowledge there is only the analytical solution for full elastic laminated plates [44], where several simplifying assumptions (e.g. zero bending stiffness of interlayer) are assumed.

One type of the modeling approach, where the analytical character persists but the structure is simplified, is the effective thickness approach. The name speaks for itself: Laminated units are approximated by monolithic one with effective thickness such that the selected property is the same for both systems. For example we are looking for the effective thickness of glass plate which has the same deflection as the original layered plate. Relevant example is the work of Galuppi and Royer-Carfagni on effective thickness for beams [47] and for plates [49] both in static regime. To our best knowledge, only two effective thickness approaches were presented for dynamics. The approach presented by López-Aenlle and Pelayo [3, 4] is derived from free vibration of a three-layered simply-supported beam and extended to other boundary conditions. The second one published by Zemanová [158] is enhanced dynamic effective thickness based on Galuppi and Royer-Carfagni solution [47]. Development of these easy-to-use approaches fulfills needs of engineering practice, but for complex analysis and general behavior understanding is effective thickness restrictive. The way-out may be the use of numerical models.

Viscoelastic numerical calculations using the finite element method (FEM) are common nowadays. Despite this fact, only a few full 3D calculations were published, e.g. [74, 133], due to their computational demands. To increase the numerical efficiency there is a possibility to reduce the task order. Simple beam FEM model based on Mau's [99] refined classical laminate theory [126] was introduced by Zemanová [159]. Key idea lies in kinematic description of each beam separately and enforcing displacement continuity by Lagrange multipliers. Later the work was extended to the finite-strain regime [160] and also from beams to plates [161]. Overview of these mechanical models can be found in PhD thesis [154]. Baraldi presented in [15] another possible model of laminated beams. The model built on simple assumptions and mixed formulation provides the possibility to use Euler-Bernoulli beam theory coupled with constant shear assumption across the interlayer thickness.

2.2 Approaches to fracture modeling

There exist many different approaches to crack/fracture phenomena modeling. Several common ones are:

- *Extended finite element method* (XFEM), where elements are enhanced by discontinuous field through a partition of unity method [106, 107, 137],
- Discontinuous *Cohesive zone model* (CZM) introduced by Barenblatt [16] and Dugdale [38],
- Recently proposed *Cracking elements method* (CEM), which is discontinuity embedded approach driven by local criteria [138, 164],
- *Thick level set* (TLS) approach [108, 109],
- *Peridynamics* [135],
- *Meshless/meshfree methods* [18, 113],
- Deleting elements where some threshold is exceeded, for example using Rankine stress criterion,
- and others methods or criteria [24].

All listed methods have some advantages and fields of application but mostly these are difficult to implement or they require additional criteria for crack initialization and branching. In the following text we focus only on those formulations of damage that are based on so called *continuum damage mechanics* (CDM), pioneer work of Kachanov [79, 80]. In CDM, damage is characterized by additional field $\boldsymbol{x} \mapsto d(\boldsymbol{x}) \in \langle 0, 1 \rangle$[1]. It is actually a reduction of material stiffness: when the crack fully develops in some element, the element stiffness is reduced to zero but the element itself is not modified or removed. Unfortunately, it is well-known that the application of the finite element method in CDM leads to enormous mesh dependency and the damage is localized into one band of elements [75]. To overcome unacceptable spurious localization several regularization techniques were developed. Historically the first regularized damage model was proposed by Pijaudier-Cabot and Bažant [123]. The model is called the integral-type nonlocal damage, and is based on weighted spatial averaging of internal variable. Depending on which internal variable and which weighting function is selected various models are obtained. As representative examples we provide [37].

Another significant group of regularized approaches are gradient damage models. Peerlings et al. [116] proposed regularization of local equivalent strain using expansion into a Taylor series. After local averaging and neglecting higher order terms, the equivalent strain appears to be a function of local equivalent strain and its second gradient. It

[1] In fact, the introduced field d may not be scalar, see for example [41], where second-order damage tensor is introduced. However, characterization of damage by a scalar field is the most widespread formulation.

can be understood as penalization of solutions with high gradients. Unfortunately these models suffer from spurious expansion of damage after crack initiation. Several papers were published to overcome this issue, see gradient model with variable internal length [56] or model with decreasing interactions proposed recently [124]. Nice and comprehensive comparison and overview of regularized continuum damage formulations, including also the variational damage approach discussed later, can be found in [76]. Another convenient study on localization of regularized damage models was presented in [77]. Phase field damage belongs to a family of mentioned variational brittle fracture methods, which in some way correspond to energy principles.

The foundation of the energetic approach to fracture theory lies in a famous work by Griffith [60] which introduced one of the main pillars of the crack propagation, the energy release rate and the surface energy. He stated that the crack propagates if and only if the critical value of the energy release rate is reached. The critical value is a material constant and it represents the released energy to create crack of the unit surface. Even though it was an important milestone, Francfort and Marigo [45] pointed out that Griffith's theory is an unreliable instrument to predict the crack initiation and the crack path. In an effort to avoid these limitations they introduced the variational framework of brittle fracture, where the bulk energy competes with the dissipated energy via energy minimization. The formulation still requires unfeasibly difficult implementation of the free-discontinuity problem, because of minimization over all admissible crack topologies. To overcome the numerical difficulty Bourdin suggested in [25, 26] a regularized version of the Francfort and Marigo [45] model. They presented model, which was later named *Phase-field damage model* (PF). This approach is based on work of Ambrosion and Tortorelli [9] who introduced an approximation of Mumford-Shah functional [112] for the model of image segmentation. An overview can be found in [27].

Independently, there were developed fracture phase-field models based on Ginzburg-Landau theory, see [13, 83], where the name *phase-field model of fracture* appeared. Physics community use phase-field approach for simulating phase changes and the mechanics community use the name for regularized models based on variational formulation. For a more accurate definition of these models, see comprehensive overview in [150].

Bourdin et al. [26] present their formulation as regularization of sharp crack considering Γ-convergence with decreasing length scale parameter. However regularization by Bourdin's model is not unique. Recently Wu [151] presents a unified theory in which Bourdin's model is recovered as a particular example. This unified theory was accepted by the mechanics community as *phase-field damage* and this definition still applies. Behavior of individual model depends on many factors. Five main ingredients of PF models are listed and discussed:

- Degradation function $g(d)$ – The function which appropriately degrades the element stiffness. The most common choice for degradation function is quadratic

polynomial $g(d) = (1 - d)^2$ [26]. Despite its adequate behavior and widespread use, several other degradation functions were proposed, see for example [23, 88] where cubic polynomials are used or [128] where a relatively new family of degradation functions are presented and its numerical validation is performed.

- Dissipation function – Several different models were introduced but we mention only the two most common. First is the classic formulation of Bourdin et al. [26], where the square of damage variable is employed. Main advantage of this model is approximation of the crack discontinuity by an exponential function which naturally implies the lower bound to 0. With a quadratic degradation function, which bounds damage from above by 1, we get a naturally constrained system. Unfortunately, there is no threshold and the damage starts to develop at the beginning of loading. In contrast, the formulation with a linear damage variable, firstly presented by Pham [120], has a perfectly linear elastic branch in the stress-strain diagram and the damage appears only after exceeding the energy threshold. Moreover, the associated smeared crack has finite width. The disadvantage is that the discontinuity is approximated by parabola therefore there is no self limitation of damage from below. It must be enforced additionally.

- Irreversibility – In classic materials there is no crack healing, therefore we must somehow enforce crack irreversibility $\dot{d} \geq 0$. There is always the possibility to enforce this constraint by the tools of mathematical programming [115, Chapter 16]. However, this approach does not guarantee robustness and numerical efficiency. Several simplistic approaches were presented. The most common is using the so-called *history variable* [102], which stores maximum achieved elastic tension energy. Nevertheless, a question remains whether this powerful approach is equivalent to the original one. Gerasimov at al. published another option, enforcing the irreversibility by penalization [58].

- Solver type – The PF solution is obtained through minimization of energetic functional. The functional depends on kinematic variable $\boldsymbol{u}$ and on damage d itself, therefore governing equations must be solved for both function simultaneously. This approach is referred to as the *monolithic solver* [143]. The monolithic approach suffers from divergence, because functional is non-convex with respect to both variables simultaneously. To overcome this difficulty Gerasimov and De Lorenzis [57] proposed a line-search based approach or recently Wick [147] proposed a modified Newton method for monolithic solver. Another approach is based on the fact that functionals are convex with respect to each variable separately and presents a *staggered scheme* [26]. The idea is simple: firstly kinematic function $\mathbf{u}$ is solved while damage is constant (with respect to pseudo-time) and then vice versa. Process is repeated until the solution converges. This approach is relatively robust but sometimes suffers from slow convergence. The last approach we mention is a variationaly inconsistent *hybrid formulation* [8] based on ad-hoc assumptions, which can significantly reduce numerical demands in some particular cases.

- Active/Passive decomposition – To follow real materials fracture behavior it is appropriate to model different responses in tension and in compression. This decomposition is evident in the 1D regime. In general 3D stress state it is not so obvious how to distinguish these two states. The suitable choice seems to be spectral decomposition, for phase-field proposed by Miehe [105]. Its numerical implementation remains a problem, but several theoretical decomposition algorithms were published, e.g. [66]. More appropriate approach for implementation is volumetric-deviatoric split [11], where the whole deviatoric stress and tension part of the volumetric stress are degraded by the damage and the remaining part of stress stays intact. Even simpler decomposition proposed by Lancioni et al. [90] assumes that only the deviatoric part is damaged. Other methods can be found for example in [46] or [152].

For our purposes it is important to investigate the extension of the phase-field models to the dynamics regime. This topic is still open to questions but particular results are available. To the best of our knowledge, the first reference to dynamics in the phase-field model appears in work of Larsen et al. [91] where the existence of the dynamic solution is presented. Following this work, Bourdin [28] introduced numerical implementation of the dynamic solution based on backward differences and showed particular numerical results. Works of Hofacker and Miehe [70, 71], who use Newmark time-discretization method, are also worth mentioning. All these approaches adopt the premise about unaffected kinetic energy by fracture and the assumption about rate-independent kinetic energy with respect to the crack velocity. Moreover, the models are explicit and in each time instant the damage and the kinematic variable is calculated only once. This fact is proposed ad-hoc. Better than this ad-hoc approach is to get an explicit integrator by energy minimization principle, see for example Shen et al. [134]. Integrator of Hofacker and Miehe [71] may have such form, because Newmark method is variational integrator, see next section 2.3. But it hasn't been shown yet. For comparison Chen [33] proposed a model where also the kinetic energy is degraded, specifically by the same degradation function as the elastic energy.

For numerical investigation of the laminated glass structures, a reduction to plate or beam is preferably used. Question is how to implement phase-field damage to these reduced models. One of the first proposed models was presented in [10], where the full strain energy is degraded. In [141] more accurate approach appears. Authors presume that the strain energy is decomposed to the bending and the membrane part. Membrane part was further divided based on the spectral decomposition and only tension part was degraded whereas the bending energy was damaged whole. Full decomposition across thickness was proposed by Kiendl et al. [84], but it brings implementation difficulties due to numerical integration over thickness. The recently proposed phase-field model for Euler-Bernoulli beams [89] is also valuable. In constrast to the classic formulation, the authors assume that damage is not constant across the thickness of the beam. The

position of the damaged area is an unknown parameter instead. For comparison with PF, the implementation of gradient-damage model is found in [122].

Phase-field damage approach is nowadays very popular and many extensions and applications were presented. Examples of possible applications are: extension to ductile fracture [22], PF model of fatigue [30], finite deformation implementation [22] or multi-field fracture [101, 103, 104]. Given the focus of this work, we must mention the application of PF on laminates or laminated structures: Hirshikesh [68] investigates crack propagation in composite laminates, Alessi and Freddi [5] model fracture in hybrid laminates, Khonsari [100] presents fracture of brittle thin films subjected to out-of-plane load and Baldelli et al [92] proposes the same analysis for in-plane loading. Notable innovative approach, where the system for displacements is solved by conventional finite element method meanwhile damage field is calculated using the finite volume method, is presented in [129]. Recently proposed approach [111] based on the discontinuous Galerkin method is also worth mentioning.

2.3 Integrators

In this short section a very brief overview of simple time-discretization techniques is provided.

The basic idea lies in discretization of time derivatives by finite differences, an idea originated by Leonhard Euler [40]. These traditional integrators are ad-hoc methods in the sense that they do not reflect the internal structure of governing differential equations. As a result they numerically dissipate and do not preserve invariants in general.

On the other hand, we can discretize the integral of action [97, Chapter 7] instead of governing differential equations, see [86] for classic and extended framework of stationary principle in continuum mechanics. This approach leads to so called variational integrators [93]. Integrators derived this way are symplectic, momentum conserving and exhibit good long-time energy behavior [98]. Update scheme is derived via Hamilton's principle of stationary action, therefore using discrete Lagrange-d'Alembert's equations [97, Chapter 13]. The representative of explicit variational integrators is the central differences method. Kane et al. showed that also the Newmark β method has variational structure [82], see also the work of Krenk [87] about energy conservation in the Newmark algorithm. Extension of this algorithm to viscoelastic materials described by generalized Maxwell chain was proposed by Hatada et al. [65]. It was shown that this extended integrator still preserves variational structure. Further extension from scalar regime to full 3D implementation can be done in several ways. One of them considers a rate-independent Poisson ratio. See [162] for comparison with other approaches.

Variational integrators are derived from a driving scalar functional. This is consistent with the phase-field damage approach, therefore extension of the phase-field to the dynamic regime is straightforward. Actually, Shen et al. [134] presented dynamic phase-field damage using variational integrators and as a result he get explicit solver with no internal staggered iterations. For comparison, Hofacker and Miehe [70, 71] introduced a simple explicit model for dynamic phase-field fracture. They proposed to compute the damage field only once in each time instant. However this does not stem from any physical assumption. Recently Li et al.[94] present another explicit brittle fracture model based on Newmark explicit method. This method automatically decouples the evolution system for displacement and damage. Similarly Ren [127] proposed a Verlet integration scheme accelerated by adaptive sub-stepping.

2.4 Contact

Accurate implementation of impact requires modeling and meshing of both, the impactor and the laminated glass, and considering impenetrability of the masses [78]. This task is challenging itself. It makes contact to be the critical part of the thesis and little space is devoted to it. The plan within this thesis is to use the simple spring element method [34]. Method simplifies the contact considering that the impactor is an additional degree of freedom connected to the point of impact by a spring with prescribed stiffness function. For this function Hertz law [67] is mostly adopted. Another method presented in [34] is the lumped mass method, but it works sufficiently only if the impactor's weight is orders of magnitude greater than the weight of the laminated glass plate.

2.5 Laminated glass damage

Investigation of laminated glass behavior under impact requires involvement of all mentioned aspects, which makes analysis demanding and complex. Many possible approaches give rise to a large number of publications on this topic, especially with the focus on automobile industry application. The list of articles is not definitely comprehensive and only some representatives are listed.

In the pre-breakage regime, response of laminated glass loaded by impact can be captured by basic models (see section 2.1) extended by impact and time integrator, see interesting study of soft impact implemented in FEM software ABAQUS in [110]. Thematic example is the paper by Del Linz et al. [36], where the pseudo analytical solution of LG plates loaded by a heavy blast explosion is introduced. The solution is obtained using the Galerkin method with trigonometric series. Moreover authors present an analytical approach to crack density evaluation. More challenging is the description of post-breakage behavior of this material. It is almost impossible to obtain a close-form

analytical solution. Worth mentioning is the work of Galuppi and Royer-Carfagni [53] where a mechanical fracture-homogenized model for LG in tension is introduced. This model assumes that the glass is fragmented into a known number of pieces and partial delamination occurs in cracks surroundings. Post-breakage behavior is then driven by the effective stress field obtained by the variational approach. The same authors extend this work in [54], where the mechanical model for LG in bending mode is introduced. Two bending modes are presented: In-plane and Out-of-plane bending. In the former case they suppose that only the glass respond in compressive part of the cross section, whereas the interlayer stiffened by glass fragments acts in tension. Tension modulus is obtained by homogenization mentioned earlier [53]. The latter case assumes that tension is transferred via the interlayer only and the compression is carried by the glass fragments contacts. This approach is similar to the one used for the reinforced concrete design.

To capture the fracture patterns and the cracks initiation, we must employ numerical methods. The conventional choice is to use the finite element method (FEM). An example of this approach is [165], where the authors investigate the damage of the laminated automotive glazing impacted by head. A continuum damage mechanics with anisotropic damage tensor is used and PVB is modeled as elastic material under small-strain assumption. In contrast Timmel [140] presents work, where hyperelasticity for PVB is employed, specifically the Blatz-Ko law. In this case the fracture is obtained by deleting elements, which exceed the given stress threshold. The procedure implementation is efficient, but suffers from intense mesh dependency. Partial improvement can be found in [118], where introduction of short plastic phase suppresses unstable stress wave propagation after element removal. Moreover, the author enhanced the model by tiebreak contact with an additional cohesive zone for delamination. Unfortunately, this model still remains mesh dependent. Recently, Alter et al. [7] presented a non-local failure criterion for element deletion which eliminates the mesh dependency. Another approach for fracture modeling of laminated glass is the extended finite element method (XFEM), see work of Xu et al. [153] who employ this method. Disadvantage of the approach is that the implementation in 3D and managing the crack branching is difficult. Numerical investigation of post-breakage behavior of laminated glass can be also performed using the cohesive zone model (CZM), see implementation for impact of automotive windshield glazing in [95]. Authors implemented hyperelastic Mooney-Rivlin law for PVB interlayer and loaded the plate by headform impactor. Although there is no dependence of the mesh on contact force, the mesh-dependence appears in the crack patterns. Review of mention methods with numerical examples can be found in [31]. Worth mentioning is also the work of Wang et al. [144], where an interesting comparison of the finite element method, the extended finite element method, the discrete element method and combined finite-discrete element method in capability to predict fracture pattern is published. Despite the fact that analyses are performed on solid glass only and under plane stress assumption, the results exemplifies possibilities of individual methods. From

the work point-of-view the combined finite-discrete element method (FEM/DEM) wins since it predicts the most reasonable patterns. Recently Wang et al. [145] extended the analysis on laminated glass. Plane stress impact is considered and only FEM/DEM approach is employed. The interlayer is modeled as Mooney-Rivlin material and the cohesive zone model for delamination is used. In [119] we can found a numerical treatment of delamination process and its comparison with experiments.

Chapter 3

Phase field formulation of brittle fracture

3.1 Variational approach to brittle fracture

As was mentioned in Chapter 2, first variational description of brittle fracture comes from Francfort and Marigo [45]. They pointed out that Griffith theory is insufficient for crack initialization. It can be seen from simple thought. Consider elasticity planar problem loaded by $\hat{\sigma}$ with inner crack of length l. Fracture mechanics say that stress intensity factor K_I in a neighborhood of crack tip is $\hat{\sigma}\sqrt[2]{l}$. By formula $G = K_I^2/E$ we get energy release rate G of order $\hat{\sigma}^2 l$. Griffith criterion immediately implies that the stress field $\hat{\sigma}$ must be $1/\sqrt[2]{l}$. It is inconvenient for prediction of crack initialization because as $l \to 0$ then the required stress goes to infinite, $\hat{\sigma} \to \infty$. In absence of initial crack the model is not able to handle crack initialization. Francfort and Marigo proposed variational framework to overcome the shortcoming of Griffith approach, i.e. displacement field $\boldsymbol{u}(\boldsymbol{x})$ and crack topology $\Gamma(\boldsymbol{x})$ are obtained as minimizer

$$(\boldsymbol{u}(\boldsymbol{x}), \Gamma(\boldsymbol{x})) = \underset{(\hat{\boldsymbol{u}}, \hat{\Gamma}) \in \mathcal{U} \times \mathcal{G}}{\arg\min} \{\mathcal{E}(\hat{\boldsymbol{u}}(\boldsymbol{x}), \hat{\Gamma}(\boldsymbol{x}))\} \tag{3.1}$$

of following energetic functional

$$\mathcal{E}(\boldsymbol{u}(\boldsymbol{x}), \Gamma(\boldsymbol{x})) = \int_{\Omega \setminus \Gamma} \psi_{\mathrm{e}}(\nabla_{\mathrm{s}} \boldsymbol{u}(\boldsymbol{x}))\, \mathrm{d}V + \int_{\Gamma} k(\boldsymbol{x})\, \mathrm{d}\mathscr{H}^{N-1}. \tag{3.2}$$

The above notation needs some clarification. We consider continuous domain $\Omega \subset \mathbb{R}^N$ with $N \in \{1, 2, 3\}$, where displacement field $\boldsymbol{u}(\boldsymbol{x})$ and $(N-1)$-dimensional fracture topology $\Gamma(\boldsymbol{x})$ are realized. Value $\mathscr{H}^{\delta}$ represents δ-dimensional Hausdorff measure and $k(\boldsymbol{x})$ is fracture toughness. The first term in functional (3.2) represents the bulk energy, so ψ_{e} is the energy density depending on the symmetric gradient of displacements. The spaces $\mathcal{U}$ and $\mathcal{G}$ are set of kinematically admissible displacements and set of topologically

admissible crack, respectively. They are defined as

$$\mathcal{U} = \{\boldsymbol{u} \in W^{1,2}(\Omega \setminus \Gamma), \boldsymbol{u}(\boldsymbol{x}) = \bar{\boldsymbol{u}} \ \ \forall \boldsymbol{x} \in (\partial\Omega \setminus \Gamma)\} \tag{3.3}$$

$$\mathcal{G} = \{\Gamma \subset \bar{\Omega}, \mathscr{H}^{N-1}(\Gamma) < \infty\} \tag{3.4}$$

where $W^{1,2}(\Omega \setminus \Gamma)$ is the Sobolev space of functions with square-integrable weak derivatives and $\bar{\boldsymbol{u}}$ is a prescribed function of the Dirichlet boundary condition.

Minimizer of (3.1) is a steady-state solution. For quasi static analysis driven by monotonously increasing pseudo time parameter t, we consider no crack healing enforced by irreversibility condition

$$\Gamma(\boldsymbol{x}, t) \supseteq \Gamma(\boldsymbol{x}, s), \forall t \geq s. \tag{3.5}$$

Actually, crack evolution is restricted by further conditions but deeper analysis of the model is beyond the scope of the work, see [45]. In what follows we consider constant fracture toughness $k(\boldsymbol{x}) = G_\mathrm{f}$. Resulting governing variational framework is summarized in the following box, where irreversibility is formulated in Hausdorff measures.

Variational brittle fracture

$$(\boldsymbol{u}(\boldsymbol{x}, t), \Gamma(\boldsymbol{x}, t)) = \underset{(\hat{\boldsymbol{u}}, \hat{\Gamma}) \in \mathcal{U} \times \mathcal{G}}{\arg\min} \{\mathcal{E}(\hat{\boldsymbol{u}}(\boldsymbol{x}, t), \hat{\Gamma}(\boldsymbol{x}, t))\} \tag{3.6}$$

$$\mathcal{E}(\boldsymbol{u}(\boldsymbol{x}, t), \Gamma(\boldsymbol{x}, t)) = \int_{\Omega \setminus \Gamma} \psi_\mathrm{e}(\nabla_\mathrm{s} \boldsymbol{u}(\boldsymbol{x}, t), \Gamma(\boldsymbol{x}, t)) \, \mathrm{d}V + G_\mathrm{f} \mathscr{H}^{N-1}(\Gamma(\boldsymbol{x}, t)) \tag{3.7}$$

$$\mathscr{H}^{N-1}(\Gamma(\boldsymbol{x}, t)) \geq \mathscr{H}^{N-1}(\Gamma(\boldsymbol{x}, s)), \forall t \geq s \tag{3.8}$$

Remark 3.1. This model is based on famous article from Francfort and Marigo [45], where only quasi static analysis is presented, inertial forces are neglected. This formulation serves as kind of motivation for phase-field model and inertia forces are introduce later.

Remark 3.2. In the rest of the work, the explicit dependence of quantities on spatial variables is omitted. We believe that this will not bring any misunderstandings and, moreover, it will improve the clarity of mathematical equations. E.g. the expression $\mathcal{E}(\boldsymbol{u}(\boldsymbol{x}, t), \Gamma(\boldsymbol{x}, t))$ is simplified to $\mathcal{E}(\boldsymbol{u}, \Gamma)$ or $\mathcal{E}(\boldsymbol{u}, \Gamma, t)$ depending on the context.

Remark 3.3. This work is not a pure mathematical text and the investigation of the existence and uniqueness of the solution is beyond the scope of the thesis. For this reason, the text avoids the specification of individual spaces and other mathematical details. Instead, in the following text, admissible fields are introduced without further mathematical specification.

Remark 3.4. In this chapter we investigate physical continuum, therefore the case $N = 3$ is used exclusively.

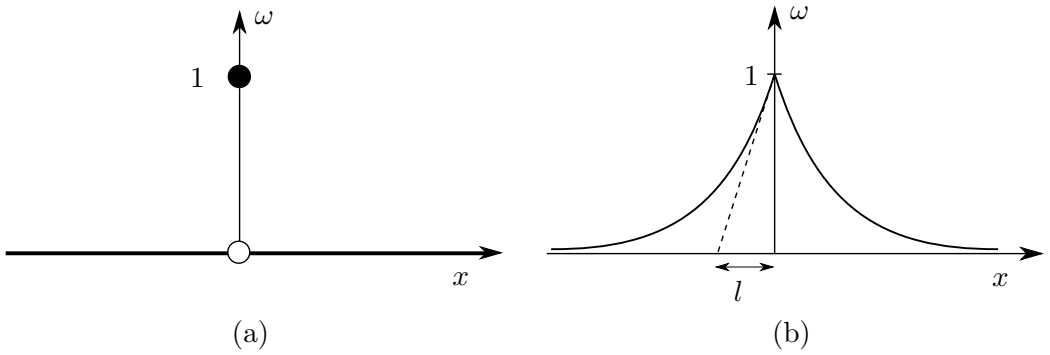

FIGURE 3.1: Sharp crack represented by discontinuity (a) and smeared regularized crack (b)

3.2 Regularization of energy functional

The main drawback of the variationally consistent model (3.6)-(3.8) is impossibility of straightforward numerical implementation. When we know the crack path a priori, we can parameterize it by scalar parameter, e.g. the length l. In this case, the implementation of minimizing problem is still feasible and we are looking for minimizing displacement field $\boldsymbol{u}$ and the actual length of crack l. Unfortunately, the path of the crack is usually not known in advance, and moreover, by prescribing it, we prevent its branching and development in another place. Thus in general, the set of topologically admissible cracks counts an infinite number of different topologies and we do not yet know an effective way to search it through effectively.

The combination of continuous regularization and damage mechanics principle can be used to overcome this issue. The sharp crack from Figure 3.1a is replaced by the regularized continuous damage field d, which characterizes the state of the material, see Figure 3.1b. Here $d = 0$ corresponds to an intact material and $d = 1$ to a fully cracked material. The regularization of sharp fracture energy is not unique. The original phase-field damage model (PF) [25, 26] is based on work of Ambrosion and Tortorelli [9] approximation of Mumford-Shah functional [112], but nowadays phase-field damage model represents whole family of models presented by Wu [151]. This general regularization takes the form

$$G_{\mathrm{f}} \int_{\Gamma} \mathrm{d}\mathscr{H}^2 \approx \frac{G_{\mathrm{f}}}{c_\alpha} \int_{\Omega} \frac{1}{l_{\mathrm{c}}} \alpha(d) + l_{\mathrm{c}} |\nabla d|^2 \,\mathrm{d}V = \int_{\Omega} \psi_{\mathrm{d}} \,\mathrm{d}V = \Psi_{\mathrm{d}}(d), \tag{3.9}$$

where α is dissipation function, which governs properties of individual models and l_{c} is length-dimension parameter which is linked to crack thickness. Finally c_α is model constant bound directly to function α as $c_\alpha = 4 \int_0^1 \sqrt{\alpha(\xi)} \,\mathrm{d}\xi$. In PF models the elastic energy must be also adjusted. Instead of excluding the crack topology from the elastic domain, the energy is defined over whole body, but is degraded by degradation function

$g(d)$. The phase-field elastic accumulated energy is therefore

$$\Psi_{\mathrm{e}}(\boldsymbol{u}, d) = \int_{\Omega} g(d)\psi_{\mathrm{e}}(\boldsymbol{\varepsilon}). \tag{3.10}$$

The strain $\boldsymbol{\varepsilon}$ is defined as symmetric gradient of displacement field $\boldsymbol{\varepsilon} = \nabla_{\mathrm{s}}\boldsymbol{u}$. The degradation function can be of arbitrary shape, but we will use exclusively the relation $g(d) = (1-d)^2$ in this work. It has advantageous properties that naturally holds the damage field less than or equal to one and, in combination with a suitable α function, has other suitable properties. The formulation (3.10) is quite efficient, but does not have the required physical properties. Real materials such as glass usually have significantly lower tensile strength than strength in compression. We must take this fact into account in the models. The elastic energy must be divided into active and passive part and only the active part is degraded, while the passive part is left intact, i.e.

$$\Psi_{\mathrm{e}}(\boldsymbol{u}, d) = \Psi^{+}(\boldsymbol{u}, d) + \Psi^{-}(\boldsymbol{u}) = \int_{\Omega} g(d)\psi_{\mathrm{e}}^{+}(\boldsymbol{\varepsilon}) + \psi_{\mathrm{e}}^{-}(\boldsymbol{\varepsilon})\,\mathrm{d}V. \tag{3.11}$$

Several types of decomposition appears in literature, but we utilizes only two of them: volumetric-deviatoric split (VD) and principal strain decomposition called spectral decomposition (SD) in literature, see Table 3.1, where K, λ, μ stands for bulk modulus and Lame's coefficients respectively. Further $\boldsymbol{\varepsilon}_{\mathrm{D}}$ is the deviatoric strain part and $\boldsymbol{\varepsilon}^{\pm}$ are positive and negative strain parts from spectral decomposition. It can be expressed by principal strains ε_i and eigenvectors $\boldsymbol{p}_i$ as $\boldsymbol{\varepsilon}^{\pm} = \sum_i \pm\langle\pm\varepsilon_i\rangle \boldsymbol{p}_i \otimes \boldsymbol{p}_i$. Finally the Macaulay brackets are defined as $\langle a\rangle = \big(a + |a|\big)/2$.

Split	$\psi_{\mathrm{e}}^{+}(\boldsymbol{\varepsilon})$	$\psi_{\mathrm{e}}^{-}(\boldsymbol{\varepsilon})$
VD	$K/2\langle \mathrm{tr}(\boldsymbol{\varepsilon})\rangle^2 + \mu\boldsymbol{\varepsilon}_{\mathrm{D}} : \boldsymbol{\varepsilon}_{\mathrm{D}}$	$K/2\langle -\mathrm{tr}(\boldsymbol{\varepsilon})\rangle^2$
SD	$\lambda/2\langle \mathrm{tr}(\boldsymbol{\varepsilon})\rangle^2 + \mu\boldsymbol{\varepsilon}^{+} : \boldsymbol{\varepsilon}^{+}$	$\lambda/2\langle -\mathrm{tr}(\boldsymbol{\varepsilon})\rangle^2 + \mu\boldsymbol{\varepsilon}^{-} : \boldsymbol{\varepsilon}^{-}$

TABLE 3.1: Strain energy decompositions: volumetric-deviatoric split (VD) and spectral decomposition (SD).

The last ingredient is the work of body forces $\boldsymbol{b}$ and external forces $\boldsymbol{t}$ acting on part of boundary $\partial\Omega_t \subseteq \partial\Omega$ given by

$$\mathcal{P}(\boldsymbol{u}) = \int_{\Omega} \boldsymbol{b}\cdot\boldsymbol{u}\,\mathrm{d}V + \int_{\partial\Omega_t} \boldsymbol{t}\cdot\boldsymbol{u}\,\mathrm{d}A. \tag{3.12}$$

Now, the quasi static variational regularized problem is formulated as searching for displacement field $\boldsymbol{u}$ and damage field d, which minimize total energy $\Psi_{\mathrm{e}} + \Psi_{\mathrm{d}} - \mathcal{P}$ and satisfy irreversibility condition for d, i.e.

Variational regularized fracture	
$(\boldsymbol{u}(t), d(t)) = \underset{(\hat{\boldsymbol{u}},\hat{d})\in\mathcal{U}\times\mathcal{D}}{\arg\min}\ \{\mathcal{E}(\hat{\boldsymbol{u}}(t), \hat{d}(t))\}$	(3.13)
$\mathcal{E}(\boldsymbol{u}, d) = \Psi_{\mathrm{e}}(\boldsymbol{u}, d) + \Psi_{\mathrm{d}}(d) - \mathcal{P}(\boldsymbol{u})$	(3.14)
$\dot{d} \geq 0$	(3.15)

Remark 3.5. This formulation remains quasistatic in the sense that individual minimization is performed in each time instant. The only equation, where time plays an important role, is the irreversibility condition.

Remark 3.6. The dot $\dot{\square}$ represents the differentiation of field $\square$ with respect to time t.

3.2.1 Governing equations

The unknown displacements and phase-field damage parameters are found by minimizing the energy functional in Eq. (3.14) complemented with boundary conditions. Thus, the governing equations describing the displacement sub-problem follow from Eq. (3.14) by taking variation with respect to $\boldsymbol{u}$,

$$\begin{aligned} \nabla \cdot \boldsymbol{\sigma} + \boldsymbol{b}^* &= \boldsymbol{0} \qquad \text{in } \Omega, \\ \boldsymbol{\sigma} \cdot \boldsymbol{n} &= \boldsymbol{t}^* \qquad \text{on } \partial\Omega_t, \end{aligned} \tag{3.16}$$

where $\boldsymbol{n}$ is the outward unit normal vector to the boundary $\partial\Omega$. The stress field is given by

$$\boldsymbol{\sigma} = g(d)\, \frac{\partial \psi_{\mathrm{e}}^{+}(\boldsymbol{\varepsilon}(\boldsymbol{u}))}{\partial \boldsymbol{\varepsilon}} + \frac{\partial \psi_{\mathrm{e}}^{-}(\boldsymbol{\varepsilon}(\boldsymbol{u}))}{\partial \boldsymbol{\varepsilon}}\,. \tag{3.17}$$

The phase-field sub-problem yields the damage evolution equation and the corresponding Neumann boundary condition

$$\left.\begin{aligned} \frac{1}{c_\alpha}\left(\frac{\mathrm{d}\alpha(d)}{\mathrm{d}d} - 2l_{\mathrm{c}}^2\Delta d\right) &= -\frac{1}{2}\frac{\mathrm{d}g(d)}{\mathrm{d}d}\tilde{Y} \qquad \dot{d} > 0 \\ \frac{1}{c_\alpha}\left(\frac{\mathrm{d}\alpha(d)}{\mathrm{d}d} - 2l_{\mathrm{c}}^2\Delta d\right) &> -\frac{1}{2}\frac{\mathrm{d}g(d)}{\mathrm{d}d}\tilde{Y} \qquad \dot{d} = 0 \end{aligned}\right\} \quad \text{in } \Omega,$$

$$\left.\begin{aligned} \tfrac{G_{\mathrm{f}}}{c_\alpha} 2l_{\mathrm{c}}\nabla d \cdot \boldsymbol{n} &= 0 \qquad \dot{d} > 0 \\ \tfrac{G_{\mathrm{f}}}{c_\alpha} 2l_{\mathrm{c}}\nabla d \cdot \boldsymbol{n} &> 0 \qquad \dot{d} = 0 \end{aligned}\right\} \quad \text{on } \partial\Omega, \tag{3.18}$$

where Δ is the Laplace operator, $\dot{d}$ denotes the damage rate, i.e. the derivative of the phase-field variable with respect to a (pseudo)time and $\tilde{Y}$ is a normalized effective damage/crack driving force.

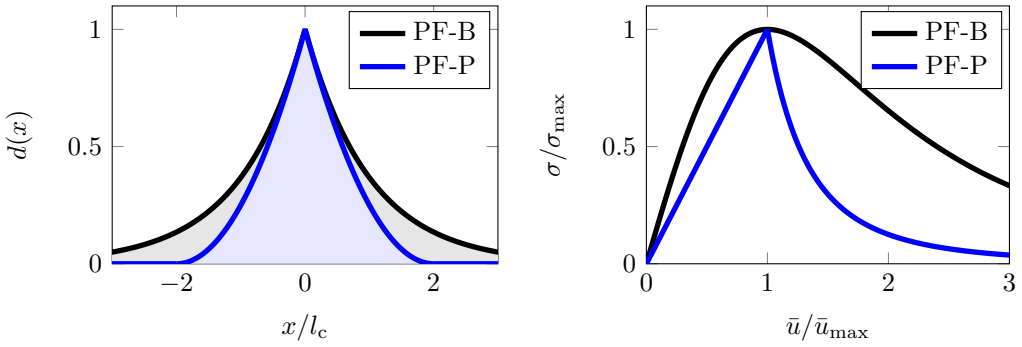

(a) (b)

FIGURE 3.2: Damage profiles for two different geometric crack functions (a) and stress evolution diagrams (b) corresponding to a one-dimensional localized solution of an infinite bar under tension, for the Bourdin (PF-B) and Pham (PF-P) model.

3.2.2 Variationally consistent models

Different damage models can be derived from this general formulation by a different choice of the geometric function α and the degradation function g, or by modification of the normalized effective crack driving force $\tilde{Y}$. If no modification is performed, therefore crack driving force $\tilde{Y}$ remains

$$\frac{2\psi_e^+(\boldsymbol{\varepsilon}(\boldsymbol{u}))}{G_f/l_c}, \tag{3.19}$$

then these models are variationally consistent. We investigate two of them.

Model proposed by Bourdin [26] was historically the first phase field model. It assumes quadratic dissipation function $\alpha(d) = d^2$ which induces $c_\alpha = 2$. This model is denoted as PF-B in what follows. The main advantage of this model is that it naturally constrains the damage field from below by zero. In combination with the quadratic degradation function $(1-d)^2$, it is an effective model, because at that moment the solution of the damage equation leads to a linear weak form without inequalities constraints. This behavior is easily observable in 1D example, where damage $d = 1$ is prescribed in point $x = 0$. Exponential solution is visualized by black in Figure 3.2a. A small inconvenience can be infinite support of damage function, i.e. crack is developing in whole domain. Moreover the damage evolves immediately at the onset of the loading. It can be seen from stress evolution diagram of simple tension-compression test, where missing linear response, see Figure 3.2b.

Model proposed by Pham [120] is based on dissipation function $\alpha(d) = d$ and $c_\alpha = 8/3$ and denoted as PF-P is this thesis. The preservation of the linear branch in the force-displacement diagram, and thus the development of damage only after the damage criterion is satisfied, is the main advantage of this model. Despite the fact that

integrated dissipated energy is roughly the same for PF-P and PF-B, this model exhibits more physical behavior with respect to brittle materials due to the linear branch and also because the support of the damage function is finite, see Figure 3.2. Drawback of PF-P model is that d solution is not restricted from below and therefore it is necessary to use variational inequality constrained solver.

3.2.3 Variationally inconsistent models

Using driving crack force (3.19) the presented models are variationally consistent in the sense that the behavior of structure is determined directly by the minimization process. Nevertheless this term can be replaced with arbitrary ad hoc function without relation to the variational problem. The main function for variationaly inconsistent phase-field model used in this thesis is the modified Rankine-based stress criterium, i.e.

$$Y = \zeta \left\langle \sum_{i=1}^{3} \left(\frac{\langle \sigma_i \rangle}{f_{\mathrm{t}}} \right)^2 - 1 \right\rangle, \tag{3.20}$$

where σ_i is principal stress and f_{t} is tensile strength. Parameter ζ multiplies the driving force after failure and limit case $\zeta \to \infty$ recovers the perfectly brittle material. This approach is advantageously used for beam and plates model, see equation (4.18) in Section 4.1.

3.2.4 Implementation/Numerical solving

The phase field damage model in quasi-static regime is now fully described and now it remains to supply implementation details. The finite element method (FEM) is nowadays the best approach for solving such task, therefore the computational library FEniCS [6] was used, because it offers an efficient python interface. This makes all the codes available on a free gitlab repository [73]. Other successful applications of the phase-field fracture in the framework of FEniCS can be found in [20, 69], where other codes are also accessible.

Two fields d and $\boldsymbol{u}$ are coupled and the monolithic approach, i.e. minimizing w.r.t. d and $\boldsymbol{u}$ simultaneously, is the most direct way to solve the problem. Nevertheless using such an approach leads to a solver that is poorly robust. Therefore, in this work we exclusively use the staggered approach, which solve a weak forms for displacement and for damage independently and alternates between them until it converges. The advantage is that each sub-problem is convex and robustness is observed. Due to some difficulties in solving displacements due to decomposition (3.11), we also present a so-called hybrid staggered model, where decomposition is considered only in the calculation of damage, but the elastic energy during $\boldsymbol{u}$-minimization is completely degraded without the use of decomposition.

Our implementation strategy for the anisotropic and hybrid staggered approach are outlined in Algorithms 1 and 2 to better understand the methods. For both algorithms, we update the phase-field parameter with the FEniCS-SNES solver, based on a semi-smooth Newton method for variational inequalities, to ensure that the parameter d cannot decrease in time and stays within the admissible $\langle 0, 1\rangle$ interval. Additionally, the iterations with a time-step are terminated using the energy convergence control with the tolerance of $\xi_{\mathrm{SA}} = 10^{-6}$. Notice that the displacement sub-problem in the anisotropic staggered scheme (Algorithm 1) involves iterative energy minimisation using the Newton method with the relative tolerance $\xi_{\mathrm{NM}} = 10^{-11}$, whereas the same step in Algorithm 2 results in a linear problem.

Algorithm 1: Anisotropic staggered approach

Data:
set staggered approach tolerance ξ_{SA};
set Newton method tolerance ξ_{NM};
for $t \in \{t_0, \ldots, t_{\mathrm{end}}\}$ **do**
  while $\xi^{(i)} > \xi_{\mathrm{SA}}$ **do**
    get $\mathbf{u}_t^{(i)}$ by minimisation of $\mathcal{E}^{(i)}$ from (3.14) w.r.t. $\mathbf{u}$ using Newton method with tolerance ξ_{NM};
    get $d_t^{(i)}$ by iterative minimisation of $\mathcal{E}^{(i)}$ from (3.14) w.r.t. d using FEniCS-SNES solver;
    update $\mathcal{E}^{(i)} \leftarrow \mathcal{E}(\mathbf{u}_t^{(i)}, d_t^{(i)})$;
    update $\xi^{(i)} \leftarrow |\mathcal{E}^{(i)} - \mathcal{E}^{(i-1)}|/\mathcal{E}^{(i)}$;
    update $i \leftarrow i + 1$;
  end
end

Algorithm 2: Hybrid (isotropic-anisotropic) staggered approach

Data:
set staggered approach tolerance ξ_{SA};
for $t \in \{t_0, \ldots, t_{\mathrm{end}}\}$ **do**
  while $\xi^{(i)} > \xi_{\mathrm{SA}}$ **do**
    get $\mathbf{u}_t^{(i)}$ from linear problem given by minimisation of $\mathcal{E}^{(i)}$ from (3.14) with no split (3.10) w.r.t. $\mathbf{u}$;
    get $d_t^{(i)}$ by minimisation of $\mathcal{E}^{(i)}$ from (3.14) w.r.t. d using FEniCS-SNES solver;
    update $\mathcal{E}^{(i)} \leftarrow \mathcal{E}(\mathbf{u}_t^{(i)}, d_t^{(i)})$;
    update $\xi^{(i)} \leftarrow |\mathcal{E}^{(i)} - \mathcal{E}^{(i-1)}|/\mathcal{E}^{(i)}$;
    update $i \leftarrow i + 1$;
  end
end

3.2.5 Parameters for the phase-field models and their relation

For the numerical analysis, we present in this section material parameters needed to predict the crack initiation and propagation in material. The elastic properties are often known, but the phase-field fracture formulation contains two additional parameters which have to be specified, i.e., the fracture energy G_f and the length-scale parameter l_c.

In this thesis we investigate the fracture of glass. A typical value of the fracture energy $G_\mathrm{f} = 4$ J·m^{-2} for soda-lime-silica glass can be found in the literature [144, 148] and tensile strength of glass can be estimated according to standards [1] as $f_\mathrm{t} = 45$ MPa. Then, the corresponding length-scale parameter l_c seen as a material parameter can be estimated. For illustration, we adopt the following analytical expressions,

$$l_\mathrm{c} = \frac{27}{256}\frac{EG_\mathrm{f}}{f_\mathrm{t}^2} \qquad \text{for PF-B model [27, 121, 163]}, \tag{3.21}$$

$$l_\mathrm{c} = \frac{3}{8}\frac{EG_\mathrm{f}}{f_\mathrm{t}^2} \qquad \text{for PF-P model [114, 150]}, \tag{3.22}$$

derived from spatially homogeneous solutions of the one-dimensional quasi-static problems. This results in a very small length-scale parameter of about 10 μm for glass, and therefore, leads to a very fine mesh and excessive computational costs for our real-size samples or glass panels in structural glass facades. For this reason, we decided to treat the length scale as a numerical parameter and to derive the corresponding fracture energy from Eqs. (3.21) and (3.22). For example, the fracture energies corresponding to the length-scale parameter of 3 mm can be seen in Table 3.2. This way, the length-scale parameter can be set according to the mesh density, and the fracture energy can be adjusted for the simulation.

	G_f [146] [J·m^{-2}]	$l_\mathrm{c} = \frac{27}{256}\frac{EG_\mathrm{f}}{f_\mathrm{t}^2}$ [mm]	$l_\mathrm{c} = \frac{3}{8}\frac{EG_\mathrm{f}}{f_\mathrm{t}^2}$ [mm]	$G_\mathrm{f} = \frac{256}{27}\frac{f_\mathrm{t}^2 l_\mathrm{c}}{E}$ [J·m^{-2}]	$G_\mathrm{f} = \frac{8}{3}\frac{f_\mathrm{t}^2 l_\mathrm{c}}{E}$ [J·m^{-2}]
material parameter	4	0.010	0.036		
numerical parameter		3	3	823	231

TABLE 3.2: Link between the fracture energy G_f and the length-scale parameter l_c seen as material or numerical parameter using the Young modulus $E = 70$ GPa and the tensile strength for annealed glass $f_\mathrm{t} = 45$ MPa from [1]

3.3 Dynamic phase field fracture

The models presented in previous sections were quasi static in the sense, that inertia forces was neglected. In this Section we extend phase field models to dynamic regime to take these forces into account.

3.3.1 Formulation

For dynamical systems, the common principle of minimum potential is replaced by Hamilton's principle of stationary action and fields $\boldsymbol{u}(t)$ and $d(t), t \in \langle 0, T\rangle$ are obtained by minimization of action integral

$$\mathcal{A}(\boldsymbol{u}, \dot{\boldsymbol{u}}, d) = \int_0^T \mathcal{L}(\boldsymbol{u}, \dot{\boldsymbol{u}}, d)\,\mathrm{d}t, \tag{3.23}$$

where $\mathcal{L}$ is so called Lagrangian which form is postulated as

$$\mathcal{L}(\boldsymbol{u}, \dot{\boldsymbol{u}}, d) = \mathcal{K}(\dot{\boldsymbol{u}}) - \Psi_{\mathrm{e}}(\boldsymbol{u}, d) - \Psi_{\mathrm{d}}(d) + \mathcal{P}(\boldsymbol{u}), \tag{3.24}$$

where $\mathcal{K}$ is kinetic energy defined as quadratic form of displacement field

$$\mathcal{K}(\dot{\boldsymbol{u}}) = \int_\Omega \frac{1}{2}\rho\dot{\boldsymbol{u}} \cdot \dot{\boldsymbol{u}}\,\mathrm{d}\boldsymbol{x}. \tag{3.25}$$

This formulation assumes that kinetic energy is not affected by damage, therefore the functional is d-independent, which ensures mass conservation. Three more terms in equation (3.24) are elastic potential, dissipated energy and external work of traction forces with the same definitions as in the quasi static case.

The variational consistent approach to dynamic phase-field damage can be summarized by following box:

Dynamic phase field fracture

$$(\boldsymbol{u}(t), d(t)) = \underset{(\hat{\boldsymbol{u}},\hat{d})\in\mathcal{U}\times\mathcal{D}\times\mathcal{I}}{\arg\min} \left\{ \int_0^T \mathcal{L}(\hat{\boldsymbol{u}}(t), \dot{\hat{\boldsymbol{u}}}(t), \hat{d}(t))\,\mathrm{d}t \right\} \tag{3.26}$$

$$\mathcal{L}(\boldsymbol{u}, \dot{\boldsymbol{u}}, d) = \mathcal{K}(\dot{\boldsymbol{u}}) - \Psi_{\mathrm{e}}(\boldsymbol{u}, d) - \Psi_{\mathrm{d}}(d) + \mathcal{P}(\boldsymbol{u}) \tag{3.27}$$

$$\dot{d} \geq 0 \tag{3.28}$$

3.3.2 Numerical integrators

First of all we suppose that the solution is evaluated only in discrete time instants $0 = t_0 < t_1 < t_2 < \ldots < t_N = T$ selected from the original time interval $\langle 0, T\rangle$. The action integral (3.23) is approximated based on this time discretization as

$$\sum_{i=0}^{N-1} \Delta t_i \mathcal{L}_{\mathrm{d}}(\boldsymbol{u}_i, \boldsymbol{u}_{i+1}, d_i, d_{i+1}), \tag{3.29}$$

where common notation $\boldsymbol{u}_i = \boldsymbol{u}(t_i)$ and $d_i = d(t_i)$ is used and also $\Delta t_i = t_i - t_{i-1} = \Delta t$ is supposed to be constant. Function $\mathcal{L}_{\mathrm{d}}$ is discretized Lagrangian, which approximate the action integral on a given sub-interval. The following procedure depends whether

the discrete variational principle (3.29) is followed. Integrators derived from the discrete variation principle have more promising properties, but on the other hand it is not always advantageous to follow the principle.

3.3.2.1 Semi explicit solver

The form of discrete Lagrangian determines the type of integrator. In this section we want to derive semi explicit integrator in the sense that displacement field is solved explicitly whereas damage field can be solved still by minimization. For this purposes, relatively simple expression leading to central difference scheme is used, i.e.

$$\mathcal{L}_{\mathrm{d}}(\boldsymbol{u}_i, \boldsymbol{u}_{i+1}, d_i, d_{i+1}) = \mathcal{L}(\boldsymbol{u}_i, \frac{\boldsymbol{u}_{i+1} - \boldsymbol{u}_i}{\Delta t}, d_i). \tag{3.30}$$

As a result the original minimization in continuous time domain fell apart to individual minimizations with respect to each displacement $\boldsymbol{u}_i$ and damage d_i, where $i = 0, \ldots, N$. The stationarity condition for displacement field $\boldsymbol{u}_i$ leads to discrete Euler-Lagrange equation in form

$$\frac{\partial \mathcal{L}_{\mathrm{d}}(\boldsymbol{u}_{i-1}, \boldsymbol{u}_i, d_{i-1}, d_i)}{\partial \boldsymbol{u}_i} + \frac{\partial \mathcal{L}_{\mathrm{d}}(\boldsymbol{u}_i, \boldsymbol{u}_{i+1}, d_i, d_{i+1})}{\partial \boldsymbol{u}_i} = 0, \tag{3.31}$$

which can be expressed implicitly in weak form

$$\delta\mathcal{K}(\delta\boldsymbol{u}) - \delta\Psi_{\mathrm{e}}(\delta\boldsymbol{u}) + \delta\mathcal{P}(\delta\boldsymbol{u}) = 0, \forall\delta\boldsymbol{u} \tag{3.32}$$

where

$$\delta\mathcal{K} = \frac{1}{\Delta t^2} \int_\Omega \rho(\boldsymbol{u}_{i+1} - 2\boldsymbol{u}_i + \boldsymbol{u}_{i-1}) \cdot \delta\boldsymbol{u} \,\mathrm{d}\boldsymbol{x}, \tag{3.33}$$

$$\delta\Psi_{\mathrm{e}} = \int_\Omega \left(g(d_i) \frac{\partial \psi^+(\boldsymbol{u}_i)}{\partial \boldsymbol{u}_i} + \frac{\partial \psi^-(\boldsymbol{u}_i)}{\partial \boldsymbol{u}_i} \right) \cdot \delta\boldsymbol{u} \,\mathrm{d}\boldsymbol{x}, \tag{3.34}$$

$$\delta\mathcal{P} = \int_\Omega \boldsymbol{t} \cdot \delta\boldsymbol{u} \,\mathrm{d}\boldsymbol{x}. \tag{3.35}$$

The governing weak form for damage is identical with the quasi-static version. The stationary condition

$$\delta\mathcal{A}(\boldsymbol{u}, \dot{\boldsymbol{u}}, d, \delta d) = 0, \quad \forall\delta d \tag{3.36}$$

becomes

$$\int_\Omega \frac{G_{\mathrm{f}}}{c_\alpha} \left(\frac{\alpha'(d)}{l} + l\nabla d\nabla\delta d \right) + g'(d)\psi^+ \,\mathrm{d}\boldsymbol{x} = 0, \quad \forall\delta d \tag{3.37}$$

with damage irreversibility condition

$$d_i(\boldsymbol{x}) \leq d_{i+1}(\boldsymbol{x}), \quad \forall \boldsymbol{x}, i = 0, \ldots, N-1 \tag{3.38}$$

This approach therefore induces the following explicit non-incremental dynamic procedure: (i) find displacement $\boldsymbol{u}_i$ at time t_i by solving linear problem (3.41), (ii) solve damage field d_i by variational inequality problem (3.37)-(3.38), (iii) increment time. This method is outlined in Algorithm 3.

Algorithm 3: Dynamic semi-explicit solver

Data:
Set time space, i.e. $t_0, t_N, \Delta t$;
for $t \in \{t_0, \ldots, t_N\}$ **do**
  get $\mathbf{u}_{i+1}$ from linear problem given by weak form (3.32);
  get d_{t+1} from weak form (3.37) using FEniCS-SNES solver;
  update $\boldsymbol{u}^{(i-1)} \leftarrow \boldsymbol{u}^{(i)}$;
  update $\boldsymbol{u}^{(i)} \leftarrow \boldsymbol{u}^{(i+1)}$;
  update $i \leftarrow i + 1$;
end

3.3.2.2 Implicit solver

The selected form (3.30) of discrete lagrangian $\mathcal{L}_\mathrm{d}$ is not unique and a large number of others can be used. Many of them leads to implicit solver where coupling of equations for $\boldsymbol{u}$ and d is observed. It means that monolithic or staggered approach (see Algorithm 1) must be used in each time step, which significantly increases computational time. From that reason Hofacker and Miehe [71] proposed inconsistent scheme unfortunately also named the staggered approach, where displacement $\boldsymbol{u}_i$ and damage d_i is solved only ones in each time step from decoupled equations. Lets remark this scheme with original integrator from article, i.e. Newmark constant average acceleration scheme. This scheme assumes that displacement and displacement rate in new time step t_{i+1} are expressed as

$$\dot{\boldsymbol{u}}_{i+1} = \dot{\boldsymbol{u}}_i + \frac{1}{2}\left(\ddot{\boldsymbol{u}}_{i+1} + \ddot{\boldsymbol{u}}_i\right)\Delta t_i, \tag{3.39}$$

$$\boldsymbol{u}_{i+1} = \boldsymbol{u}_i + \dot{\boldsymbol{u}}_i \Delta t_i + \frac{1}{4}\left(\ddot{\boldsymbol{u}}_{i+1} + \ddot{\boldsymbol{u}}_i\right)\Delta t_i^2. \tag{3.40}$$

By using these identities the governing weak forms become

$$\delta\mathcal{K}(\delta\boldsymbol{u}) - \delta\Psi_\mathrm{e}(\delta\boldsymbol{u}) + \delta\mathcal{P}(\delta\boldsymbol{u}) = 0, \forall\delta\boldsymbol{u} \tag{3.41}$$

where

$$\delta\mathcal{K} = \frac{4}{\Delta t^2}\int_\Omega \rho(\boldsymbol{u}_{i+1} - \tilde{\boldsymbol{u}}_i)\cdot\delta\boldsymbol{u}\,\mathrm{d}\boldsymbol{x}, \tag{3.42}$$

$$\delta\Psi_\mathrm{e} = \int_\Omega \left(g(d_i)\frac{\partial\psi^+(\boldsymbol{u}_{i+1})}{\partial\boldsymbol{u}_{i+1}} + \frac{\partial\psi^-(\boldsymbol{u}_{i+1})}{\partial\boldsymbol{u}_{i+1}}\right)\cdot\delta\boldsymbol{u}\,\mathrm{d}\boldsymbol{x}, \tag{3.43}$$

$$\delta\mathcal{P} = \int_\Omega \boldsymbol{t}\cdot\delta\boldsymbol{u}\,\mathrm{d}\boldsymbol{x}. \tag{3.44}$$

The auxiliary variable $\tilde{\boldsymbol{u}}_i$ depends only on the variables from time t_i and is defined as

$$\tilde{\boldsymbol{u}}_i = \boldsymbol{u}_i + \dot{\boldsymbol{u}}_i\Delta t_i + \frac{1}{4}\ddot{\boldsymbol{u}}_i\Delta t_i^2. \tag{3.45}$$

This procedure is summarized in Algorithm 4.

Remark 3.7. The main difference between implicit and semi-explicit scheme is in term Ψ_e. The explicit central-difference scheme assume that decomposition is made on old displacements $\boldsymbol{u}_i$, on the other hand the unknown field $\boldsymbol{u}_{i+1}$ is decomposed in implicit method. This makes the implicit scheme more difficult to implement.

Algorithm 4: Dynamic implicit staggered approach

Data:
Set time space, i.e. $t_0, t_N, \Delta t$;
for $t \in \{t_0, \ldots, t_N\}$ **do**
  get $\mathbf{u}_{i+1}$ from linear problem given by weak form (3.41);
  get d_{t+1} from weak form (3.37) using FEniCS-SNES solver;
  update $\tilde{\boldsymbol{u}}^{(i)}$ from equation (3.45);
end

3.3.2.3 Explicit solver

There is also an effort by several researchers to explore fully explicit solvers where solution not just for $\boldsymbol{u}$ but especially for d in time t_{i+1} is obtained incrementally without solving system of algebraic equations. Let's mention for example [127], but these approaches are not investigated in the thesis.

Chapter 4

Spatially reduced layered models

The damage models derived in the previous chapter are mainly used to simulate the initialization and development of cracks in laminated glass. Full 3D numerical simulation of such material can be disproportionately expensive and therefore it is often advantageous to use a spatially reduced model. For this reason, in this chapter we will derive the beam and plate models focusing on how damage is implemented.

For the problem description of multi-layer laminated glass samples, the domain Ω with the boundary $\partial\Omega$ will be divided into layers Ω_i corresponding either to glass or polymer. In the common laminated glass setup with odd number of layers M, glass is described by the odd layers, i.e. the set $\Omega_{\mathrm{G}} = \cup_{i\in\mathcal{I}}\Omega_i$ whereas polymer layers are described by the even layers, i.e. the set $\Omega_{\mathrm{P}} = \cup_{i\in\mathcal{J}}\Omega_i$ where $\mathcal{I} = \{2k : k \in \mathbb{N}_0, k < M/2\}$ and $\mathcal{J} = \{2k+1 : k \in \mathbb{N}_0, k < (M-1)/2\}$, see Figure 4.1.

We assume that the fracture occurs in the glass layers only, whereas the polymer foil remains unbroken and holds the glass shards together. The delamination on glass/polymer-interfaces is also not considered in this thesis.

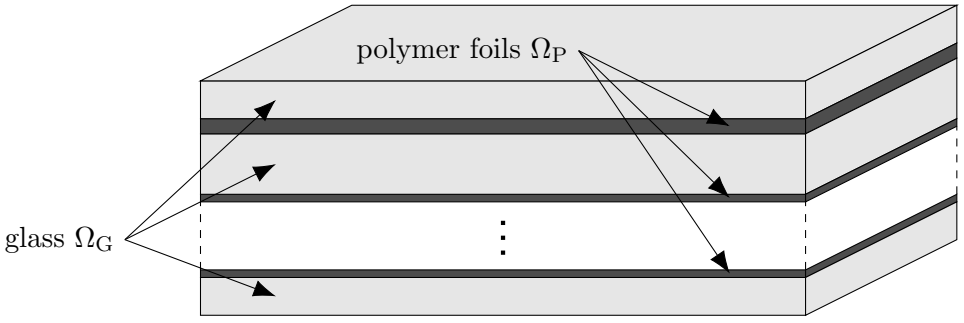

FIGURE 4.1: Subdomains of multi-layer laminated glass plates $\Omega = \Omega_{\mathrm{G}} \cup \Omega_{\mathrm{P}}$

In a quasi static regime, the governing energy functional for time instant t_n is obtained by summation over all layer indices $\mathcal{K} = \{0, \dots, M-1\}$, i.e.,

$$\mathcal{E}_n(\boldsymbol{u}, d) = \sum_{i \in \mathcal{K}} \mathcal{E}_{n,i}(\boldsymbol{u}, d) \tag{4.1}$$

where $\mathcal{E}_{n,i}$ for the polymer layer is defined as an elastic material with

$$\mathcal{E}_{n,i}(\boldsymbol{u})\Big|_{i \in \mathcal{J}} = \Psi_{\mathrm{e},i}(\boldsymbol{u}) - \mathcal{P}_{n,i}(\boldsymbol{u}), \tag{4.2}$$

which consists of the stored elastic strain energy and the external potential energy only. On the other hand, the energy functional for glass must also contain the dissipated surface energy to take into account damage:

$$\mathcal{E}_{n,i}(\boldsymbol{u}, d)\Big|_{i \in \mathcal{I}} = \bar{\Psi}_{\mathrm{e},i}(\boldsymbol{u}, d) + \Psi_{\mathrm{s},i}(d) - \mathcal{P}_{n,i}(\boldsymbol{u}). \tag{4.3}$$

Note that the elastic strain energy in glass $\bar{\Psi}_{\mathrm{e},i}(\boldsymbol{u}, d)$ differs from the elastic strain energy in polymer $\Psi_{\mathrm{e},i}(\boldsymbol{u})$ because it depends on damage. The former one is decomposed into the tensile and the compressive components whereas for interlayers, i.e. for indices $i \in \mathcal{J}$, the damage and degradation function is not considered, therefore no decomposition is needed. Note that each individual layer has its own critical energy release rate of the material $G_{\mathrm{c},i}$ and the length-scale parameter $l_{\mathrm{c},i}$.

4.1 Mindlin beam model

Although the continuum damage model is fully determined by the expressions presented above, the model must be further adjusted to spatially reduce it to the beam model. Suppose for the moment that individual layers are not binded together. As a result each layer i is described by an independent triple of kinematic variables - the longitudinal displacement u_i, rotation of the cross section φ_i and the transverse deflection w_i. Moreover the damage in layer i is denoted d_i and individual z axis starting in the layer midline is z_i, see Figure 4.2 left. Based on the common Mindlin beam approach (first-order shear theory), the longitudinal strain ε_i and shear strain γ_i of layer i are

$$\varepsilon_i(x, z_i) = u_i'(x) + z_i \varphi_i'(x), \quad \gamma_i(x) = \varphi_i(x) + w_i'(x) \tag{4.4}$$

Suppose further that each layer has width b_i and height h_i and is described by an elastic material with Young's modulus E_i and shear modulus G_i. The in-plane deflected beam

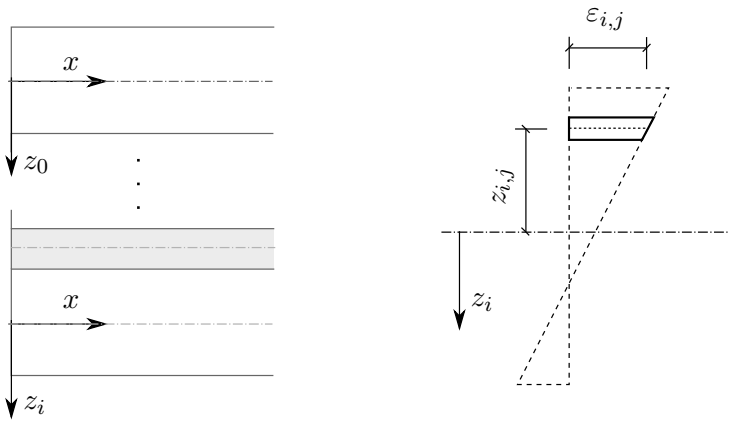

FIGURE 4.2: The local coordinate system on layer (left) and Mindlin-beam distribution of strain through layer i thickness.

energy density $\psi_{\mathrm{e},i} = (E_i\varepsilon_i^2 + G_i\gamma_i^2)/2$ for interlayers where no damage occurs. The elastic potential energy in the i-th layer therefore is

$$\Psi_{\mathrm{e},i}(u_i, w_i, \varphi_i) = \frac{1}{2}\int_0^L E_i A_i \left(u_i'(x)\right)^2 + E_i I_i \left(\varphi_i'(x)\right)^2 + G_i A_i^* \left(\varphi_i + w_i'\right)^2 \,\mathrm{d}x, \qquad (4.5)$$

whereas the elastic energy for glass must be decomposed to the tensile and the compressive part. Numerical integration over thickness is employed here and the expressions read

$$\Psi_{\mathrm{e},i}^+(u_i, w_i, \varphi_i, d_i) = \frac{1}{2}E_i b_i \int_0^L g(d_i) \sum_{j=0}^{J} \langle u_i'(x) + z_{i,j}\varphi'(x)\rangle^2 \Delta z_i \,\mathrm{d}x + \frac{1}{2}G_i A_i^* \int_0^L g(d_i) \left(\varphi_i + w_i'\right)^2 \,\mathrm{d}x, \qquad (4.6)$$

$$\Psi_{\mathrm{e},i}^-(u_i, \varphi_i) = \frac{1}{2}E_i b_i \int_0^L \sum_{j=0}^{J} \langle -u_i'(x) - z_{i,j}\varphi'(x)\rangle^2 \Delta z_i \,\mathrm{d}x, \qquad (4.7)$$

The presented identities call for some remarks. First, note that A_i and I_i are cross section area and moment of inertia of the i-th layer. The symbol A_i^* denotes the reduced area by shear reduction coefficient which, for rectangular cross section is $A_i^* = 5A_i/6$. In numerical integration over thickness, we assume that the layer i is divided into J layers with constant thickness Δz_i and with mid-plane coordinate $z_{i,j}$ of sublayer j, see right part of Figure 4.2, where linear distribution of strain across thickness is illustrated.

Finally, the damage d_i is assumed to be constant within the cross section. The regularized dissipated energy functional can therefore be integrated over the cross section as

$$\Psi_{\mathrm{s},i}(d_i, \nabla d_i) = \frac{G_{\mathrm{c},i} A_i}{c_\alpha} \int_0^L \frac{1}{l_{\mathrm{c},i}} \alpha(d) + l_{\mathrm{c},i} \|\nabla d\|^2 \,\mathrm{d}x \tag{4.8}$$

and similarly the external energy is adjusted to beam theory as

$$\mathcal{P}_{n,i}(u_i, w_i, \varphi_i) = \int_0^L b^u_{n,i} u_i + b^w_{n,i} w_i + b^\varphi_{n,i} \varphi_i \,\mathrm{d}x, \tag{4.9}$$

where (without loss of generality) we assume no surface traction. Body forces $b^u_{n,i}$, $b^w_{n,i}$ and $b^\varphi_{n,i}$ represent conjugate forces to kinematic variables u_i, w_i and φ respectively.

We still assume that the layers are not binded together, therefore the determination of the weak form is expressed in each layer independently. Moreover minimization in damage-free layers leads to common governing equations, therefore minimization in glass layers only is presented in what follows. To simplify some expressions we can arrange the unknown kinematic displacements of layer i in time n into a vector $\boldsymbol{u}_{n,i} = (u_{n,i}, w_{n,i}, \varphi_{n,i})$.

The displacements and damage from the previous step $(\boldsymbol{u}_{n-1,i}, d_{n-1,i})$ are known with the initial conditions that $\boldsymbol{u}_{0,i} = \boldsymbol{0}$ and $d_{0,i} = 0$. The unknown fields $(\boldsymbol{u}_{n,i}, d_{n,i})$ minimize the beam energy functional, i.e,

$$\delta_{\boldsymbol{u}_i} \mathcal{E}_{n,i}(\boldsymbol{u}_{n,i}, d_i) = 0, \qquad i \in \mathcal{I} \tag{4.10}$$

$$\delta_{d_i} \mathcal{E}_{n,i}(\boldsymbol{u}_i, d_{n,i}) = 0, \qquad i \in \mathcal{I}. \tag{4.11}$$

under the condition that the phase-field damage variable is not descending and stay within its limits, i.e.,

$$1 \geq d_{n,i} \geq d_{n-1,i} \geq 0, \quad i \in \mathcal{I}. \tag{4.12}$$

Here $\delta_f A$ stands for first-order variation of functional A with respect to function f.

The minimisation (4.10) leads to the following weak form of the displacement governing equation

$$\frac{\partial \Psi_{\mathrm{e},i}(\boldsymbol{u}_{n,i}, d_{n,i})}{\partial \boldsymbol{u}_{n,i}} \cdot \delta \boldsymbol{u}_{n,i} + \int_0^L \boldsymbol{b}_{n,i} \cdot \delta \boldsymbol{u}_{n,i} \,\mathrm{d}x = 0, \quad \forall \delta \boldsymbol{u}, \quad i \in \mathcal{I} \tag{4.13}$$

where $\boldsymbol{b}_{n,i} = (b^u_{n,i}, b^w_{n,i}, b^\varphi_{n,i})$ is vector of beam body forces and $\delta\boldsymbol{u}_{n,i} = (\delta u_{n,i}, \delta w_{n,i}, \delta\varphi_{n,i})$ is vector of test functions.

The final weak form for glass layers containing the numerical thickness integration reads

$$\begin{aligned} E_i b_i \int_0^L g(d_i) \sum_{j=0}^{J} \left(\langle u_i' + z_{i,j}\varphi_i\rangle - \langle -u_i' - z_{i,j}\varphi_i\rangle\right) \left(\delta u_i' + z_{i,j}\delta\varphi'\right) \Delta z_i \,\mathrm{d}x + \\ + G_i A_i^* \int_0^L g(d_i) \left(\varphi_i + w_i'\right) \left(\delta\varphi_i + \delta w_i'\right) \,\mathrm{d}x = \\ = \int_0^L b^u_{n,i}\delta u_i + b^w_{n,i}\delta w_i + b^\varphi_{n,i}\delta\varphi_i \,\mathrm{d}x, \quad \forall \delta u_i, \delta w_i, \delta\varphi_i, \quad \forall i \in \mathcal{J}. \end{aligned} \tag{4.14}$$

For the sake of overview, Let us now present also the weak form w.r.t. foil indices which leads to common Mindlin beam equations, therefore

$$\begin{aligned} \int_0^L E_i A_i u_i' \delta u_i' + E_i I_i \varphi_i' \delta\varphi_i' + G_i A_i^* \left(\varphi_i + w_i\right) \left(\delta\varphi_i + \delta w_i\right) \,\mathrm{d}x = \\ = \int_0^L b^u_{n,i}\delta u_i + b^w_{n,i}\delta w_i + b^\varphi_{n,i}\delta\varphi_i, \quad \forall \delta u_i, \delta w_i, \delta\varphi_i, \quad \forall i \in \mathcal{I}. \end{aligned} \tag{4.15}$$

Evolution equation for the phase-field damage variable in the weak form given by minimisation (4.11) is

$$\int_0^L g'(d_{n,i})\tilde{Y}_i \delta d_i \,\mathrm{d}x + \frac{2A_i}{c_\alpha} \int_0^L \alpha'(d_{n,i})\delta d_i + 2l_{\mathrm{c},i}^2 \nabla d_{n,i} \cdot \nabla \delta d_i \,\mathrm{d}x = 0, \quad \forall \delta d_i, \tag{4.16}$$

where

$$\tilde{Y}_i = \frac{2l_{\mathrm{c},i}}{G_{\mathrm{c},i}} \int_{A_i} \psi^+_{\mathrm{e},i} \,\mathrm{d}A \tag{4.17}$$

is the effective driving force. It is defined directly from the evolution equation, therefore the damage is driven by the average tensional stored energy in the cross-sectional area. To initiate the damage by extreme stress at the surface fibers, we replace the integral in driving force with

$$\int_{A_i} \psi^+_{\mathrm{e},i} \,\mathrm{d}A \equiv \frac{E_i A_i}{2} \max\left(\langle\varepsilon_i(x, h_i/2)\rangle^2, \langle\varepsilon_i(x, -h_i/2)\rangle^2\right). \tag{4.18}$$

The last missing ingredient in the model is the layer interconnection. Two interface assumptions are employed here: (i) the layers are transversely incompressible and (ii) longitudinal displacement is continuous at the interfaces. These restrictive conditions

can be written mathematically as

$$w_i = w_j, \quad \forall i \in \mathcal{K}, \forall j \in \mathcal{K}, \tag{4.19}$$

$$u_{i-1} + \varphi_{i-1}\frac{h_{i-1}}{2} = u_i - \varphi_i\frac{h_i}{2} \quad \forall i \in \mathcal{K}, i > 0, \tag{4.20}$$

These equations can be used to enforce the interconnections directly by substitution. It leads to a reduced number of kinematic unknowns. The formulation for glass, represented by weak forms (4.13) and (4.16) for indices $i \in \mathcal{I}$, remain intact, whereas kinematic variables of damage-free interlayers with indices $i \in \mathcal{J}$ are substituted by expressions determined by restrictions (4.19) and (4.20), i.e.,

$$w_i = w_0, \quad \forall i \in \mathcal{K}, \tag{4.21}$$

$$u_i = \frac{1}{4}\left(h_{i-1}\varphi_{i-1} - h_{i+1}\varphi_{i+1}\right) + \frac{1}{2}\left(u_{i-1} + u_{i+1}\right), \quad \forall i \in \mathcal{J}, \tag{4.22}$$

$$\varphi_i = \frac{1}{h_i}\left(-\frac{1}{2}\varphi_{i-1}h_{i-1} - \frac{1}{2}\varphi_{i+1}h_{i+1} + u_{i+1} - u_{i-1}\right), \quad \forall i \in \mathcal{J}. \tag{4.23}$$

The illustrative example is a 5-layer laminated glass (3 solid glasses plates and 2 interlayers) which is after substitution fully described by 7 unknowns: $w_0, u_0, \varphi_0, u_2, \varphi_2, u_4, \varphi_4$.

4.2 Mindlin plate models

The derivation of the Mindlin plate model follows the same steps as those of the Mindlin beam model. For that reason this model is presented briefly compared with the beam model. This model assumes linearly distributed strain and stress field across thickness and kinematics of i-th layer is driven by middle-surface longitudinal displacement field $\boldsymbol{u}_i$, out-of-plane scalar deflection w_i and vectorial tensor of cross-section rotations $\boldsymbol{\varphi}_i$. Based on the linearity assumption the longitudinal strain $\boldsymbol{\varepsilon}_i$ and shear strain $\boldsymbol{\gamma}_i$ can be established as

$$\boldsymbol{\varepsilon}_i(\boldsymbol{x}, z_i) = \nabla_{\mathrm{s}}\boldsymbol{u}_i(\boldsymbol{x}) + z_i\nabla_{\mathrm{s}}\mathrm{S}\boldsymbol{\varphi}(\boldsymbol{x}) \tag{4.24}$$

$$\boldsymbol{\gamma}_i(\boldsymbol{x}) = \mathrm{S}\boldsymbol{\varphi}_i(\boldsymbol{x}) + \nabla w_i(\boldsymbol{x}), \tag{4.25}$$

where z_i is out-of-plane coordinate meanwhile $\boldsymbol{x} = \{x, y\}$ is in-plane coordinate system of middle-surface Ω_i. The S is auxiliary matrix

$$\mathrm{S} = \begin{bmatrix} 0 & 1 \\ -1 & 0 \end{bmatrix}. \tag{4.26}$$

The Mindlin-Reissner plate model ignores the normal stress across thickness, therefore in each infinitesimal layer plane-stress conditions can be assumed. Therefore the stress

field is defined as

$$\boldsymbol{\sigma}_i(\boldsymbol{\varepsilon}_i) = \mathrm{D}_i^{\mathrm{PS}} : \boldsymbol{\varepsilon}_i, \tag{4.27}$$

$$\boldsymbol{\tau}_i(\boldsymbol{\gamma}_i) = 2\nu_i \mathrm{I} : \boldsymbol{\gamma}_i, \tag{4.28}$$

where D^{PS} is plane-stress elastic tensor defined again through Lame's coefficients λ_i and ν_i and I is the identity tensor. The last ingredient is thickness integration for spatial reduction. It is impossible to perform it in closed form, therefore a numerical integration is employed and active/passive elastic energy becomes

$$\Psi_{\mathrm{e},i}^{+} = \frac{1}{2}\int_{\Omega_i} g(d_i)\left(\sum_{j=0}^{J} \Delta z_{i,j}\boldsymbol{\varepsilon}_{i,j} : \boldsymbol{\sigma}_{i,j}^{+} + \xi h_i \boldsymbol{\gamma}_i \cdot \boldsymbol{\tau}_i\right) \mathrm{d}\boldsymbol{x}, \tag{4.29}$$

$$\Psi_{\mathrm{e},i}^{-} = \frac{1}{2}\int_{\Omega_i} \sum_{j=0}^{J} \Delta z_{i,j}\boldsymbol{\varepsilon}_{i,j} : \boldsymbol{\sigma}_{i,j}^{-} + (1-\xi) h_i \boldsymbol{\gamma}_i \cdot \boldsymbol{\tau}_i \,\mathrm{d}\boldsymbol{x}. \tag{4.30}$$

Summation again represents dividing i-th layer into sublayers indexed by j, each represented by in-plane stress $\boldsymbol{\sigma}_{i,j}$ and strain $\boldsymbol{\varepsilon}_{i,j}$ with sub-thickness $\Delta z_{i,j}$. Parameter ξ determines what amount of shear is degraded; $\xi = 1$ means shear is fully degraded meanwhile $\xi = 0$ is shear damage-free state. Still the stress tensor $\sigma_{i,j}^{\pm}$ must be somehow decomposed. Based on this decomposition this model is denoted as $\mathrm{P}-\mathrm{SD}$ if spectral decomposition is used and is denoted $\mathrm{P}-\mathrm{VD}$ for volumetric-deviatoric split. The degradation function still remains $g(d_i) = (1-d_i)^2$.

Finally recall the plate substitution expressions for interlayers to remind usage of the auxiliary matrix

$$w_i = w_1, \quad \forall i \in \mathcal{K}, \tag{4.31}$$

$$\boldsymbol{u}_i = \frac{1}{4}\left(h_{i-1}\mathbf{S}\,\boldsymbol{\varphi}_{i-1} - h_{i+1}\mathbf{S}\,\boldsymbol{\varphi}_{i+1}\right) + \frac{1}{2}\left(\boldsymbol{u}_{i-1} + \boldsymbol{u}_{i+1}\right), \forall\, i \in \mathcal{J}, \tag{4.32}$$

$$\mathbf{S}\,\boldsymbol{\varphi}_i = \frac{1}{h_i}\left(-\frac{1}{2}\mathbf{S}\,\boldsymbol{\varphi}_{i-1}h_{i-1} - \frac{1}{2}\mathbf{S}\,\boldsymbol{\varphi}_{i+1}h_{i+1} + \boldsymbol{u}_{i+1} - \boldsymbol{u}_{i-1}\right), \forall\, i \in \mathcal{J}. \tag{4.33}$$

4.3 Parameters for reduced models

Although derived for pure tension, the relationships introduced in Table 3.2 could also be used for thin structures in bending providing the stress distribution is close to constant within the finite elements in which the glass fracture could occur. Therefore, this approximation was used in the 2D plane-stress simulations of the longitudinal cross-section where the mesh was refined in the area of maximum bending moments.

On the contrary, the relations introduced in Eqs. (3.21) and (3.22) are not applicable if we employ the beam and plates formulations with one element per the layer thickness characterized by a through-the-thickness constant damage parameter. To illustrate this

fact, we establish relations between the length-scale parameter l_c and the fracture energy G_f for beams under pure bending.

Similarly to previous approaches, e.g. [22, 121, 163], we start from the evolution equation for the damage distribution Eq. (3.18) with $\dot{d} > 0$ and neglect all spatial derivatives of d as we consider a spatially homogeneous solution. By performing integration over the thickness h, we get

$$\frac{G_\mathrm{f} h}{c_\alpha l_\mathrm{c}} \frac{\mathrm{d}\alpha(d)}{\mathrm{d}d} = 2(1-d) \int_{-h/2}^{h/2} \psi_\mathrm{e}^+ \,\mathrm{d}z. \tag{4.34}$$

where we limit our attention to PF-P model for simplicity. To that end, we assume that the damage starts to evolve if the largest tensile stress reaches the tensile strength f_t. This allows us to write the integral on the right-hand side of Eq. (4.34) in terms of f_t as

$$\int_{-h/2}^{h/2} \psi_\mathrm{e}^+ \,\mathrm{d}z = \frac{f_\mathrm{t}^2 h}{12E}. \tag{4.35}$$

If we set $d = 0$ at the onset of cracking, Eqs. (4.34) and (4.35) lead for $c_\alpha = 8/3$ and $\dfrac{\mathrm{d}\alpha(d)}{\mathrm{d}d} = 1$ to the approximation of the length-scale parameter in the form

$$l_\mathrm{c} = 6 \left(\frac{3}{8} \frac{G_\mathrm{f} E}{f_\mathrm{t}^2} \right). \tag{4.36}$$

The same result can be derived under some simplifying assumptions for the PF-B formulation,

$$l_\mathrm{c} = 6 \left(\frac{27}{256} \frac{G_\mathrm{f} E}{f_\mathrm{t}^2} \right). \tag{4.37}$$

Therefore the relationships (3.21)-(3.22) are not valid for a beam or plate under pure bending. To control this model by maximum tensile strength f_t the identities (4.36)-(4.37) must be used. Nevertheless this applies only for pure bending, but the reality is more complicated in general case, therefore another approach can be employed

In this regard it appears useful to replace the strain energy density ψ_e^+ by a constant ψ_sur^+ representing the strain energy density calculated on the basis of the maximum tensile stress. This rewrites Eq. (4.16) as

$$\int_{\Omega_\mathrm{s}} \left(\frac{h G_\mathrm{f}}{c_\alpha} \left(\frac{\alpha'(d)}{l} + 2l \nabla d \nabla \delta d \right) + g'(d) \psi_\mathrm{sur}^+ \cdot h \right) \mathrm{d}\boldsymbol{x} = 0, \quad \forall\, \delta d. \tag{4.38}$$

The indices have been omitted here because this conclusion is valid also for quasi-static as well for dynamic regime likewise for layered or single-layer case.

Chapter 5

Quasi-static brittle fracture of laminated glass

This chapter is based on article [132].

5.1 Numerical case study of a monolithic glass plate under bending

This first part of our study is devoted to the monolithic glass plates only. This way, we want to separate the effect of polymer foils and focus purely on the glass response. In the next two sections the response of laminated glass is discussed, and the numerical model is validated against the experimental data. Implementation details are presented in section 3.2.4.

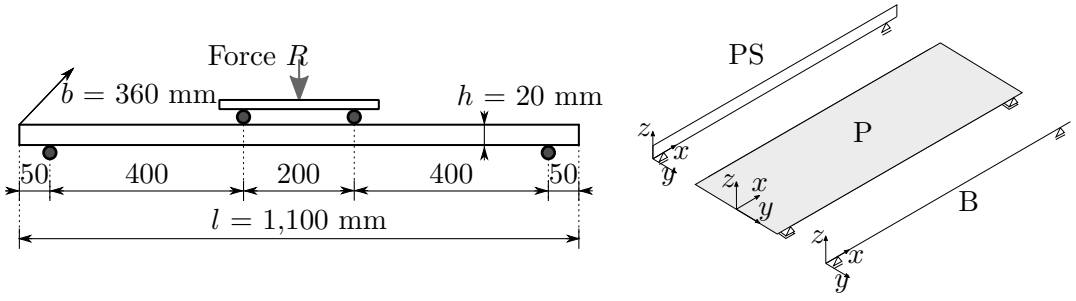

FIGURE 5.1: Four-point bending loading scheme and geometry of a glass sample and three different spatially reduced models, i.e., 2D plane-stress (PS) longitudinal cross-section, Reissner-Mindlin plate (P), Timoshenko beam (B).

The numerical experiments were performed on a single glass sheet of dimensions 1,100 mm × 360 mm × 20 mm loaded in four-point bending, see Figure 5.1. The prescribed displacement of loading head was gradually increased until fracture with the loading-rate of

0.03 mm/s. The pseudo-time increment in Algorithms 1 and 2 started initially at 0.1 s and was subsequently refined to 0.01 s and finally to 0.001 s close to localisation. Regarding the discretization, we tested three different spatially reduced models schematically shown in Figure 5.1, i.e., 2D plane-stress model (PS) of the longitudinal cross-section, 2D model using the Mindlin-Reissner plate theory (P), and 1D model based on the Mindlin beam theory (B). For the simulations, a few types of meshes were tested, i.e., PS-Uniform: regular uniform mesh with the element size of 2 mm, PS-Refined mesh, P-Refined mesh or B-Refined mesh refined in the largest-bending-moment area, Figure 5.2. Let us highlight that all simulations reported in the following assume the symmetries shown in Figure 5.2. Hence, the simulation results and the localised crack in particular must be interpreted by taking these symmetries into consideration.

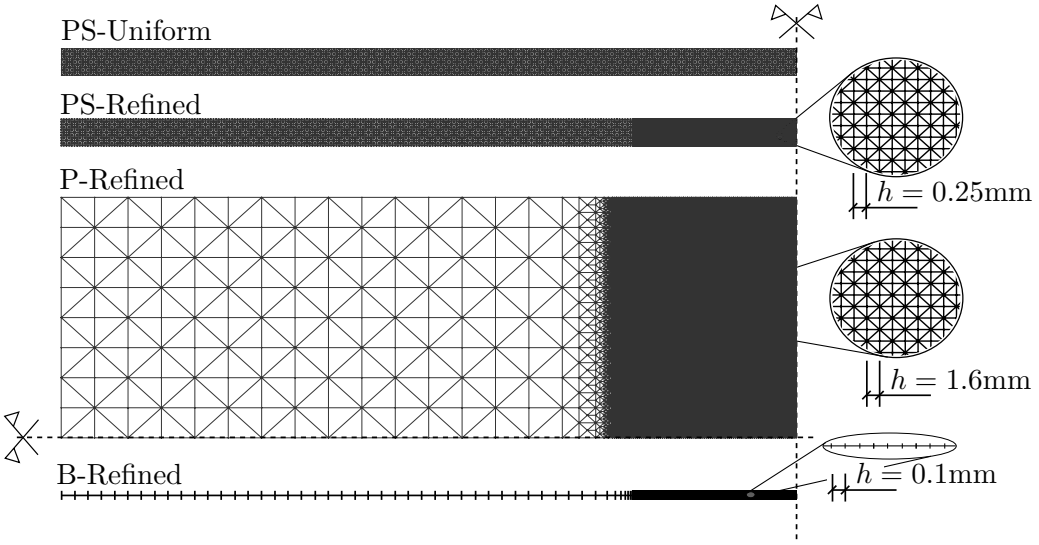

FIGURE 5.2: Regular uniform or refined discretization for the 2D plane-stress model (PS) and refined meshes used for a quarter of a plate (P) and a half of a beam (B).

Finite elements with linear basis functions were employed in this numerical study as the phase-field formulations require relatively fine meshes in any case. Prior to modelling damage, we tested the convergence of the solution to the linear elastic problem without glass fracture. For example for the plane-stress formulation, the errors in displacements and stresses were under 2.5% for the uniform mesh and under 1.5% for the refined variant, compared to the reference solution corresponding to the mesh of 1,100×20 quadratic elements.

The length-scale parameter l_c was set according to the element size, i.e., $l_\mathrm{c} \approx 2h_\mathrm{min}$ with the smallest element size h_min, see [102]. Subsequently, the corresponding fracture energy G_f was derived according to Eqs. (3.21) and (3.22), or according to the modified version for beams in Eqs. (4.36) or (4.37).

5.1.1 Effect of the phase-field formulation and mesh refinement

First, we present a comparison of three responses corresponding to the individual phase-field formulations using the PS model. In Figures 5.3 and 5.4, the diagrams show the evolution of the largest tensile stress σ_x at the midpoint and the overall reaction R under the loading points for the prescribed vertical displacement of the loading head $\bar{w}$. It can be seen in Figure 5.3 that the tensile stress evolution differ quite significantly for the regular mesh. The PF-B model yields a nonlinear stress-strain response from the beginning of the loading test, so no initial linear phase is visible in the plots in Figure 5.3. Moreover, the failure stress differs for the three formulations. We attribute this discrepancy to a relatively coarse mesh and linear basis functions for the displacement field yielding constant stresses and strain energy density within an element. Consequently, the fracture occurs at different prescribed loading levels.

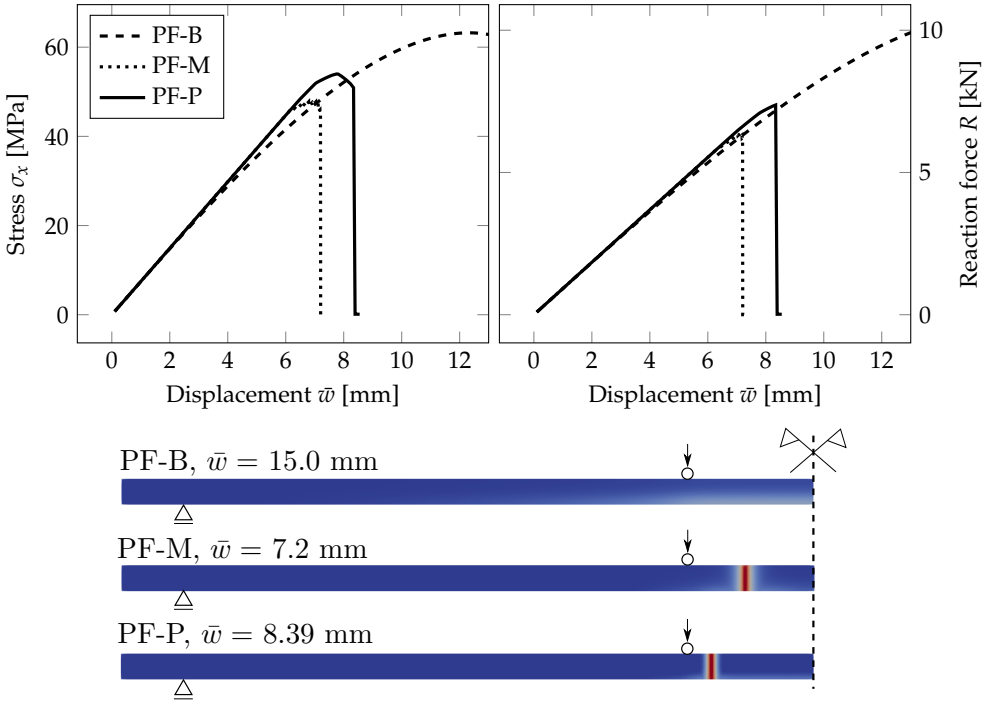

FIGURE 5.3: PS-Uniform mesh, anisotropic staggered solver with the spectral-decomposition split: Comparison of phase-field formulations in terms of the evolution of the largest tensile stress at the midpoint and the overall reaction under the loading points for the prescribed displacement, complemented with the damage evolution plot showing the position of the localised cracks.

Therefore, we refined the mesh in the area of the largest bending moment, where the cracks are supposed to initiate. The element size in this area is about 0.25 mm, see Figure 5.2. The evolution of the normal stress and reaction and the damage after the crack localisation are shown in Figure 5.4. In this case, the failure stresses are closer to each other and to the adopted tensile strength of glass. We assume that for even finer mesh, the performance of the PF-M and PF-P models would be almost indistinguishable. On

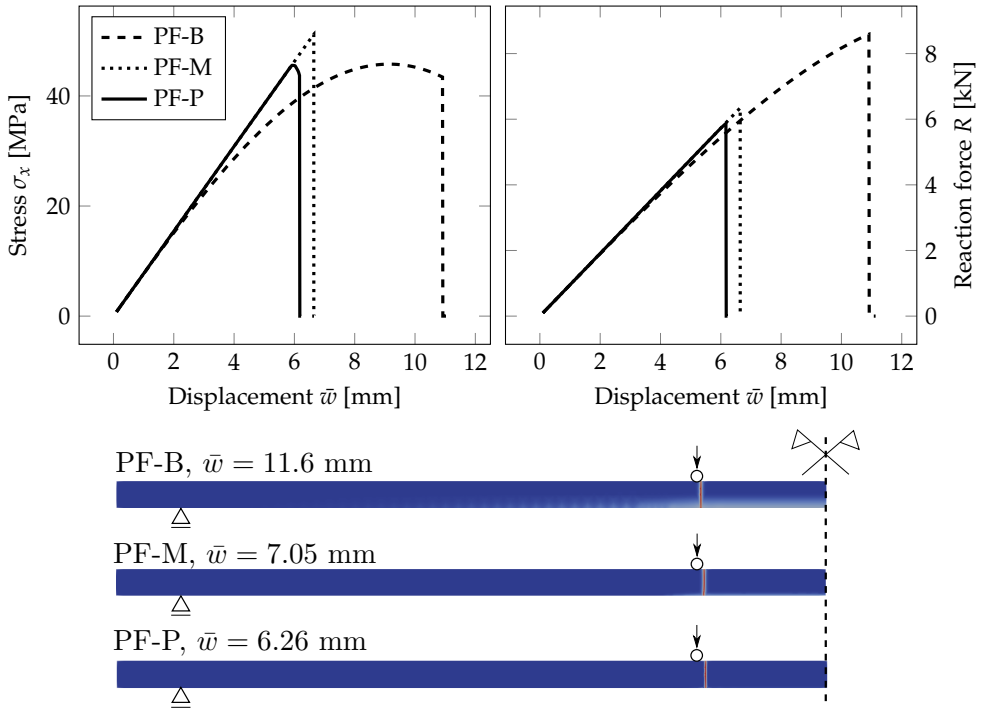

FIGURE 5.4: PS-Refined mesh, anisotropic staggered solver with the spectral-decomposition split: Comparison of phase-field formulations in terms of the evolution of the largest tensile stress at the midpoint and the overall reaction under the loading points for the prescribed displacement, complemented with the damage evolution plot showing the position of the localised cracks.

the other hand, a significant nonlinear response prior to fracture can be seen for the PF-B formulation. Also the crack localised in this particular case for an almost two-times higher prescribed displacement.

Further, Figure 5.5 shows the phase-field parameter evolution before the damage is localised in one crack for the PF-P formulation. We use one scale for all the plots. Initially, the damage starts to evolve in the area of the largest bending moment. Then, a few relatively equidistant short ridges appear, and finally, one crack, corresponding to the maximum of the phase-field variable, localises close to the loading point. Hence, the phase-field model seems to predict the initiation of multiple regularly spaced cracks, from whose only one localises, as the localised solution corresponds to a lower energy value, e.g., [14, 29, 72].

Based on this comparison, we decided to prefer the PF-P formulation for the next analyses as it provides the initial linear elastic response of glass and preserves the variational structure of the problem. The refined mesh discretisations were used for all following examples in this numerical study and all three spatially reduced models; the label "Refined" is omitted to shorten the notation.

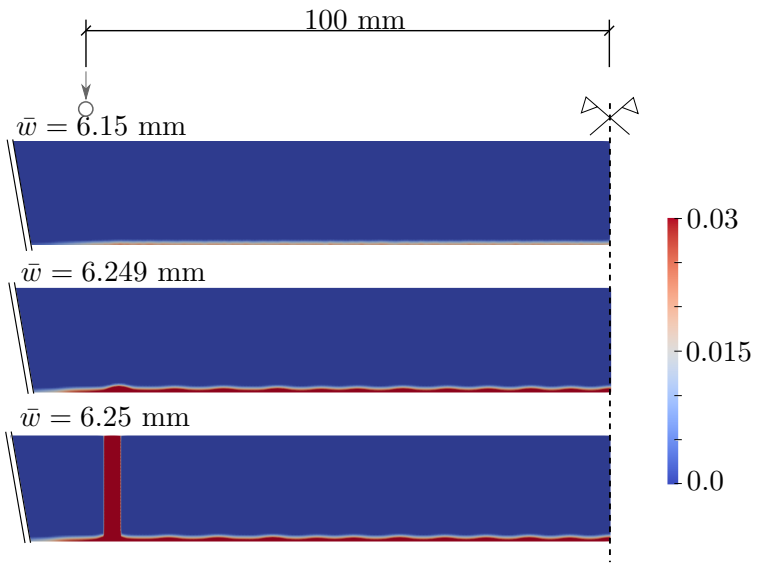

FIGURE 5.5: PS-Refined mesh, anisotropic staggered solver with the spectral-decomposition split: Evolution of the phase-field parameter using PF-P formulation.

5.1.2 Effect of the type of the solver and tension/compression energy split

Subsequently, we briefly compare the anisotropic and hybrid formulation (Section 3.2.4) within the staggered scheme for our example, combined with two different ways for the tension-compression split of the strain tensor from Section 3.2, i.e., the volumetric-deviatoric split and the spectral decomposition. As can be seen from Figure 5.6, both

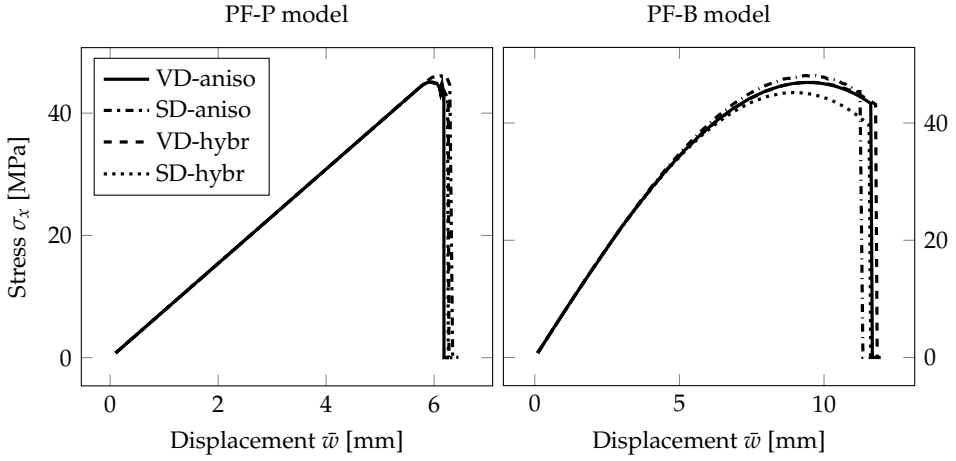

FIGURE 5.6: PS-Refined mesh: Comparison of the anisotropic solver, Algorithm 1, employing the volumetric-deviatoric split (VD-aniso) or spectral decomposition approach (SD-aniso) with their counterparts using a linear hybrid formulation (VD-hybr and SD-hybr), Algorithm 2.

ways of the formulation and decomposition deliver almost identical response for the PF-P model of a thin glass plate under bending. For completeness, we show the same comparison also for the PF-B formulation. The observed differences can be attributed

to the predicted early-stage degradation. However, the effect of the choice of the fully anisotropic or hybrid formulation and the split is negligible for our purposes.

5.1.3 Effect of the dimensional reduction

Before comparing the fracture response corresponding to different dimensional reductions, we illustrate the effect of the relationship between the fracture energy G_f set according to Eqs. (3.22) and (4.36) for the selected l_c and f_t.

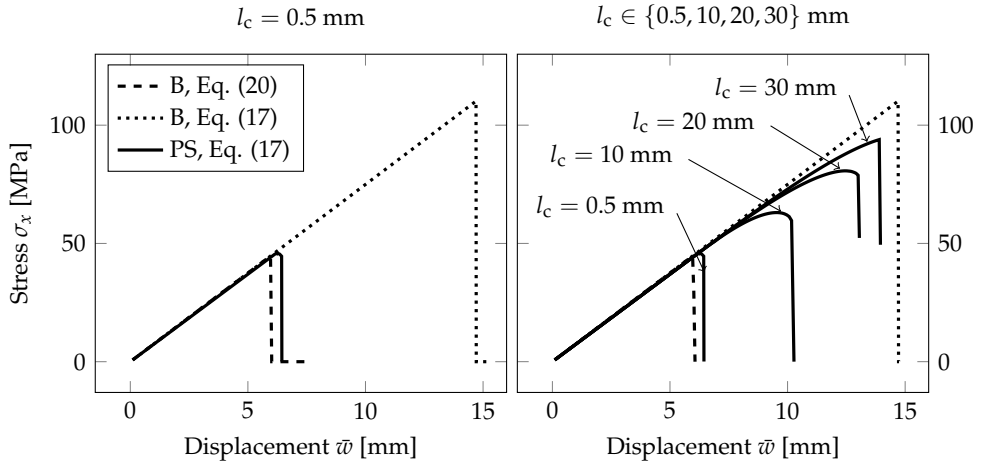

FIGURE 5.7: PF-P model, anisotropic staggered approach with the spectral-decomposition split: Comparison of the plane-stress model (PS) with the formulation derived for beams (B) using two constitutive relationships for G_c, l_c, and f_t, i.e., $G_\mathrm{f}/l_\mathrm{c} = 8f_\mathrm{t}^2/(3E)$ from equation (3.22) and $6G_\mathrm{f}/l_\mathrm{c} = 8f_\mathrm{t}^2/(3E)$ from equation (4.36).

Figure 5.7 shows the evolution of the largest tensile stress at the midpoint of the span for the increasing prescribed deflection. The PF-P formulation with the spectral decomposition was used within the staggered solver. The derived fracture energy G_f corresponds to the critical stress $f_\mathrm{t} = 45$ MPa, and the length-scale parameter for the PS model set to $l_\mathrm{c} = 0.025h = 0.5$ mm, i.e., twice the element size, or $l_\mathrm{c} \in \{10, 20, 30\}$ mm, i.e., $l_\mathrm{c} \in \{0.5h, h, 1.5h\}$. For the B model, the length-scale parameter was fixed to the value $l_\mathrm{c} = 0.2$ mm, i.e., twice the element size, as its change does not affect the results in contrast with the PS model.

For the beam formulation with the mesh density shown in Figure 5.2, the largest failure stress at the bottom surface under tension is more than doubled compared to the given critical stress f_t with l_c provided by equation (3.22). The adjusted fracture energy according to equation (4.36) provides the response comparable to the plane-stress formulation, and the fracture occurs close to the prescribed tensile strength if the length-scale parameter is much smaller than the thickness of the glass layer, e.g., $l_\mathrm{c} = 0.025h = 0.5$ mm, see Figure 5.7. On the other hand, if the crack is more diffused, the failure stress on the bottom surface increases. Then, a nonlinear response can also be seen in the stress-displacement diagram for the PS model. If the length-scale parameter is greater than

the glass thickness, the response of the PS model is approaching the upper bound given by the beam theory using the fracture energy derived from Eq. (3.22).

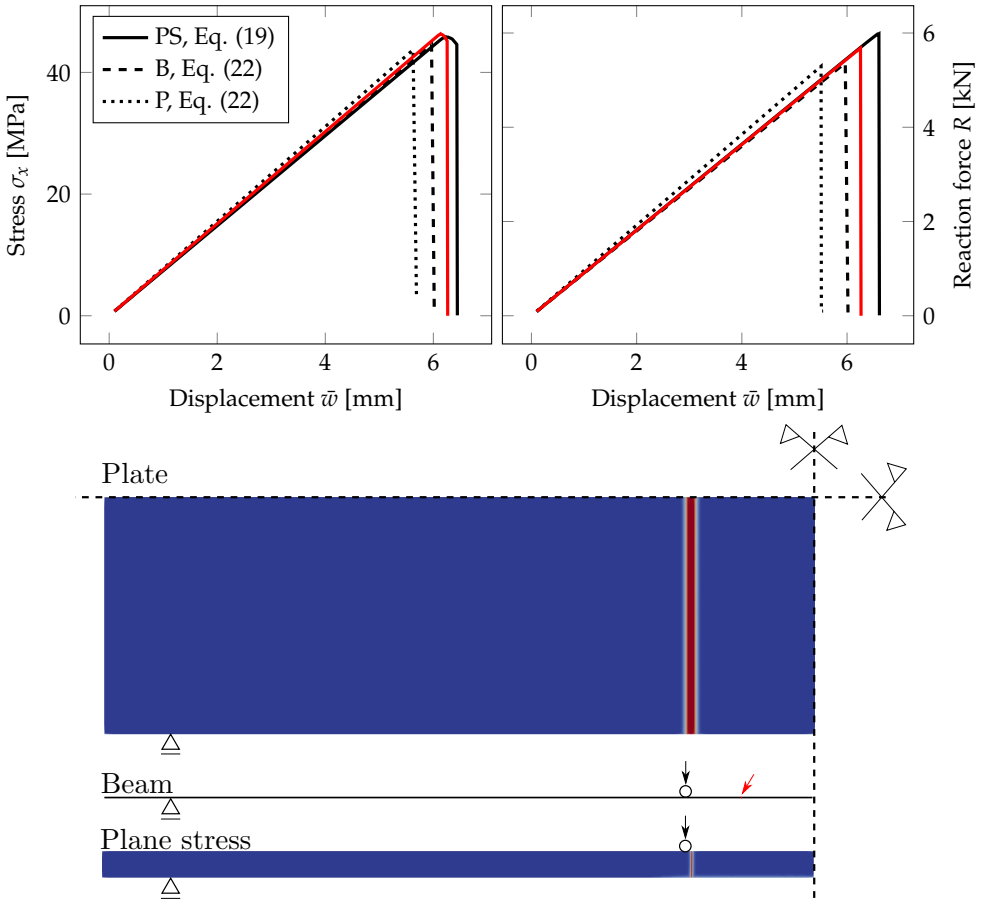

FIGURE 5.8: PF-P formulation, anisotropic staggered approach with the spectral-decomposition split: Comparison of plane stress (PS) for the PS-Refined mesh from Figure 5.2 (black line) or additionally refined in the area of the expected crack propagation (red line), beam (B), and plate (P) model in terms of the evolution of the largest tensile stress at the midpoint, the overall reaction, and the damage evolution showing the position of the localised cracks.

This comparison illustrates that the fracture energy has to be set with respect to the applied dimensional reduction, loading type, and the value of the length-scale parameter compared with the thickness of the structure under bending. For example in [84], the authors report the same response of their phase-field fracture model for plates and the reference solution for a solid using a constant G_f value and the length-scale parameter l_c equal to the plate thickness. However, this identity cannot be achieved for any values of the length-scale parameter.

Figure 5.8 compares the response of the PS, B, and P models for a monolithic glass simply supported on two sides. The evolution of the largest tensile stress and the overall reaction force R under the loading points is plotted for the three models as a function of the prescribed deflection. The failure stress is almost the same for the beam and plate formulations and slightly higher for the PS model. The stiffnesses of the monolithic

glass plate corresponding to the beam theory and the PS model are equivalent, but the fracture occurs later for the PS model. The red line corresponds to a mesh additionally refined in the area of the expected crack propagation to illustrate how the responses for the B a PS models converge if the PS mesh is refined.

On the other hand, the plate formulation is stiffer and the glass fractured for a lower prescribed deflection. We attribute these small differences again to a rather coarse mesh for the plate in some unfractured regions and to linear basis functions used in this analysis. We expect the differences to decrease at the cost of higher computational demands. The crack appeared at the same position near the loading for the PS and P model, see Figure 5.8. For the B model, the position of fracture is different, but still at the region of the constant largest bending moment.

For the plate model, the evolution of the phase-field parameter is displayed in Figure 5.9. Each rectangle represents a quarter of the glass plate for a different magnitude of the prescribed loading. The damage starts to initiate at about a quarter of the plate width near the loading point and subsequently localises into a straight crack.

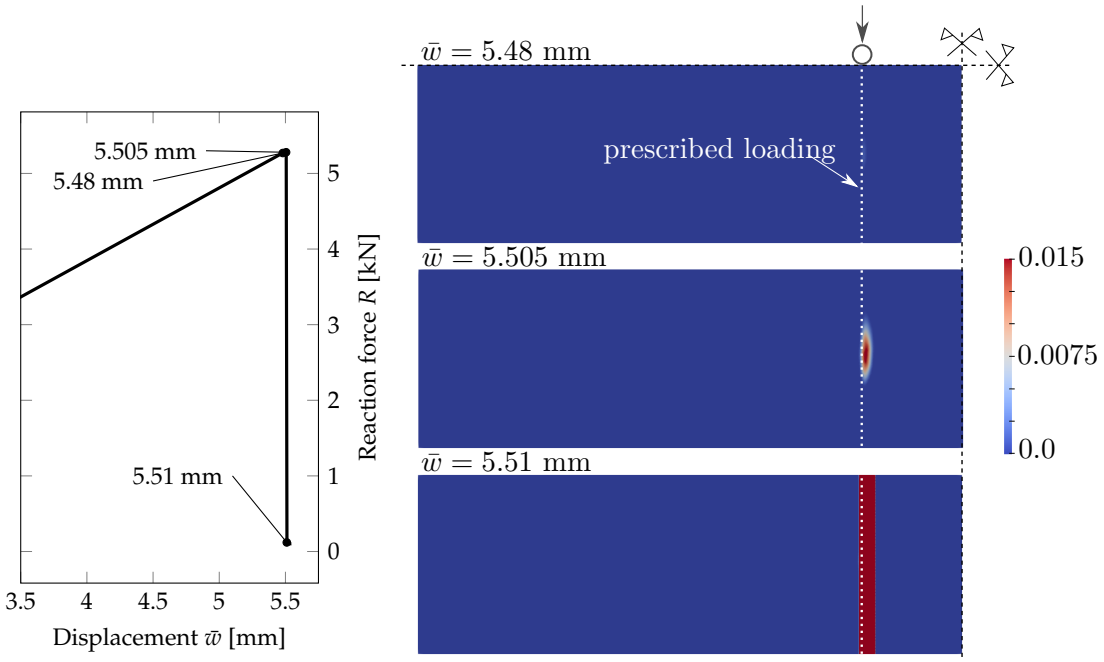

FIGURE 5.9: PF-P formulation, anisotropic staggered approach with the spectral-decomposition split: Evolution of the phase-field parameter on a quarter of the glass plate.

5.1.4 Reduced glass strength near plate edges

The tensile strength of thin glass plates is highly affected by micro-defects and scratches induced during the production, transport, and handling. Moreover, the edge strength depends on the quality of edge finishing. Because the region of the largest tensile stresses includes parts of both edges for the four-point bending tests, the crack mostly initiates

from a defect on the edge. As suggested for example in the German glass standard [2], the strength on edges can be reduced to initiate the cracking from the edge. Near the bottom edge about 50 mm from the midspan, we modified the strength to 80% of the given tensile strength in a $1.5l_c \times 1.5l_c$ square, i.e., 4.8 mm × 4.8 mm in our example. Then, the crack starts to initiate from this predefined area toward the opposite edge, as can be seen in Figure 5.10. For a smaller area, e.g. $l_c \times l_c$, the localisation does not occur from an edge point. If we use a quarter of the plate with two axes of symmetry, the final crack is almost perpendicular to the long edges as the strength was reduced on two opposite sides. On the other hand, the crack is inclined when one half of the laminated glass plate is used in simulation, Figure 5.10.

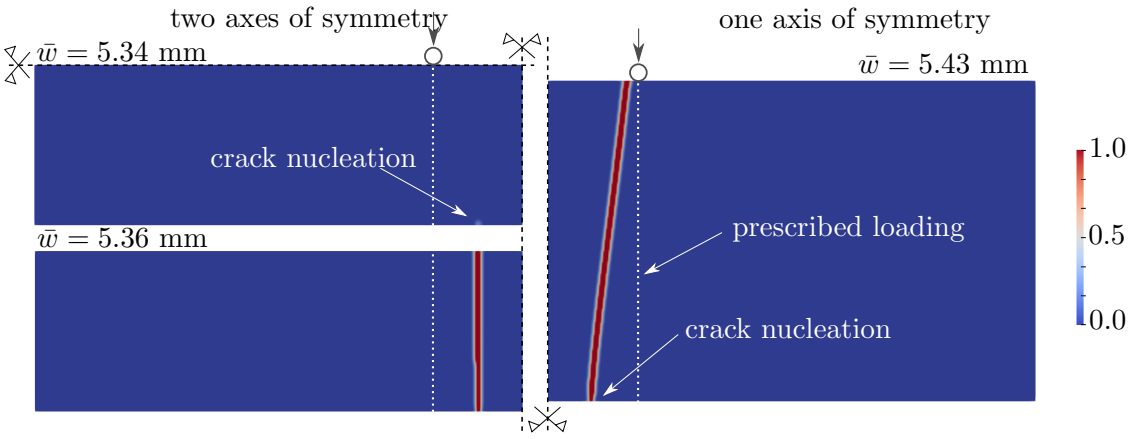

FIGURE 5.10: PF-P formulation, P mesh, anisotropic staggered approach with the spectral-decomposition split: Evolution of the phase-field parameter on a quarter of the glass plate and the final crack pattern on a half of the plate.

Similarly, the strength can be reduced along the whole edge. The lower strength has to be assigned not only to the nodes directly on the edge but for a band of nodes to overcome the cracking initiated on the inner surface. However, we are unable to reproduce the typical V-shape fracture patterns, shown in Figure 5.16 on page 53, with the quasi-static plate model considering homogeneous material data in the plate interior; only one crack resulted from all numerical simulations.

5.2 Experimental testing on laminated glass

The material parameters needed for the numerical model were obtained from both the literature review and experimental testing on three-layer laminated glass samples presented in this section.

5.2.1 Material composition of laminated glass

Two types of laminated glass samples were tested under quasi-static loading. All of them were three-layer plates with a polymer interlayer and two glass layers of the same

type. The material specification is summarised in Table 5.1. The nominal dimensions of samples were as follows: the length $l = 1.1$ m, the width $b = 0.36$ m, and the thicknesses of layers $h_1/h_2/h_3 = 10/0.76/10$ mm.

name	glass	interlayer	samples
ANG-EVA	annealed	ethylen-vinyl acetate	5
ANG-PVB	annealed	polyvinyl butyral	5

TABLE 5.1: Material composition of layers in tested specimens.

5.2.2 Testing of polymers and the material model

In the present study, we exploit the results of our extensive experimental program reported in [64]. Therein, small three-layer cylindrical samples were loaded in dynamic torsion or dynamic single-lap shear under different ambient temperatures and applied frequencies. Subsequently, a set of parameters of the generalised Maxwell model for each interlayer were identified. For both polymer foils, the series employed in the numerical modelling are summarised in Table 5.2.

	EVA	PVB		EVA	PVB
τ_p [s]	G_p [kPa]	G_p [kPa]	τ_p [s]	G_p [kPa]	G_p [kPa]
10^{-9}	6,933.9	–	10^{2}	445.1	587.2
10^{-8}	3,898.6	–	10^{3}	300.1	258.0
10^{-7}	2,289.2	–	10^{4}	401.6	63.8
10^{-6}	1,672.7	–	10^{5}	348.1	168.4
10^{-5}	761.6	1,782,124.2	10^{6}	111.6	–
10^{-4}	2,401.0	519,208.7	10^{7}	127.2	–
10^{-3}	65.2	546,176.8	10^{8}	137.8	–
10^{-2}	248.0	216,893.2	10^{9}	50.5	–
10^{-1}	575.6	13,618.3	10^{10}	322.9	–
10^{0}	56.3	4,988.3	10^{11}	100.0	–
10^{1}	188.6	1,663.8	10^{12}	199.9	–

TABLE 5.2: Prony series for the generalised Maxwell model with the relaxation times τ_p and corresponding shear moduli G_p for the reference temperature $T_0 = 20\,^{\circ}\mathrm{C}$ and the long-term moduli $G_\infty = 682.18$ kPa for EVALAM 80-120 (EVA) and $G_\infty = 232.26$ kPa for TROSIFOL BG R20 (PVB), [64]

To simplify the formulation, we assume that the time/temperature-dependent response of the interlayer can be approximated by an equivalent elastic material with the shear modulus G in the middle of each time interval t for the temperature T, see e.g. [39]. Then, the shear modulus of the interlayer is evaluated in each time instant according to

$$G(t,T) \approx G_\infty + \sum_{p=1}^{P} G_p \exp^{\frac{-t/2}{a_T(T)\tau_p}}, \tag{5.1}$$

with the Prony series $(G_p, \tau_p)_{p=1..P}$ and the long-term shear modulus G_∞ from Table 5.2. For the shift parameter a_T reflecting the temperature-dependency of the polymer interlayers, we employed the Williams-Landel-Ferry equation [149]

$$\log a_T(T) = \frac{-C_1(T - T_0)}{C_2 + T - T_0}. \tag{5.2}$$

The model parameters C_1 and C_2 associated with the reference temperature T_0 are listed in Table 5.3.

		EVA	PVB	
Reference temperature	T_0	20	20	°C
Parameters	C_1	339.102	8.635	–
	C_2	1,185.816	42.422	°C
Shift parameter	$\alpha_T(T = 25°\text{C})$	0.03769	0.1229	–

TABLE 5.3: Parameters for the time-temperature superposition using the William-Landel-Ferry equation [149]

5.2.3 Quasi-static bending tests

The set of *four-point bending tests* was performed on five ANG-EVA and five ANG-PVB samples at the Faculty of Civil Engineering, Czech Technical University in Prague. The experiments were displacement-controlled with the cross-head speed of the MTS loading device of 0.03 mm/s. The samples were placed on cylindrical supports and separated with rubber pads, Figure 5.11. The measured room temperature was 25 °C. Two displacement sensors measured the vertical deflection at the midspan of samples to check that the experimental set-up was symmetric. Additionally, eight strain gauges LY 11-10/120 were attached to the glass surface: five on the upper surface under compression and three on the bottom surface under tension, Figure 5.11 or [62].

Table 5.4 summarizes the extreme tensile failure stresses for the two types of laminated glass samples independently. These values are utilized for the validation of the numerical solver in the next section. Mostly, the fracture originated from a defect on the plate's edge.

samples	min failure stress [MPa]	max failure stress [MPa]
ANG-EVA	32	60
ANG-PVB	28	69

TABLE 5.4: Extreme tensile failure stresses on the bottom surface of laminated glass obtained experimentally for the four-point bending.

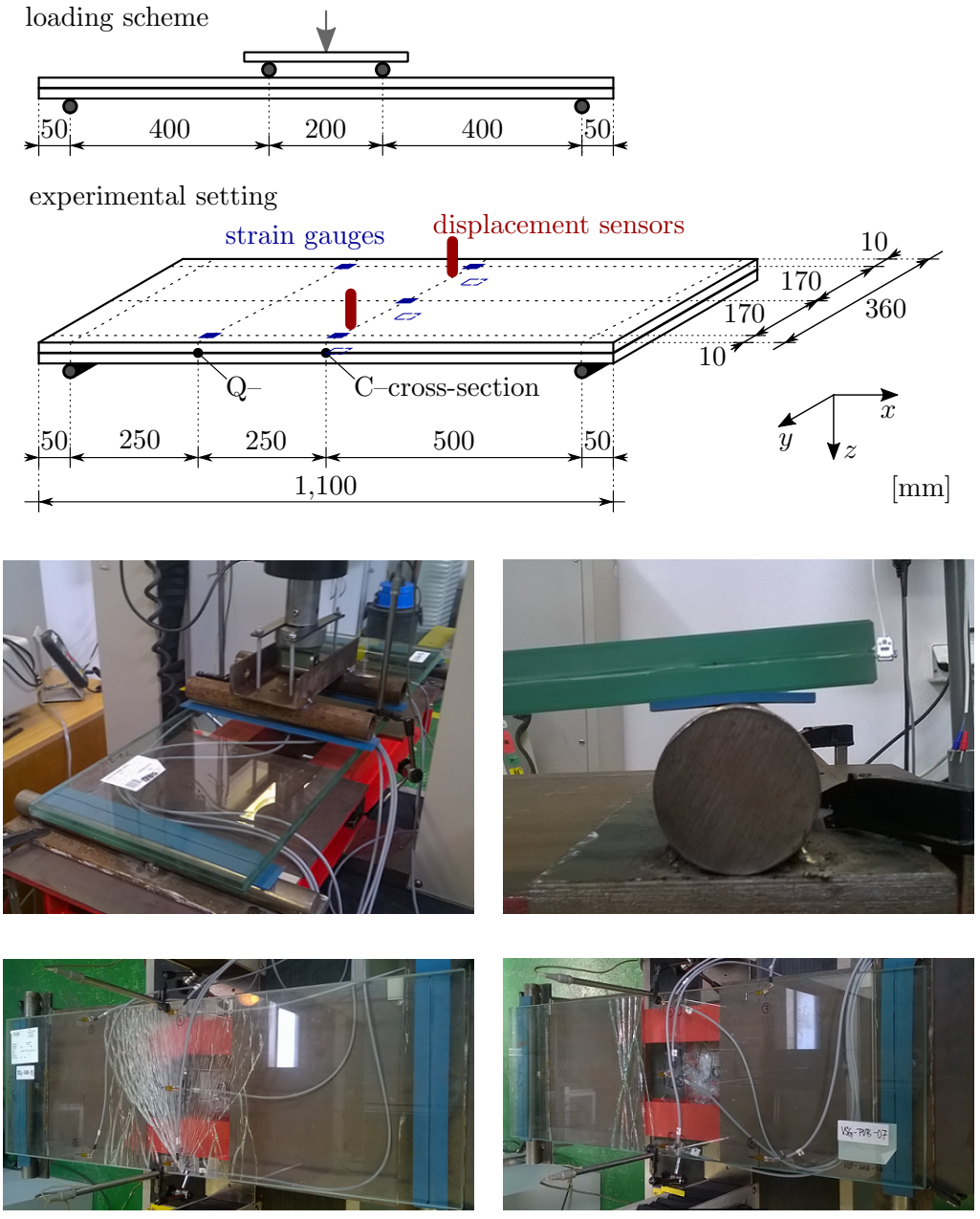

FIGURE 5.11: Experimental setup and crack patterns; courtesy of Tomáš Hána from CTU in Prague.

5.3 Validation of phase-field model against experimental data

In order to assess the behaviour of the phase-field model and the quality of the identified material parameters for both foils, we present a validation of the numerical predictions against the experimentally measured response for the three-layer laminated glass plates.

Even though the beam formulation is computationally most effective, we selected for the simulation the 2D plane-stress model representing the longitudinal cross-section,

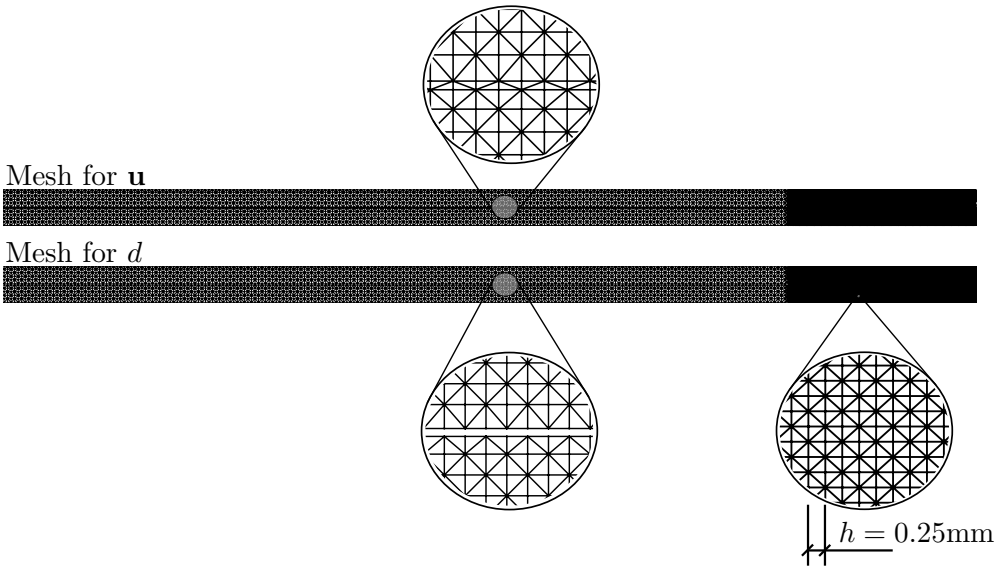

FIGURE 5.12: Locally refined discretization for the 2D laminated glass plane-stress model. Phase-field variable d is calculated on the sub-mesh in both glass layers only.

see the mesh in Figure 5.12. The reasons for this choice is that this 2D model takes into account the transverse compression of the interlayer, and provides a better way of visualisation of the crack evolution and its final pattern. Moreover, the more expensive plate formulation did not provide additional information and improvement as only one crack developed near the loading cylinder, recall Section 5.1.3.

The phase-field sub-problem, i.e. the damage evolution equation, is defined for the glass layers only (recall Figure 5.12). Therefore, the phase field is not continuous in the domain, and no crack can evolve in the interlayer. This assumption is in agreement with the displacement-controlled tests when the fractured glass did not break into pieces, as the shards were still connected to the foil, see Figure 5.11.

Note that this modelling choice implies the homogeneous Neumann conditions on glass layer boundaries Using the same mesh for $\boldsymbol{u}$ and d variables would imply the homogeneous Dirichlet boundary conditions at the glass-polymer boundary that result in interfacial crack branching, see, e.g., Figures 21 and 22 in [128] and the accompanying discussion.

5.3.1 Four-point bending tests on solid laminated glass samples

The numerical model is validated against the experimental data for the first loading stage, i.e., until the fracture of one glass layer. For laminated glass, the vertical displacements denoted as w in Figure 5.13 do not correspond to the prescribed positions of the loading head, but to the deflections at the midspan measured during the bending tests, see Figure 5.11. The fracture energy was set according to Eq. (3.22) using the extreme tensile strengths measured during the experimental testing, Table 5.4.

For both foils, we achieved a very good agreement with the experimental data for the normal stresses and the overall force reaction of the laminated plate. The numerical prediction is slightly stiffer for some of the laminated glass plates. The reasons for this small overestimation could be the deviations in material properties or dimensions due to the production tolerances. Because the shear coupling is higher for the numerical model, the error in the failure deflection for the failure stress of 69 MPa is about 4% and the fracture occurs for slightly lower numerical deflection. On the other hand, the numerical and experimental response corresponding to the minimal failure stress of 28 MPa fits well, the error in deflections is about 1%. For the EVA-based samples, the error in failure deflections is 1% for the largest failure stress of 60 MPa and 3% for the lowest value of 32 MPa.

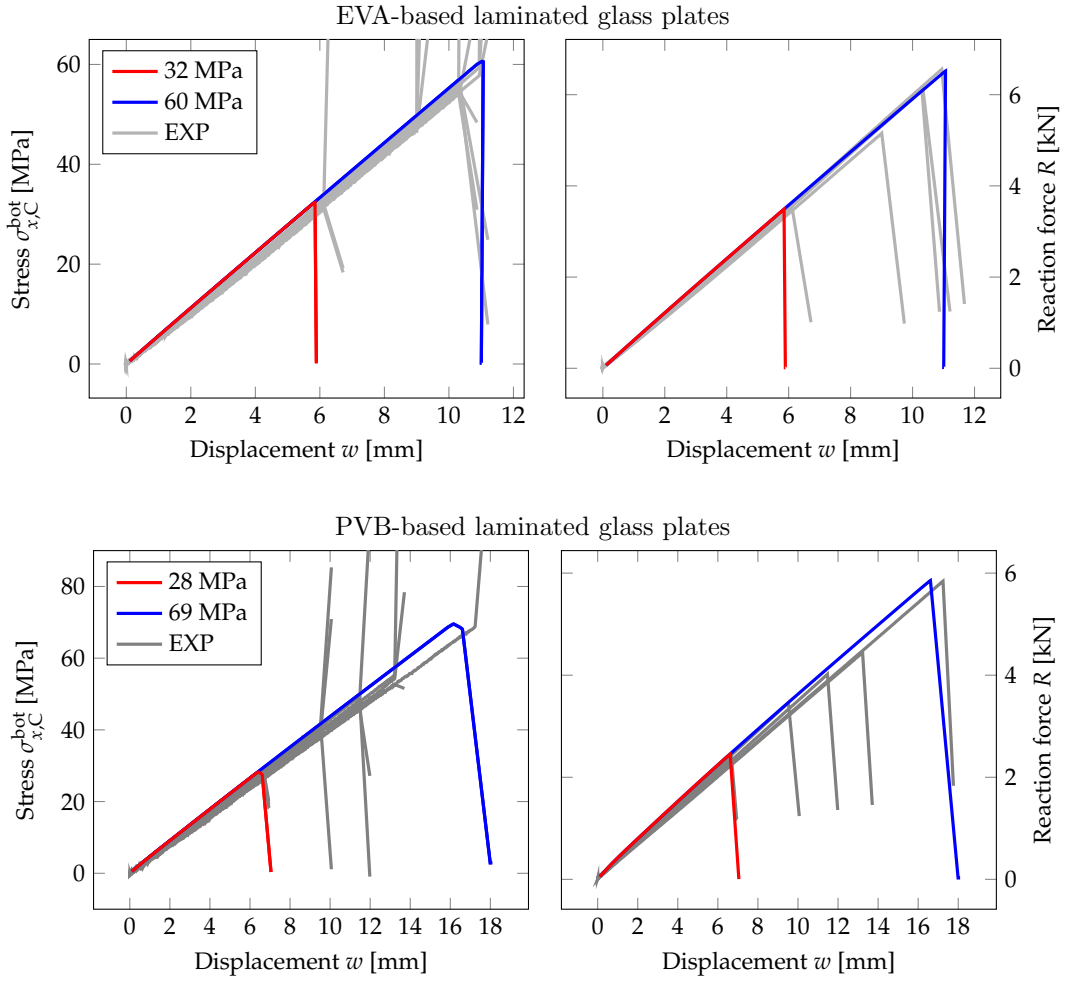

FIGURE 5.13: PF-P formulation, anisotropic staggered approach with the spectral-decomposition split, PS model: Evolution of the largest tensile stress at the midpoint and the overall reaction force under the loading points with respect to the midpoint deflection. Experimental data (EXP, grey lines); numerical response for the lowest measured failure stress (red) and for the highest value (blue).

The numerical prediction of the crack evolution obtained by the phase-field fracture model is shown in Figure 5.14. The first row corresponds to the crack initiation and the second to the position of the localised cracks for both types of laminated glass. Even for

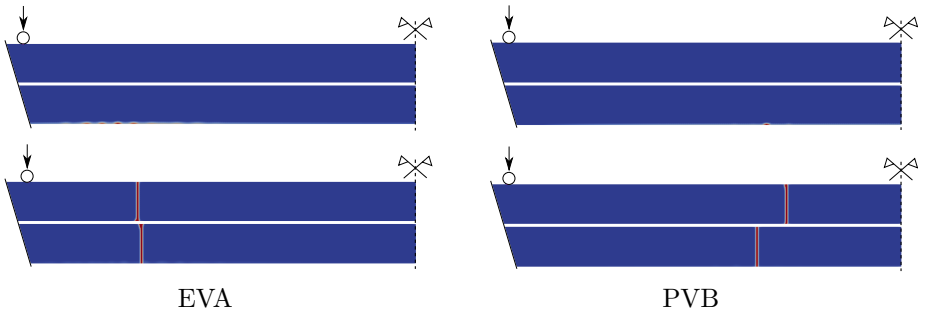

FIGURE 5.14: PF-P formulation, anisotropic staggered approach with the spectral-decomposition split, PS model: Crack initiation and localised cracks laminated glass samples under four-point bending.

a very fine increment of the applied displacement $\Delta w = 3 \times 10^{-5}$ mm, the cracks appear in both glass layers at the same converged step of the staggered algorithm. For EVA-based samples, the phase-field parameter evolves in a few bumps closer to the loading cylinder, and the cracks localised in glass layers are almost above each other. For the PVB-laminated glass, the bottom crack starts to evolve from only one initial point, and the upper crack is shifted to the centre.

5.3.2 Four-point bending tests on laminated glass samples with one layer fractured

During the experimental testing, the bottom glass layer was damaged first for the majority of tested samples, and multiple cracks evolved, see Figure 5.16. Then, the sample was unloaded, and the fracture of the second ply and so the collapse of the laminated glass sample occurred during the second loading stage.

To numerically simulate this second stage of loading and so the residual resistance of the fractured plate, we defined initial crack patterns in the bottom glass layer, consisting of one, three, or six cracks for a half of the sample, Figure 5.15. The cracks were defined by setting the initial phase-field variable to one with the width of the initial cracks $2l_c$. This simulations were performed only for the EVA-based laminated glass samples, and the final crack patterns are shown in Figure 5.15. Again only one crack localised in the upper layer.

Figure 5.17 illustrates the response of the EVA-laminated glass samples with the bottom layer fractured assuming the largest failure stress of 60 MPa. The evolution of compressive stresses on the upper surface at a quarter of the midspan and the overall reaction force are plotted for the mid-span displacement. In this case, the tensile stresses are not validated due to the fracture in the bottom glass and the inaccessible bottom surface of the upper glass layer due to the lamination.

The force-displacement diagram in Figure 5.17 shows the residual resistance of the laminated glass plate with one glass damaged. Two limits bound the stiffness of the samples:

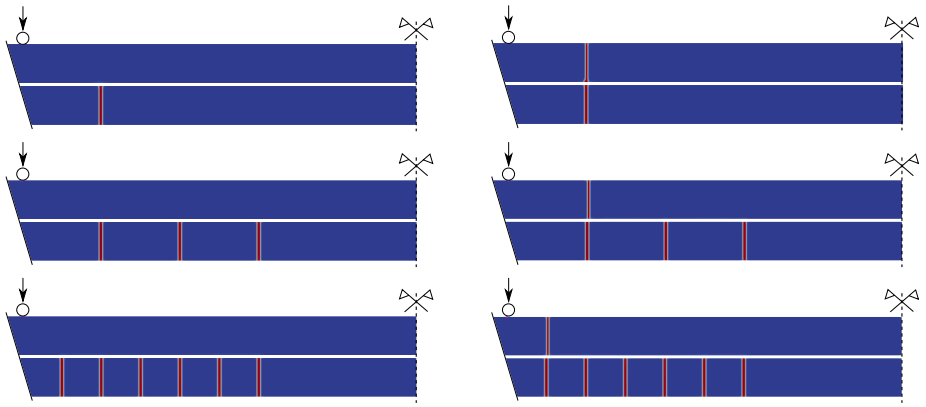

FIGURE 5.15: Phase-field variable in pre-cracked laminated glass under four-point bending with a different number of initial cracks in a symmetric half of the sample. Initial crack pattern in bottom glass ply and the final fracture for the EVA-based samples for PF-P formulation, anisotropic staggered approach with the spectral-decomposition split, PS model.

the upper limit corresponds to the behaviour of an undamaged laminated glass and the lower bound to the response of a single glass layer. The numerical model with one initial crack in a symmetric half of the bottom glass is stiffer than most of the experimentally measured responses. Therefore, the critical stress is also reached for a lower prescribed displacement. The force-displacement diagram fits well the experimental response for ANG-EVA-5 in Figure 5.16, where the damage after the first stage of loading is the lowest one for the EVA-based samples, and the sample is stiffer due to the triangular shape of the fracture pattern. Considering more initial cracks in the bottom glass under the largest bending moment results in the slopes of the stress-displacement and force-displacement diagram that match better the experimental data. The difference in the responses of a sample with three or six cracks (on a half of the area with the largest bending moment) is small. Because we neglected the weight of the fractured glass sample, the numerical post-fracture response does not correspond exactly to that what was observed in the experiment.

This analysis revealed that the stiffness of the partially fractured laminated glass can be approximated even with a 2D plane-stress model with initially predefined cracks. The numerical model matched the experimentally measured response very well and provides better estimation than a one-glass-layer limit.

5.3.3 Beam model for laminated glass and influence of interlayer

Finally, Figure 5.18 compares the numerical response of EVA-based and PVB-based laminated glass samples using the PS model and the B model, corresponding to the plane-stress model of the longitudinal cross-section and to the three-layer beam respectively. For the loading rate of 0.03 mm/s, the EVA interlayer provides better shear

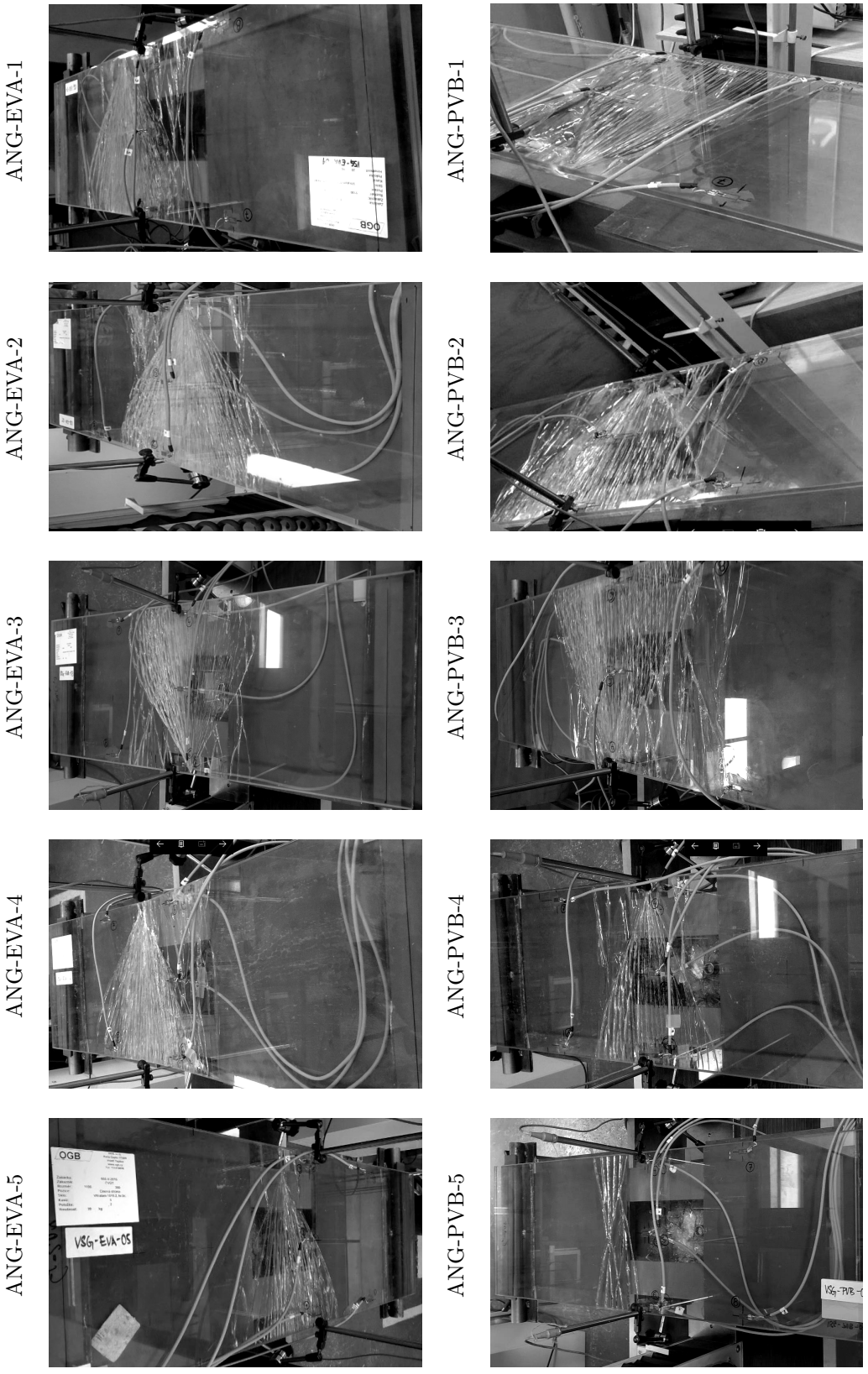

FIGURE 5.16: Fracture pattern after first loading for laminated glass samples. Both glass layers were damaged for ANG-EVA-4, whereas the fracture patterns for the other samples correspond only to the fracture of the bottom glass layer; courtesy of Tomáš Hána from CTU in Prague.

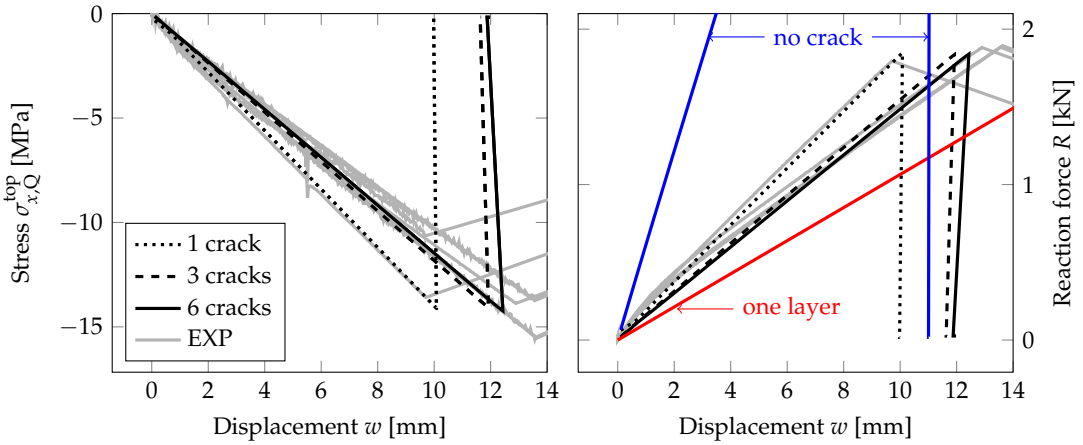

FIGURE 5.17: PF-P formulation, anisotropic staggered approach with the spectral-decomposition split, PS model: Evolution of the compressive stress at a quarter of midspan and the overall reaction under the loading points for the mid-span displacement for the second stage of loading and the EVA-based laminated glass plates. Experimental data (EXP, grey lines) and numerical response for one failure stress of 60 MPa (black) with a different number of initial cracks.

coupling, and the response of the laminated glass sample is stiffer than that of the PVB-samples. Therefore, the critical tensile strength is reached earlier; the fracture occurs for lower deflections, but the resistance of the sample is higher for EVA-based samples.

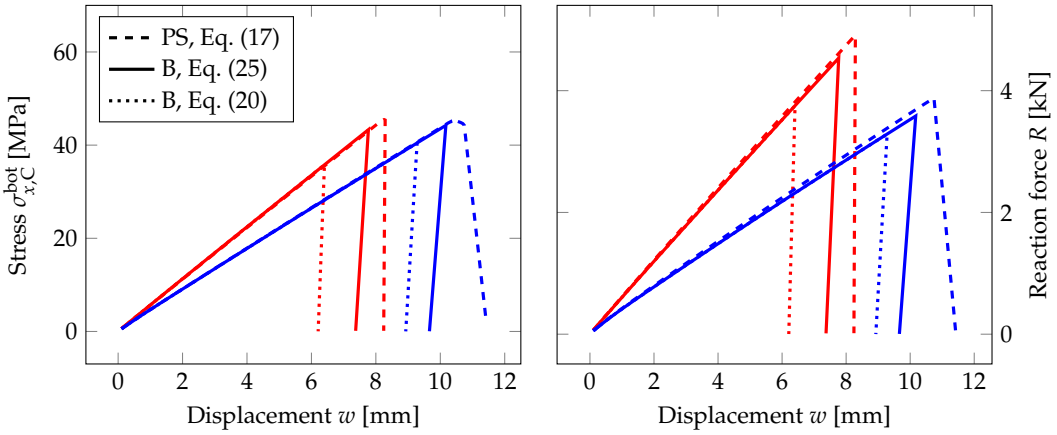

FIGURE 5.18: PF-P formulation, anisotropic staggered approach with the spectral-decomposition split: Comparison of the response of laminated glass plates with EVA (red line) or PVB (blue line) using the plane-stress (PS) or beam formulation (B). The evolution of the largest tensile stress at the midpoint and the overall reaction under the loading points for the midspan displacement. The bending strength of glass is set to 45 MPa.

For laminated glass Eq. (4.36) relating the fracture energy G_f, the length-scale parameter l_c, and the critical stress f_t cannot be applied for the B model, as it was derived for beams under pure bending only. In reality, normal forces arise from the stress redistribution in both glass layers due to the shear coupling by the interlayer. A simple approach to overcome this problem is to drive the phase-field evolution by the positive elastic energy density on the surface in tension.

As the B-model assumes a constant value of the phase field variable through the thickness, the governing equation of damage evolution is integrated over the cross section to obtain

$$\frac{A}{c_\alpha}\left(\frac{\mathrm{d}\alpha(d)}{\mathrm{d}d} - 2l_\mathrm{c}^2\,\frac{\mathrm{d}^2 d(x)}{\mathrm{d}x^2}\right) = -\frac{l_\mathrm{c}}{G_\mathrm{f}}\,\frac{\mathrm{d}g(d)}{\mathrm{d}d}\int_A \psi_\mathrm{e}^+\,\mathrm{d}A, \tag{5.3}$$

where A is the transverse cross-sectional area. Therefore, the phase field evolution is driven by the stored energy density integrated over the cross-sectional area under tension instead of the extreme value at the surface fibres. To modify this behaviour, we replace the right-hand side integral with

$$\int_A \psi_\mathrm{e}^+\,\mathrm{d}A \approx \frac{EA}{2}\max\left(\langle\varepsilon(x,h/2)\rangle^2, \langle\varepsilon(x,-h/2)\rangle^2\right), \tag{5.4}$$

where the strain $\varepsilon(x,z) = \frac{\mathrm{d}u}{\mathrm{d}x} + z\frac{\mathrm{d}\varphi}{\mathrm{d}x}$ is obtained from the centerline horizontal displacement u and cross-sectional rotation φ. This modification of driving force is performed for each glass layer separately, so a crack evolves through the layer once a critical value is reached on one of its surfaces.

The comparison in Figure 5.18 shows that the through-thickness compression of the interlayer does not affect significantly the response. The differences in the slopes of the force-displacement diagram for both formulations are negligible. The glass fracture occurs for the beam formulation earlier as the criterion is set according to the bottom surface, but the differences are considerable smaller than for the parametric studies performed in Section 5.1.

5.4 Conclusions

Using the phase-field fracture models, we studied the brittle response of monolithic and laminated glass plates under bending with the goal

- to compare three different modelling strategies based on the phase-field fracture formulations and analysed the extent of the nonlinear part of the expected linear pre-fracture response,
- to discuss the possible dimensional reduction of the problem together with the setting of the length-scale parameter and adjusted fracture energy of glass,
- to illustrate how the fracture for the four-point bending tests initiated from glass edges could be enforced,
- to predict the response of laminated glass with one layer fractured.

The main contributions of the presented study are:

- For thin plates under bending, the nonlinear response due to the damage before the crack localisation can be significant for some phase-field formulations. This effect can lead to a considerable overestimation of the response.

- The fracture energy of soda-lime-silica glass results in a very small length-scale parameter. For numerical purposes, the fracture energy should be determined concerning the applied dimensional reduction, loading type, and the value of the length-scale parameter compared with the thickness of the structure under bending. Then, a consistent value of the tensile strength corresponds to the glass fracture.

- Two possible ways of the fracture energy scaling were introduced in this study for beam or plate models. For a one-layer monolithic glass plate under bending, the scaling relations were derived from the evolution equation using a spatially homogeneous solutions. For multi-layer plates, the phase-field evolution can be driven by a positive energy density on a surface in tension as suggested in this study.

- For the plate model, the strength has to be reduced in a band or area of sufficient dimensions and not only at nodes directly on the edges to reproduce the cracking initiated at edges.

- The comparison showed that the numerical model provides a very good agreement with the measured stresses and resistance of laminated glass, even though only one/two cracks developed for all discretisations using the quasi-static solver, whereas multiple cracks evolved during the experiment.

- The stiffness and resistance of the partially fractured laminated glass can be approximated with a 2D plane-stress model with initially predefined cracks. The model matched the experiment very well and provided much better estimation than a one glass layer limit.

- For quasi-static loading of laminated glass, the presented examples also validated the time/temperature-dependent material properties of the Ethylene-Vinyl Acetate or PolyVinyl Butyral interlayers derived recently by the authors in [63].

The next step of this study will be to extend the model to incorporate the effect of the stochastic strength of glass.

Chapter 6

Stochastic fracture analysis of laminated glass beams

This chapter deals with the computational modelling of multi-layer laminated glass. The four-point bending tests of rectangular plates supported along two edges provided a data-set for validation of the numerical simulations. In our experimental study, we examined the load-bearing capacity of PVB-laminated glasses with two different cross-section layouts consisting of three or four glass plies bonded with plastic interlayers. In the numerical description, we rely on the finite element analysis complemented with the phase-field fracture description for brittle glass layers. The phase-field model with an elastic phase is employed to avoid stiffness degradation at low-stress levels which is enhanced by stress-based Rankine-type crack criterion. To reproduce the variation of the tensile strength of glass due to surface micro-defects, we try to account for this randomness in our model using randomisation in material properties or the initial phase-field variables.

In the design practice, effective thickness approaches are widely used for stress analysis of laminated glass. However, these analytical approaches have been so far derived for multi-layer composite beams made of three glass layers of any thickness or multiple glass plies with a constant layer thickness [55]. As we deal with laminated glass with multiple layer thicknesses, we rely on the finite element analysis complemented with the phase-field fracture description for brittle glass layers, which is presented in Section 4.1 supplemented by implementation details in Section 3.2.4. In the numerical model the parameters follow the experiments and the tensile strength of the glass under bending is described by the Weibull distribution, see Section 6.1. After a few numerical tests in Sections 6.2, the model is validated against an experimental data measured during quasi-static four-point bending of thin multi-layer laminated glass, Section 6.3. The main findings are summarised in Section 6.4.

6.1 Experimental setup

The main motivation for development of multilayer phase-field damage model is the validation of experimental data. The 5- and two type of 7-layer laminated glass beams were tested at the Faculty of Civil Engineering, Czech Technical University in Prague. Similar experimental setup as presented in Section 5.2.3 was used. The samples were loaded by prescribed displacement with four-point bending static scheme. The schematic experimental setup is plotted in Figure 6.1 and 6.2 which also shows the position of displacement and strain gauges. The exact experimental description is available in previous section.

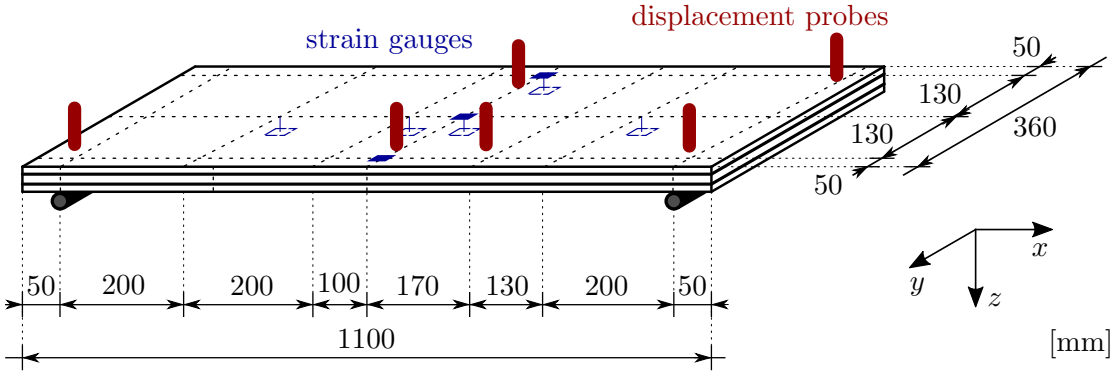

FIGURE 6.1: Experimental setup of four-point bending test and displacement/strain gauges positions.

The geometry and boundary conditions of numerical tests follow the experimental setup. Four point bending of 5- and 7-layer laminated beams were loaded by prescribed displacement until their fracture. The dimensions of the numerical model as well as the dimensions of the experiments are shown in Figures 6.1 and 6.2. Moreover, the out-of-plane width is 0.36 m and overall thickness is 20.04 mm for 5-layer and 29.04 mm/27.8 mm for 7-layer laminated glass, see Table 6.1 for thicknesses of individual layers. Apart from the laminated configuration, we perform numerical test on one-layer glass beam, which have the thickness 20 mm and the remaining dimensions are unchanged, this test is presented in Appendix 1.

	5LG	7LG-1	7LG-2
number of layers	5	7	7
thicknesses [mm]	5/2.28/6/0.76/5	5/1.52/8/0.76/8/0.76/5	6/1.52/6/0.76/6/1.52/6
overall th. [mm]	20.04	29.04	27.8
width b [mm]	360	360	360
length l [mm]	1100	1100	1100
glass type	annealed	annealed	annealed
interlayer	PVB	PVB	PVB

TABLE 6.1: Composition of laminated glass samples and nominal dimensions

The glass is supposed to be linearly elastic material with Young's modulus $E = 70$ GPa and Poisson ratio $\nu = 0.22$. In contrast, polymer foil used as interlayer is rate dependent viscoelastic material. Its behavior can be sufficiently described by generalized Maxwell

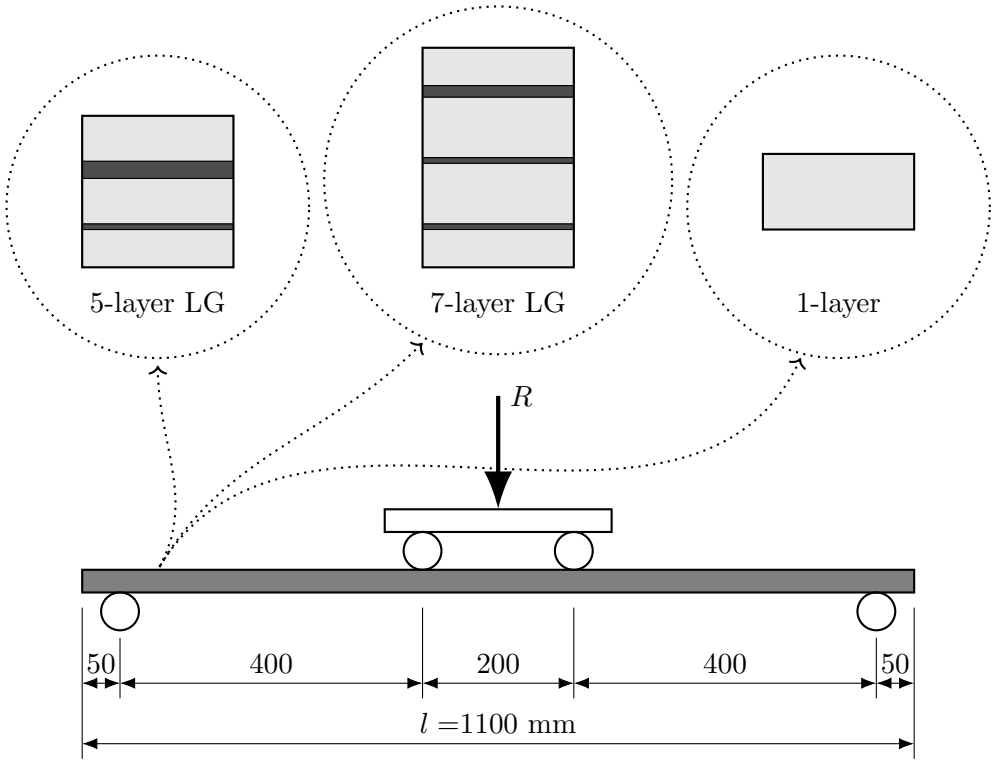

FIGURE 6.2: Scheme of the four-point bending test on multi-layer laminated glass plates

model with finite number of individual Maxwell units. This approach was investigated by the authors for this particular PVB foil, therefore the parameters of generalized Maxwell models was used from their article [63].

The remaining parameters are two independent constants from dissipation functional (4.16): the fracture energy G_c and the internal length l_c. The latter is treated as a purely numerical parameter, which is always chosen twice the minimal element length. The former is determined indirectly. Instead of fracture energy G_c, the governing parameter is tensile strength f_c and the fracture energy is evaluated based on 1D relationship

$$G_c = \frac{8}{3}\frac{f_t^2 l_c}{E}. \tag{6.1}$$

Despite the fact that identity (6.1) was derived for 1D bar under tension/compression, its validity remains also in our model. It is caused by using the driving term (4.18), which makes the dissipation functional (4.16) having the same structure.

The tensile strength f_t of glass is highly dependent on the surface and edge defects, i.e. the damage resulting from manufacturing, processing, transport and manipulation. For unknown initial flaws, the strength can be described stochastically, using the experimental data set from the bending tests on glass.

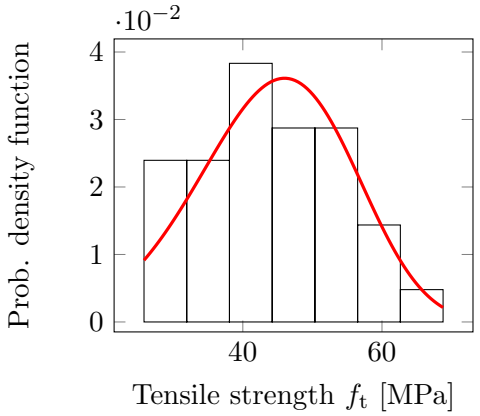

FIGURE 6.3: Histogram of experimentally obtained failure stresses and fitted probability density function defined as Weibull distribution.

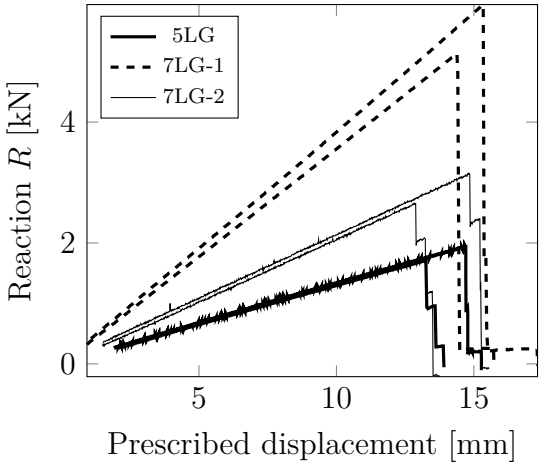

FIGURE 6.4: Reaction evolution of experiments

Our collection of glass strengths consist of two independent data sets. First 24 values, taken from literature [142], were supplemented by 10 values obtained from our experiments [157]. These 34 failure stresses are not explicitly listed here, but they are published in gitlab repository [73] accompanying this thesis. For visualization of the experimentally obtained strengths see histogram in Figure 6.3. The stochastic strength of glass expressed in MPa is described by Weibull distribution with shape parameter $k = 4.64$ and scale parameter $\lambda = 48.47$, which were fitted for given failure stresses. Therefore,

$$f_t \sim \text{Weibull}(k = 4.64, \lambda = 48.47). \tag{6.2}$$

Note that we consider the polymer foil to have infinite strength and we also assume zero relative displacements on the glass-foil contact.

6.2 Combinatorial limit analysis

It can be seen from experiments, represented here by reactions evolution in Figure 6.4, that in some cases the laminated structure cracks gradually. In contrast to this experimentally observed behavior the phase field damage model with homogeneous distribution of strength predicts different response. During the staggered iterations for an individual time instant, the crack is initiated in the bottom layer and immediately propagates across all remaining layers. How the simulate the exact glass breaking and whether the phase-field is capable to simulate the fragmentation in quasistatic regime remains open question [43]. One way to overcome this difficulty is to artificially increase the strength of inner glasses to stop the crack propagation. Since the bottom and the top layers are more prone to surface defects and therefore break more easily, this is also partially in accordance with the real behavior although this effect cannot be sufficiently quantified. To investigate capabilities of such simplified approaches, it is appropriate to check behavior in limit cases.

In the following, we investigate the response of composite plate in which the strength of the glass layer is either 5% or 95% quantile of the strength distibution. In particular

$$f_{\mathrm{t,min}} = F_{f_\mathrm{t}}^{-1}(0.05) \doteq 25.6\mathrm{MPa}, \quad f_{\mathrm{t,max}} = F_{f_\mathrm{t}}^{-1}(0.95) \doteq 61.4\mathrm{MPa}, \tag{6.3}$$

where F_{f_t} is cumulative distribution function of f_t. The maximum or minimum strength is applied to individual layer. Distribution across length is assumed constant. All 2^3 resp. 2^4 combinations of $f_{\mathrm{t,min}}/f_{\mathrm{t,max}}$ is investigated for 5-layer resp. 7-layer laminated beam. Although these combinations of extremely high and extremely low strengths are unlikely to occur in the structure, this investigation will give us an idea whether such variation of strength can explain the observed qualitative difference in failure modes.

6.2.1 5-Layer beam

In this section the results of the 5-layer laminated beams are presented. As mentioned, the numerical setup follows the experiments, recall the schematic overview in Figure 6.2. The beams are loaded by prescribed displacement and the reaction of beam is measured. The evolution of reaction R is plotted in Figure 6.5 supplemented by the bar chart showing the individual layers integrity until the crack initiation. These graphs call for some remarks.

Each type of line represents individual data series for different combination of minimal and maximal strength in layers. The concrete combination is specified in legend, where layers are arranged from bottom to top layer. For example 'min − max − max' indicates a beam whose bottom glass layer has strength $f_{\mathrm{t,min}} = 25.6$ MPa and the middle and top layers have strength $f_{\mathrm{t,max}} = 61.4$ MPa. Further the red and blue is the stochastic

envelop. The red one is closely followed by variant min − min − max, where the one cracks developed through all layers also. The other variants crack gradually and no progressive collapse occur. The combinations min − max − min, min − max − max and max − max − min can represents single-sided or double-sided scratched laminated glass from transportation or manipulation. Nevertheless their damage mechanism differs. The first one, scratched from both side, cracks firstly on the bottom layer. The top layer cracks only after further loading and the middle layer still withstand another load for a while before it collapses. On the other hand cracks appear in the weakest layer in one-side variants min − max − max and max − max − min. After additional loading more cracks appears in the same layer instead of the development of a crack into the next layer. Only in the time instant of the collapse the crack forms across the remaining two layers. The combination min − max − min exhibits the same behavior, but the fragmentation occurs in the middle layer. Damage evolution of these representatives samples is graphically illustrated in Figure 6.6.

6.2.2 7-Layer beam

Similar extreme-cases analysis was performed for the 7-layer beams as in previous sub-section. The particular results are primarily presented in Figure 6.7, where the evolution of reaction R is plotted. For the visual clarity, only 8 representative combinations are actually plotted. The second graph displays the period of time when given layer is intact similarly as for 5-layer case. Finally the sequence and positions of cracks displayed the Figure 6.8.

Similar results as for the 5-layer configuration were observed. However to conclude this section we bring two main observations from deterministic extreme-cases analysis:

- The same strength in all layers cannot predict gradual cracking of individual layers. Nevertheless the non-uniform strength field across layers in model may exhibits such behavior.
- The same results is valid for phenomenon of several cracks occurrence in one layer.

6.3 Stochastic approach

The previous section give us the idea of qualitative capabilities of phase-field model with different strengths in individual layers, but a representative combinations remain highly unlikely to occur. To investigate the model also quantitatively we perform stochastic analysis in this section.

We assume that the tensile strength is still constant along the length of the beam, but in each glass layer the strength is generated individualy from the Weibull distribution (6.2).

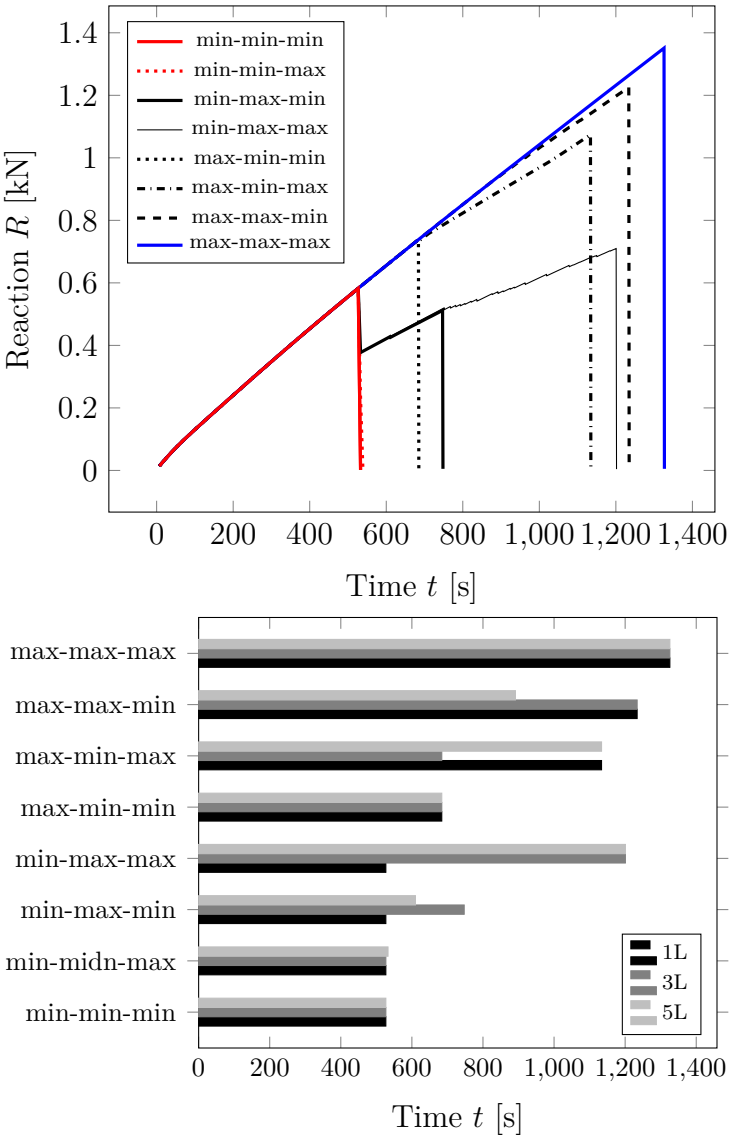

FIGURE 6.5: Evolution of reaction force R (top) and evolution of layers integrity (bottom) for individual combination of minimum and maximum stochastic strengths in 5 layer laminated beam (3 layers of glass). The first word before the dash in legend represents the lowest glass layer.

The experiments from [142] or [157], which lead to our strength set, was performed on laminated glass beams with almost the same length around one meter and the distribution (6.2) describes the structural strength rather that material point strength. Since our experimental setup follows this setting, we can assume the same distribution at structural level. From this point of view the presented stochastic approach is legitimate.

Recall that the damage is driven by a modified driving force (4.18) which ensures that the crack initiates after surface tension exceeds the randomly selected strength. Also recall that the interlayers have infinite strength. The representative bunch of such stochastic realizations for model introduced in Section 4.1 is shown in Figure 6.9, where the evolution of the reaction force for 5L, 7L and 7L-2 beam model is presented. The simulations

FIGURE 6.6: Cracks development for representative combinations min-min-min, min-max-min and min-max-max in 5-layer laminated glass.

are rendered by grey colour, whereas experiments are red. There was common quadratic rise of red curve due to on the indentation of the sample into the rubbery support pad. This inconsistency was eliminated by shifting the data such that the linear regression of data from time interval $\langle 2; 4\rangle$ strikes the origin. This initial stages of experiments were cut off and are not presented in the graphs. Finally, the last (blue) line shown average behavior by selecting all strength as $f_{\mathrm{t,\ mean}} = 44.79$ MPa.

The linear part of diagram is validated appropriately since the experiments relatively copy the simulations. The slight discrepancy in slope can be consequence of ignoring rate-dependency of foil. The rule $G(t/2)$ presented in section 5.2.2 systematically underestimate the foil stiffness as was concluded in [131]. There is evident that several realizations show a sudden drop of reaction force which indicates a gradual cracking. The better visualization can be seen from top part of Figure 6.10, where histograms

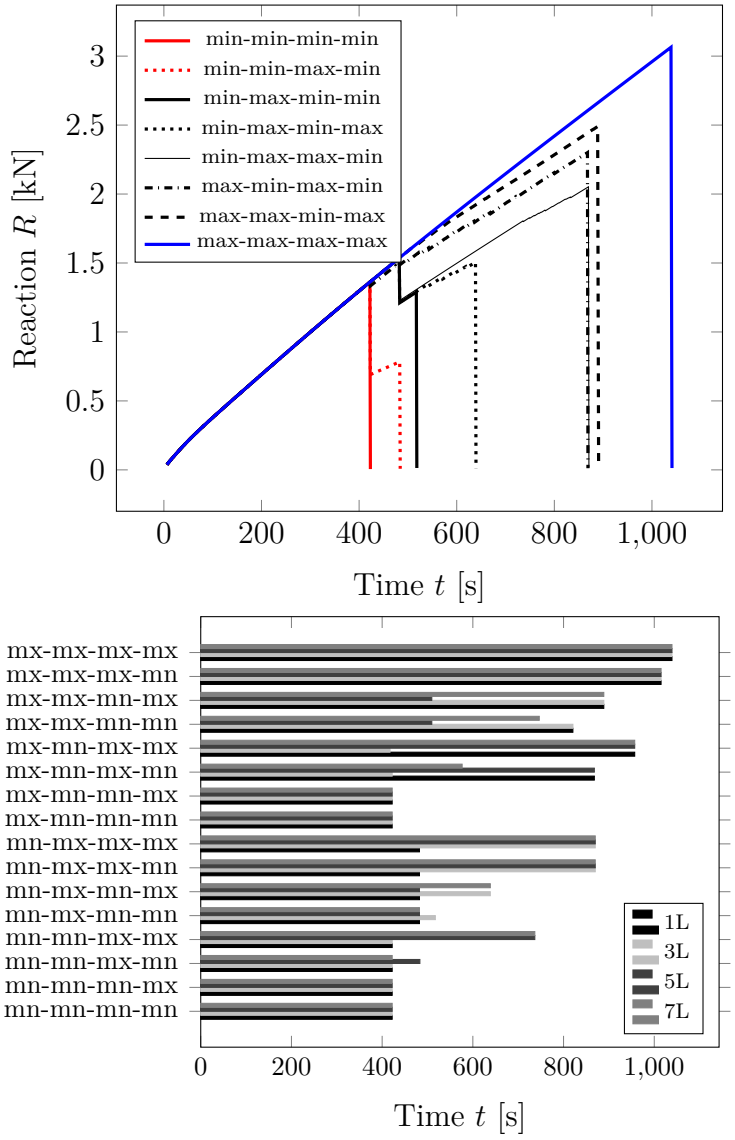

FIGURE 6.7: Evolution of reaction force R (top) and evolution of layers integrity (bottom) for individual combination of minimum and maximum stochastic strengths in 7 layer laminated beam (4 layers of glass). The first word before the dash in legend represents the lowest glass layer and the words max, min are shorten to mx, mn for clarity.

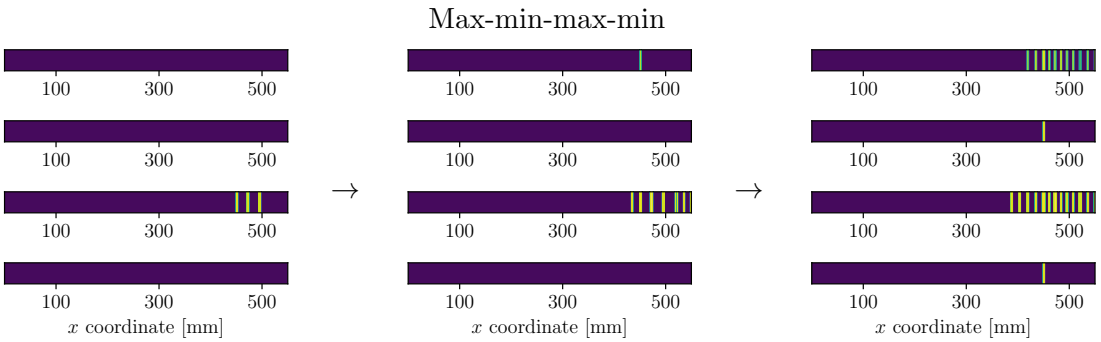

FIGURE 6.8: Cracks development for combination max-min-max-min in 7-layer laminated glass.

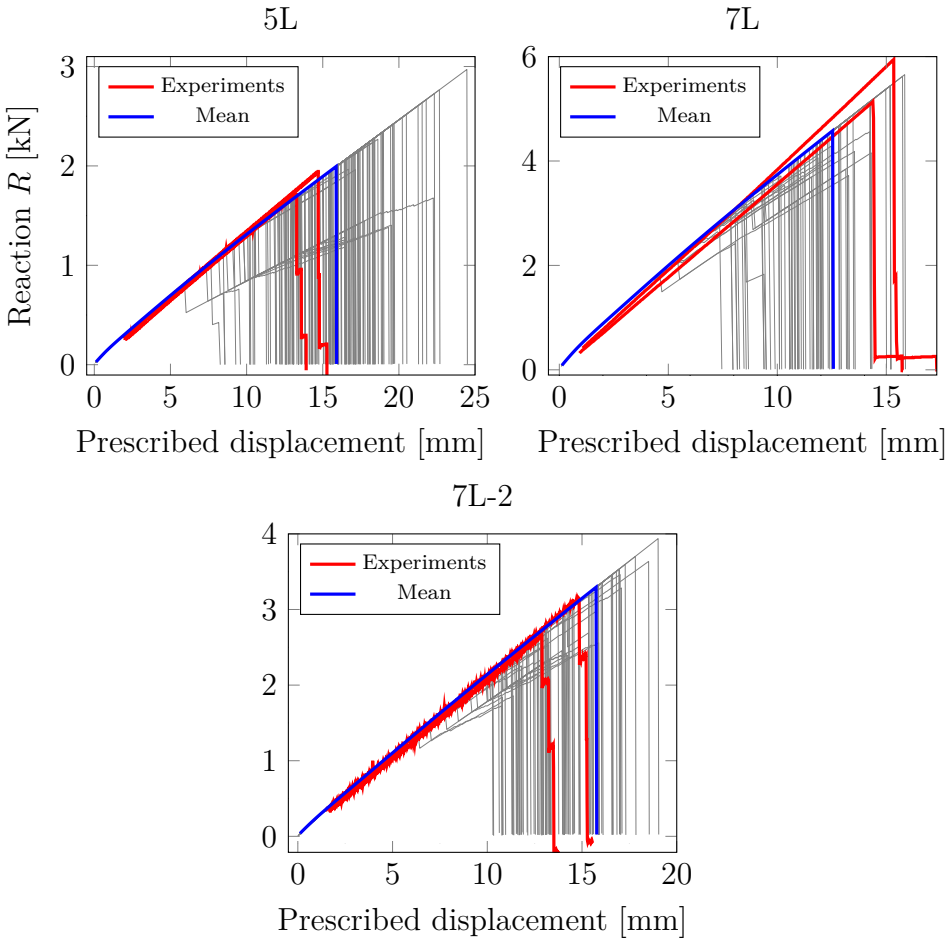

FIGURE 6.9: Evolution of total reaction of laminated glass beam for representative 100 stochastic realizations (gray), experiments (red) and mean-strength laminated glass (blue).

of prescribed displacements for 1000 realizations are plotted. The blue bars represent histogram of the onset of the first crack and the solid line of the same colour is a fitted Weibull curve. The red bars and red solid line represent similar phenomenon but for failure displacement - the instant of total failure of the beam, i.e. when cracks develop in all layers. The bottom part of Figure 6.10 is a scatter plot where each point is one stochastic realization with failure displacement as vertical coordinate and crack-initiation displacement as horizontal coordinate. These data indicates that, in the stochastic manner, the first crack is induced by smaller prescribed displacement than the total collapse and the crack does not propagate through all layers simultaneously but rather gradually. This is also supported by a scatter plot. Although plenty of points lies on the diagonal, still high amount of points have relative difference between first-crack displacement and failure displacement. This is quantified in table 6.2, which summarizes the number of occurrences where the failure displacement is greater by a certain value than the first-crack displacement.

The graph in Figure 6.11 also shows the percentage of given failure sequences, where it

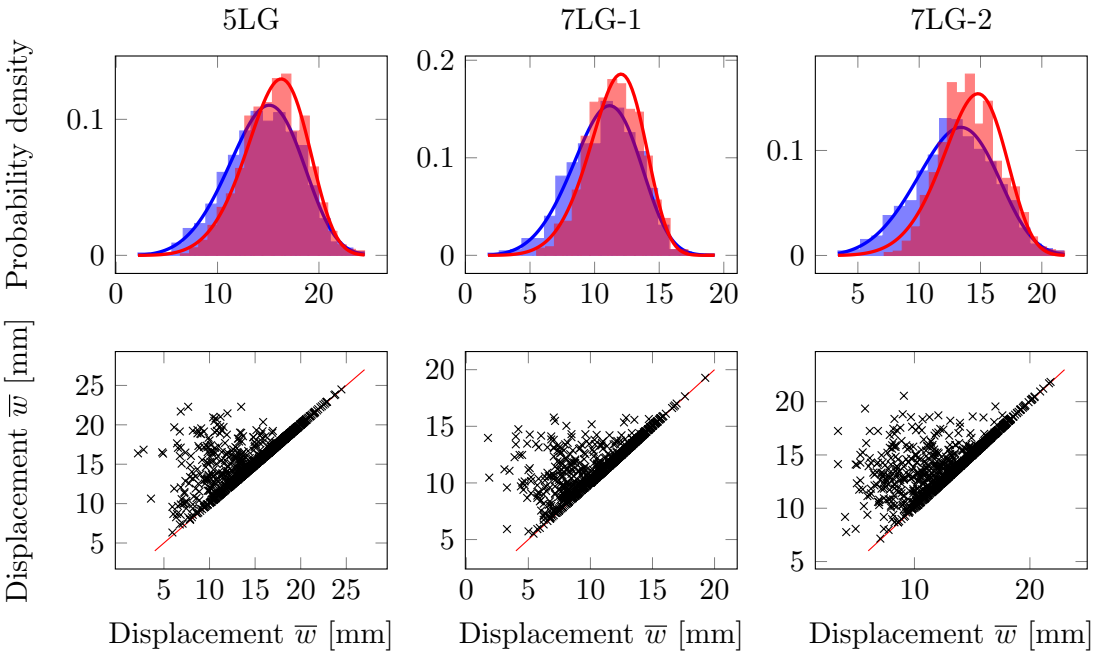

FIGURE 6.10: Histograms of displacements inducing first crack (Blue) and histogram of failure prescribed displacements (Red) for 5-layer (left) and 7-layer (right) laminated glass.

Case	Greater than 1%	Greater than 5%	Greater than 10%
5L	29.2	24.1	20.5
7L	43.9	26.0	20.8
7L-2	40.6	32.4	27.1

TABLE 6.2: Occurrence of observations where failure displacement is larger than first-crack displacement in percents.

can be seen that the most frequent failure is rapid one - all layers are damaged at the same time. The second most common sequence is cracking from below, where the tensile bottom plate cracks first and then the rest of the structure. The strength distribution for this second most frequent sequence, see Figure 6.12, shows that the strength is statistically lower for the bottom layer. It can be concluded from this that gradual cracking can only be achieved if the bottom layer is significantly weaker than the other layers. This indicates that real laminated glass does indeed have exposed layers that are less strong, but this cannot be proven from this analysis.

6.4 Conclusion

A brittle material such as glass suffers from fragmentation - it produces more cracks rather than one in the area of highest stress, even under quasi static loading. Capability of phase field approach to model this phenomena is under investigation, see [43], but it is

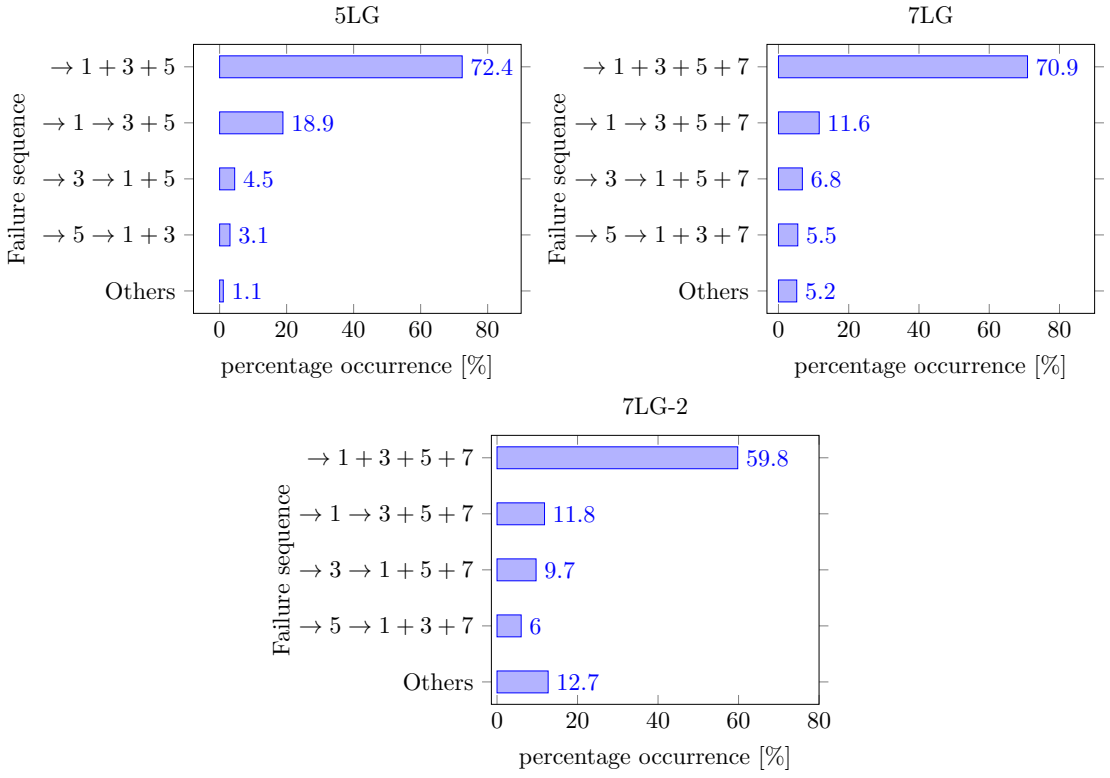

FIGURE 6.11: Percentage occurence for different failure sequences.

not fully understood. The alternative approach is stochastic simulation as is presented in this study.

In particular, the strength of material point is never known exactly, but from experiments and literature we have a strength distribution of laminated glass elements with length of approximately one meter. This means that the distribution already reflects the size-effect. As a result, we can generate one strength for each layer and consider it constant along beams length. On the other side, there is still lack of information whether the distribution differs in individual layers, or not.

The distributions in Figure 6.10 indicates the gradual cracking in stochastic manner, but probably this effect is even stronger. Since the bottom and top layer is more exposed to scratches and surface damage, the strength of these layers is probably lower than for inner glass layers. This assumption induces different (lower) strength distribution for outer layers, which makes gradual cracking even more frequent. With the available data this cannot be sufficiently quantified and therefore this idea remains a speculation.

The smallest slope of 7L experimental data in Figure 6.9 represents situation when all layers fail except the upper one. The main drawback of presented stochastic approach is its inability to model this behavior. No simulation lead to the crack developed in all but the upper layer.

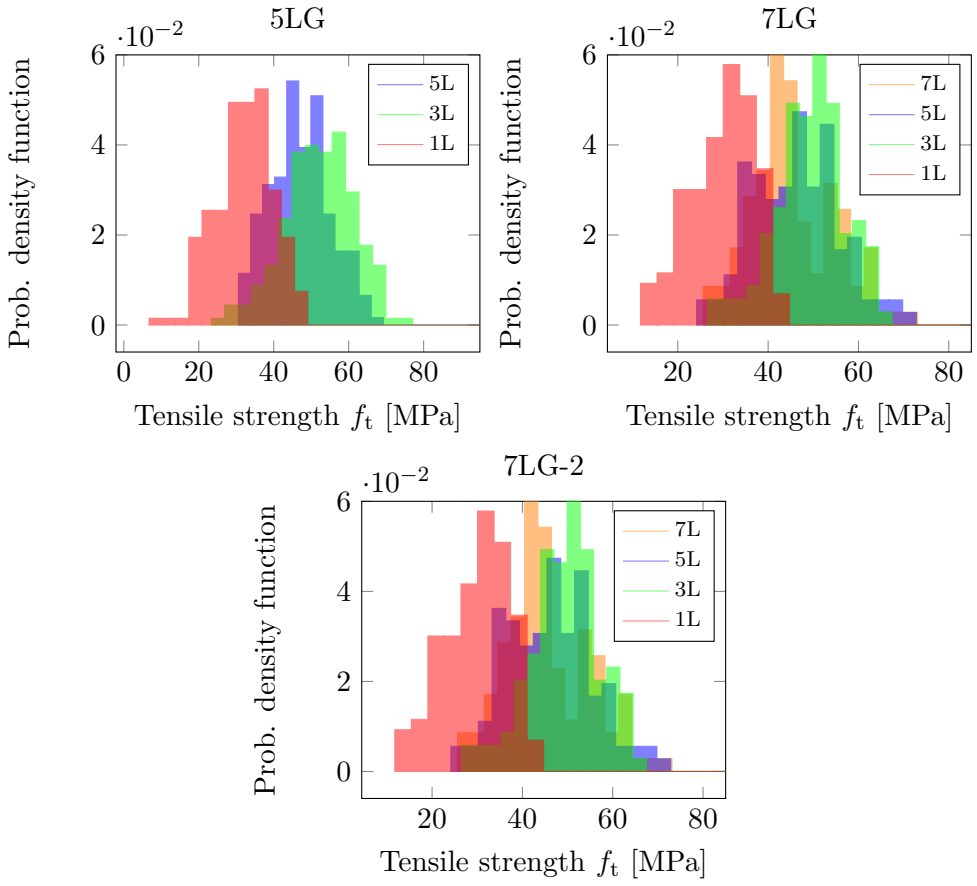

FIGURE 6.12: Strengths histogram for second most frequent case - the bottom layer cracks first followed by the rest of the structure.

The natural continuation of this research will assume a spatial variability of strength instead of a homogeneous distribution in individual layer. However, this approach requires discovering the relationship between structural strength distribution and strength distribution consistent with the phase-field model.

Chapter 7

Dynamic fracture in phase field models

This chapter is based on article [130].

Although a number of numerical techniques applied to float or laminated glass under dynamic load have been proposed, this research topic is still widely open to further investigation. See for example [146] for an extensive overview of numerical methods applied to float glass, where standard finite element method with the Rankine failure criterion is compared to the extended finite element method, the discrete element method, and their combinations. Similarly, some critical aspects and several modeling techniques applied to laminated glass structures are presented in [32, 139]. Application of peridynamic models [96] is also worth mentioning.

The present section examines the ability of the phase field model to simulate gradual fracture of a laminated glass subjected to several consecutive low velocity impacts. This issue has already been investigated in [155] with the help of commercial software LS-DYNA where the results of an extensive experimental program were also presented. Attention is therefore accorded to theoretical and computational aspects of the phase-field model in context of plates [85], while experimental measurements used to support our numerical implementation are outlined only briefly just for the sake of completeness. Proceeding in the footsteps of [155] the five (5LG) and seven (7LG) layer laminates consisting of three and four plies of a float glass bonded to a PVB (polyvinyl butyral) interlayers are examined, respectively. In particular, the ability of the phase field model to estimate the response of a laminated glass is tested by comparing the measured and simulated distributions of contact force and gradually evolving crack patterns.

7.1 Experiments

The concept of sacrificial-glass-ply design [81] was adopted in [155] to propose two specific geometries. In such a case, the outer glass layers are made thinner as they mainly serve to protect the inner glass layers, which in turn play the key role in accommodating the applied load. Additionally, the outer glass layers together with the polymer interlayers are expect to dissipate the impactor energy thus enhancing the bearing capacity of the laminated structure. Herein, the 5LG laminate is composed of three glass layers and two PVB interlayers whereas the 7LG laminate consists of four glass layers bonded with three PVB interlayers. An illustrative example of such a laminate is displayed in Figure 7.1. Geometrical details of both composites are stored in Table 7.1.

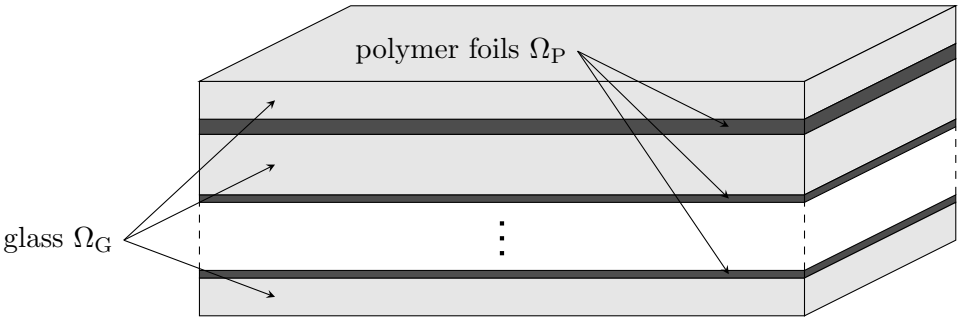

FIGURE 7.1: Example of a laminated glass

TABLE 7.1: Geometry of 5-layer (5LG) and 7-layer (7LG) laminated glass samples

	5LG	7LG
number of layers	5	7
glass type	float annealed	float annealed
interlayer material	PVB (TROSIFOL BG R20)	PVB (TROSIFOL BG R20)
number of tested samples	4	4
width b (mm)	500	500
length l (mm)	500	500
thicknesses of layers (mm)	5/2.28/6/0.76/5	5/1.52/8/0.76/8/0.76/5

The tested samples were suspended in vertical position on a pair of steel ropes along vertical edges to approximate a free boundary conditions [125], thus eliminating the effect of mechanical supports. The low velocity impact was induced horizontally via an 800 mm long pendulum device (impactor) having a cylindrical shape with a hemispherical nose with the diameter of 50 mm. The required impact energy, defined as the kinetic energy of the impactor $E_{\text{imp}} = 0.5 m_{\text{imp}} v_{\text{init}}^2$ with the impact velocity $v_{\text{init}} = \sqrt{2gh_{\text{imp}}}$, was achieved by dropping the 48.2 kg impactor from a given height h_{imp}. To examine the influence of subsequent impacts of growing intensity on a laminate fracture response the impact height was gradually increased by 5 cm as seen in Table 7.2.

For illustration, we present the results of three particular samples of the two laminates. The response of individual samples after individual impacts is summarized in Table 7.2. Considering the impacted glass on the left hand side, the empty circle $|\circ|$ indicates the onset of damage in a given ply, whereas the filled circle $|\bullet|$ identifies a glass layer which

TABLE 7.2: Overview of fractured glass layers after individual impacts including impact energies. With the left-hand side impacted, the symbols | • | indicate the previously fractured glass layers, empty spaces | | the unfractured ones, and circles |◦| the crack initiation in a glass layer

Sample		5LG–1	5LG–2	5LG–3	7LG–1	7LG–2	7LG–4
Impact Height (cm)	Energy (J)	Position of fractured glass layers after individual impacts					
5	24	| | | |	| | | |	| | | |	| | | ◦ |	| | | | |	| | | | |
10	47	| | | |	| | ◦ |	| | | |	◦ | | | • |	| | | | |	| | | | |
15	71	| | ◦ |	| | • |	| | | |	• | | | • |	| | | | |	◦ | | | |
20	95	| | • |	| | • |	| | ◦ |	• | | | • |	| | | | |	• | | | |
25	118	◦ | | • |	| ◦ | • |	| ◦ | • |	• | | | • |	| | | | |	• | | ◦ |
30	142	• | | • |	| • | • |	◦ | • | • |	• | | | • |	| | | | |	• | | | • |
35	165	• | | • |	| • | • |	• | • | • |	• | | | • |	| | | | |	• | | | • |
40	189	• | | • |	◦ | • | • |	• | • | • |	• | | | • |	| | | ◦ |	• | | | • |
45	213	• | ◦ | • |	• | • | • |	• | • | • |	• | | | • |	| | ◦ | • |	• | | | • |
50	236	• | • | • |	• | • | • |	• | • | • |	• | | | • |	◦ | ◦ | • | • |	• | | | • |

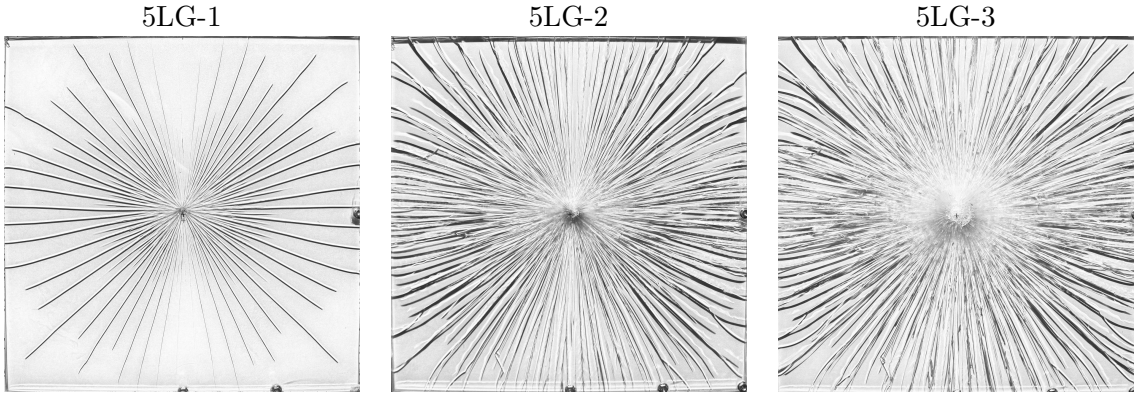

FIGURE 7.2: Final fracture patterns of 5LG samples

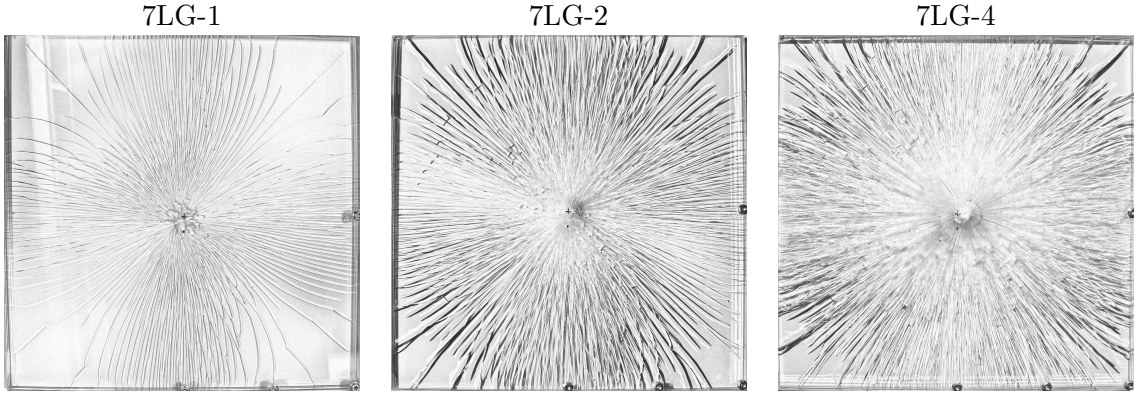

FIGURE 7.3: Final fracture patterns of 7LG samples

has already been broken during previous impacts. Empty spaces | | represent unbroken glass layers.

Although limited to three samples only, the results confirm the advantage of a sacrificial-glass-ply design which expects the outer glass layers to fracture, so the inner glass layers are still capable of sustaining additional impacts with higher energy. This is

particularly evident for samples where the impacted glass layer fractured at the initial stage of loading (5LG-1, 7LG-1, 7LG-3). Unfortunately, the results also show a certain degree of variability in the fracture response of the laminates potentially attributed to a random distribution of initial surface defects of the unprotected (outer) glass layers. This was also confirmed by our study on a single glass ply in [156] devoted specifically to the application of various damage models implemented in the LS-DYNA software. These findings make the predictive capability of any numerical model rather difficult especially in the framework of deterministic modeling. To perform stochastic simulations goes, however, beyond the present scope owing mainly to insufficient experimental data to identify, for example, a statistical distribution of the impact energies. Instead, we concentrate on tuning the computational model to represent one particular experiment. If successful, this will serve as a stepping stone for more complex stochastic analysis.

The final crack patterns are presented in Figures 7.2 and 7.3 showing a typical distribution of radial cracks of different lengths seldomly connected by short parts of secondary cracks. Also notice that apart from the diagonal cracks the cracks bend to arrive at the sample edges in a perpendicular direction. This yet will be discussed when comparing the fracture patterns with numerical predictions.

7.2 Model selection

The phase field model, as reported in Section 3.2, is determined by the decomposition of strain energy density into active ψ^+ and passive ψ^- parts and by the selection of function $\alpha(d)$.

The most physically sound response is simulated by using the spectral decomposition of the functional (3.11) proposed in [102]. However, this decomposition contains singularities in the finite element application and resulted in instabilities in our simulations. On the other hand, stable solutions were experienced when considering the decomposition based on a volumetric-deviatoric split as suggested in [11]. The active and passive contributions to the strain energy density ψ are then given by

$$\psi^+(\boldsymbol{u}) = \frac{1}{2}K\langle \mathrm{tr}(\boldsymbol{\varepsilon})\rangle^2 + \mu\boldsymbol{\varepsilon}_\mathrm{D} : \boldsymbol{\varepsilon}_\mathrm{D}, \tag{7.1}$$

$$\psi^-(\boldsymbol{u}) = \frac{1}{2}K\langle -\mathrm{tr}(\boldsymbol{\varepsilon})\rangle^2, \tag{7.2}$$

where $\boldsymbol{\varepsilon}_\mathrm{D}$ is the deviatoric part of the strain tensor $\boldsymbol{\varepsilon}$ and K is the bulk modulus.

To simulate the damage evolution, we use the Pham [120] formulation, which we briefly mention as a reminder. As for the dissipation function, the model is valid for an arbitrary choice of $\alpha(d)$. The present formulation considers a simple relation

$$\alpha(d) = d, \quad c_\alpha = 8/3, \tag{7.3}$$

with the degradation function defined as

$$g(d) = (1-d)^2. \tag{7.4}$$

Unlike common representation of a dissipation function $\alpha(d) = d^2$ suggested by Bourdin et al. [26], which considers damage evolution already at the onset of loading, the adopted linear version allows for postponing the damage initiation beyond this point, and so not affecting the initial transfer of energy from the impactor into the plate.

For the present choice of $\alpha(d)$ the fracture energy G_f can be written in terms of the tensile strength f_t, Young's modulus E, and the length scale parameter l as [152]

$$G_\mathrm{f} = \frac{8}{3}\frac{l f_\mathrm{t}^2}{E}. \tag{7.5}$$

While strictly valid for one-dimensional (1D) setting, Eq. (7.5) is generally adopted also for simulations in higher dimensions. Owing to the presence of length scale parameter l, typically equal to two times the characteristic length of the smallest element in the finite element mesh [102], this relation is also mesh dependent.

TABLE 7.3: Fracture energies G_f of glass for quasi-static bending f_t and initial tensile strength $\boldsymbol{f}_\mathrm{t}^\mathrm{in}$ and given length scale parameter l

l [mm]	E [GPa]	f_t	f_t^in [MPa]	G_f [Jm^{-2}]
4	70	45	-	308.6
4	70	-	145 (SG)	3203.8
4	70	-	250 (5LG)	9523.8
4	70	-	300 (7LG)	13714.3

For a typical edge length of a triangular element of 2 mm employed for the analysis of laminates discussed in Section 7.1, the fracture energy stored in Table 7.3 may considerably exceed a typical value of $G_\mathrm{f} = 8$ Jm^{-2} used for glass. While the value of $f_\mathrm{t} = 45$ MPa corresponds to the characteristic quasi-static strength in tensile bending defined by the European Standard EN 16612 [1], the larger values, e.g., $f_\mathrm{t}^\mathrm{in} = 145$ MPa used particularly in the analysis of a single glass ply, represents the initial value of tensile strength we adopted to postpone the onset of damage in numerical simulations and consequently to arrive at the glass response comparable with experimental observations. Point out that even larger values of the initial tensile strength were considered in [155]. Since at the onset of damage this value almost immediately drops down to the actual strength of 45 MPa, the associated fracture energy enters the analysis only at a very beginning stage of fracture process, see ahead Section 7.3 for further details. Nevertheless, realistic values of G_f would still call for much smaller elements to avoid snap-back at a

material level. On the contrary, this would lead to computationally unfeasible simulations. Thus only the large values around 300 Jm^{-2} to simulate the crack propagation were tested in all present calculations.

The impact of steel impactor with weight m_{imp} is included in the model through Hertz-law. The impactor is characterized by scalar displacement u_{imp}, which is binded to plate by nonlinear contact force

$$F(\boldsymbol{u}, u_{\mathrm{imp}}) = k\langle u_z(\boldsymbol{x}_{\mathrm{imp}}) - u_{\mathrm{imp}}\rangle^{3/2}, \tag{7.6}$$

where $\boldsymbol{x}_{\mathrm{imp}}$ is impact position on body Ω, u_z is out-of-plane component of $\boldsymbol{u} = (u_x, u_y, u_z)$ and k is contact stiffness. This stiffness for spherical impactor hitting the flat plate is defined as

$$k = \frac{4}{3}\frac{\sqrt{R}}{\frac{1-\nu^2}{E} + \frac{1-\nu_{\mathrm{imp}}^2}{E_{\mathrm{imp}}}}, \tag{7.7}$$

where $R =$ is impactor head radius and $E_{\mathrm{imp}}, \nu_{\mathrm{imp}}$ are material parameters of impactor whereas E, ν are material parameters of glass. Although the force is nonlinear the pseudo potential of this force can be still found. This potential

$$\mathcal{P}_{\mathrm{Hertz}} = \frac{2}{5}k\langle u_z(\boldsymbol{x}_{\mathrm{imp}}) - u_{\mathrm{imp}}\rangle^{5/2} \tag{7.8}$$

is added to external work (3.12) and it induces force (7.6) applied to impact point $\boldsymbol{x}_{\mathrm{imp}}$ and negative force (7.6) applied to the impactor. Additionally the kinetic energy must be enhanced by

$$\mathcal{K}_{\mathrm{imp}} = \frac{1}{2}m_{\mathrm{imp}}\dot{u}_{\mathrm{imp}}\dot{u}_{\mathrm{imp}} \tag{7.9}$$

with impactor displacement rate $\dot{u}_{\mathrm{imp}}$. This part of kinetic energy is again approximated by discretized Lagrangian and discrete Euler-Lagrange equation induces following additional member of weak form (3.33), i.e.

$$\delta\mathcal{K}_{\mathrm{imp}} = m_{\mathrm{imp}}\frac{u_{\mathrm{imp},i+1} - 2u_{\mathrm{imp},i} + u_{\mathrm{imp},i-1}}{\Delta t^2}\delta u_{\mathrm{imp}} \tag{7.10}$$

The implementation of such approach is based on common finite element method (FEM), where new additional degree of freedom representing position of rigid impactor appears in formulation.

7.2.1 Viscoelasticity of interface layer

The response of a polymer interlayer is significantly time-dependent. But even in a low velocity impact the response time is in the range of milliseconds, so that the rate dependency can be neglected and an empirical rule can be used to evaluate its current

shear stiffness. In particular, adopting the $t/2$ rule [39] the instantaneous shear modulus of the interlayer $G_{\text{interlayer}}$ is provided by

$$G_{\text{interlayer}}(t_i, T_{\text{act}}) = G(t_i/2, T_{\text{act}}), \tag{7.11}$$

where t_i is the current time and T_{act} is the actual temperature. Function $G(t, T)$ can be approximated by the Generalized Maxwell chain model [35] as presented in Chapter 5, where parameters of function $G(t, T)$ for PVB foil can be found.

TABLE 7.4: Parameters of generalized Maxwell chain model representing PVB foil for reference temperature $T_0 = 20°\text{C}$

τ_p (s)	G_p (kPa)	τ_p (s)	G_p (kPa)
10^{-5}	1,782,124.2	10^{1}	1663.8
10^{-4}	519,208.7	10^{2}	587.2
10^{-3}	546,176.8	10^{3}	258.0
10^{-2}	216,893.2	10^{4}	63.8
10^{-1}	13,618.3	10^{5}	168.4
10^{0}	4988.3	-	-

7.3 Damage of single glass ply

The explicit dynamic model is first validated for a single glass ply focusing on both the state before and after the crack initiation. A nondestructive step allows us to check the ability of the computational model and the Hertz contact to predict the dynamic response of glass, whereas the damage step identified the capability of the phase field model. To this end, both the evolution of contact force and displacements at points recorded experimentally were monitored to obtain information on how the energy is transferred from the impactor into the glass laminate. While the experiment is described in detail in [156], the presented experimental results have not been published yet.

TABLE 7.5: Material parameters of float glass and steel impactor

	Glass	Impactor
Young's modulus E (GPa)	70	210
Poisson ratio ν	0.22	0.3
Density ρ (kg/m^3)	2500	-
Mass m (kg)	-	48.2

With reference to the tested samples a glass plate with dimensions 0.5×0.5 m, recall also Table 7.1, is examined. Because of symmetry, only a quarter of the model with appropriate symmetry boundary conditions is considered. The material parameters of both the glass and impactor needed in numerical simulations are summarized in Table 7.5. As already mentioned in Section 7.1 the radius R of the impactor head is set to 50 mm.

TABLE 7.6: Details on finite element mesh

	Triangle	Quadrilateral	3D Tetrahedron
Mesh size	-	100x100	20x20x4
Characteristic length (mm)	3/(min 2)	3.5	15
Number of degrees of freedom	48626	51006	45388
Element type	Linear	Bilinear	Quadratic
Out-of-plane shear integration	Reduced	Reduced	Full

An example of the finite element mesh made of triangular elements is presented in Figure 7.4. To support the use of these elements in numerical analysis of laminates the application of bilinear quadrilateral plate elements with reduced integration of out-of-plane shear is also tested and compared with a full three-dimensional (3D) calculations exploiting higher order tetrahedral elements. Details of the adopted finite element meshes are listed in Table 7.6.

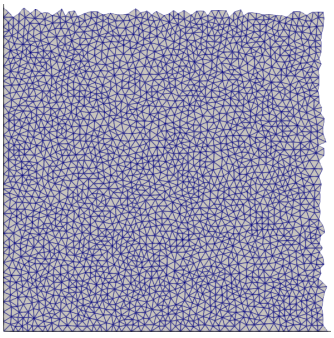

FIGURE 7.4: Example of the finite element mesh consisting of a random grid of 3-node triangular elements

The effect of the element type and the corresponding mesh on the ply response is tested first considering a simple example of a plate weakened by an initial crack. The plate is impacted with the energy of 148 J (impact height of 30 cm). The initial crack is introduced by enforcing the damage $\bar{d}(\boldsymbol{x}_d) = 0.99$ for coordinates $\boldsymbol{x}_d = \{(x, y)|\zeta > |x - 0.125|\}$ to spread over the width of two elements (Figure 7.5 left) for a given value of the shear parameter ξ, recall Eqs. (4.29) - (4.30). We set $l_c = 2h_{\min}$, where $h_{\min}$ is the edge length of the smallest element in the mesh.

The variation of deflection across the crack at the selected time $t = 0.003$ s is plotted in Figure 7.5 on the right hand side. The solid lines represent the case of no damage in shear with $\xi = 0$, thus only the bending part in Eq. (4.30) is affected by damage and the shear strains contribute entirely to ψ^-. While the mesh with the quadrilateral elements provides reasonable response, we see that for the triangular mesh the wave passes across the crack. This can be attributed to spurious shear strain transfer. However, when degrading the the whole out-of-plane shear contribution by setting $\xi = 1$ (the shear contribution now taken entirely by ψ^+ is fully degraded by function $g(d)$) in the analysis with a triangular mesh we arrive at the expected response as shown by the dashed line.

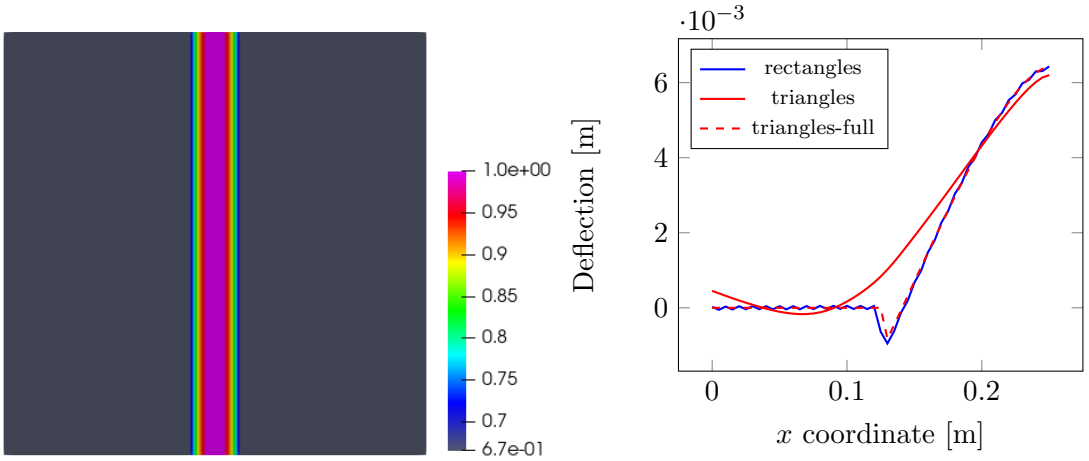

FIGURE 7.5: Initial damage distribution on quarter plate (left) and deflection distribution along x-axis for triangular and quadrilateral elements and for triangular elements with assumed shear damage with ($\xi = 1$) denoted as triangles-full (right)

The next example addresses a non-destructive test allowing us to compare the experimentally measured contact force with numerical predictions up to the impact height of 30 cm. The results for various types of meshes, recall Table 7.6, are presented in Figure 7.6(a) for $h_{\text{imp}} = 10$ cm. As seen, all meshes provide a comparable response matching well the experimental measurements. However, it has been observed that four node quadrilateral elements, albeit using one point integration in shear, experience a zero energy mode manifested by local vibration from element to element. For that reason and given the results in Figure 7.5, the triangular mesh in Figure 7.4 with shear degradation option was used in all subsequent analyses. Its applicability is further promoted by the comparative study displayed in Figure 7.6(b), where a reasonable agreement with experimental results is suggested even for a relatively high impact energy.

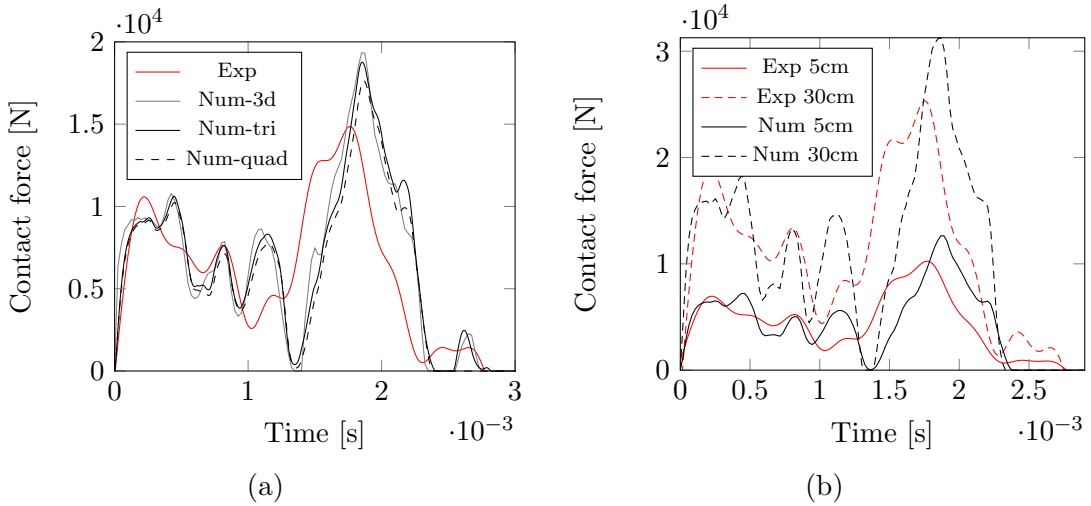

FIGURE 7.6: Comparison of evolution of measured and predicted contact force for nondestructive test: a) influence of finite element type - impact height of 10 cm, b) application of triangular mesh for impact heights of 5 cm and 30 cm

The last experiment is concerned with adjusting the onset of damage. This is because the stress calculated in the contact zone between an impactor and glass exceeds the glass strength f_t earlier than the glass breaks in experiments [61, 125]. This is quite important also with the phase-field analysis. For illustration, we consider a destructive test where the tested sample broke already at the impact height $h_\mathrm{imp} = 20$ cm. The results appear in Figures 7.7 - 7.9.

Figure 7.7(a) indicates that assuming the actual static tensile strength $f_\mathrm{t}^\mathrm{in} = f_\mathrm{t} = 45$ MPa promotes the damage initiation too early in comparison to the experimental results, while delaying the onset of the damage via artificially increasing the tensile strength to $f_\mathrm{t}^\mathrm{in} = 145$ MPa shows a considerable improvement in the prediction of the contact force. Figure 7.8 further suggests that controlling the crack initiation by $f_\mathrm{t}^\mathrm{in} = 45$ MPa does not generate sufficient energy to drive a rapid crack evolution and crack branching as observed experimentally [155, 156].

A remedy is provided by restoring the initial high tensile strength to its physically correct value at the onset of damage [155], i.e., $f_\mathrm{t}^\mathrm{in} = 145 \rightarrow f_\mathrm{t} = 45$ MPa. The former value ensures accumulation of sufficient energy, whereas the latter value allows its rapid dissipation leading to more realistic crack pattern. While seemingly simple, this step still deserves attention, particularly in the framework of the presented phase field model.

Remind that the evolution of damage is driven by fracture energy. However, the relationship between the tensile strength f_t and fracture energy G_f provided by Eq. (3.22) is valid for 1D analysis only. When used with a general 3D analysis such calculated fracture energy may lead to damage initiation for stresses, which do not exceed the prescribed tensile strength. Thus in the present study, the point of switching the analysis from initial state controlled by the initial value of fracture energy to the one associated with the actual tensile strength of $f_\mathrm{t} = 45$ MPa, recall Table 7.3, is determined by reaching the value of the damage parameter $d = 0.9$ in the most stressed element. This can be mathematically represented as

$$G_\mathrm{f} = \begin{cases} G_\mathrm{f}^\mathrm{in}, & \text{if } d(\boldsymbol{x}) < 0.9, \forall \boldsymbol{x}, \\ G_\mathrm{f}|_{f_\mathrm{t}=45\ \mathrm{MPa}} & \text{if } \exists \boldsymbol{x} : d(\boldsymbol{x}) \geq 0.9. \end{cases} \tag{7.12}$$

From that point on the subsequent fracturing process in an arbitrary element continues with the value of G_f associated with $f_\mathrm{t} = 45$ MPa and the mesh dependent length scale parameter l set to $2h_\mathrm{min} = 4$ mm in all simulations involving the triangular mesh.

This approach resulted in the damage pattern seen in Figure 7.9 with the corresponding evolution of the contact force depicted in Figure 7.7(b). Note that the shear reduction parameter ξ was set to a threshold value of 0.95 to avoid through thickness penetration of the impactor. The accumulation of energy by using increased initial tensile strength f_t^in allows for formation of more random crack patterns. With a sufficiently large difference between the actual f_t and initial f_t^in tensile strengths the model promotes cracks in

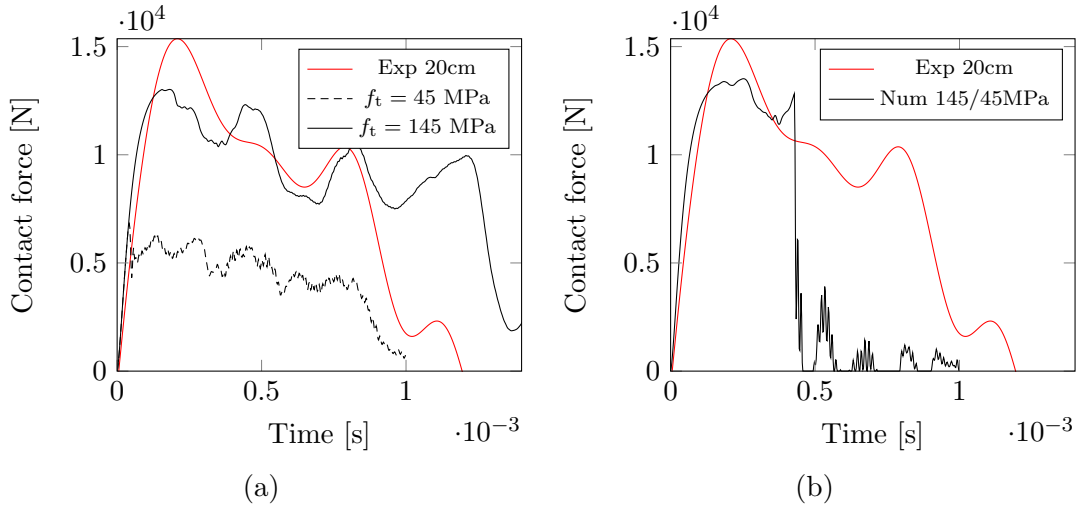

FIGURE 7.7: Comparison of evolution of measured and predicted contact force for destructive test: a) constant tensile strength, b) variable tensile strength

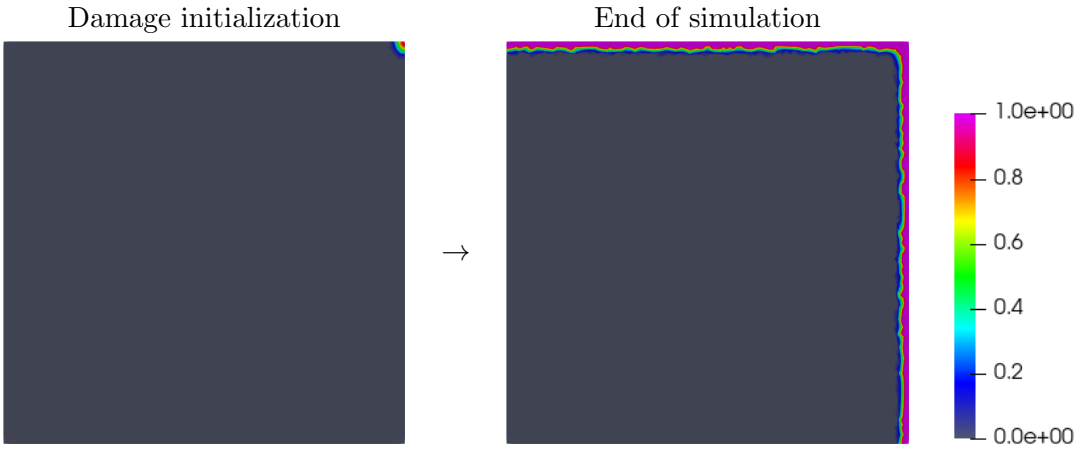

FIGURE 7.8: Damage evolution for single glass ply with static tensile strength

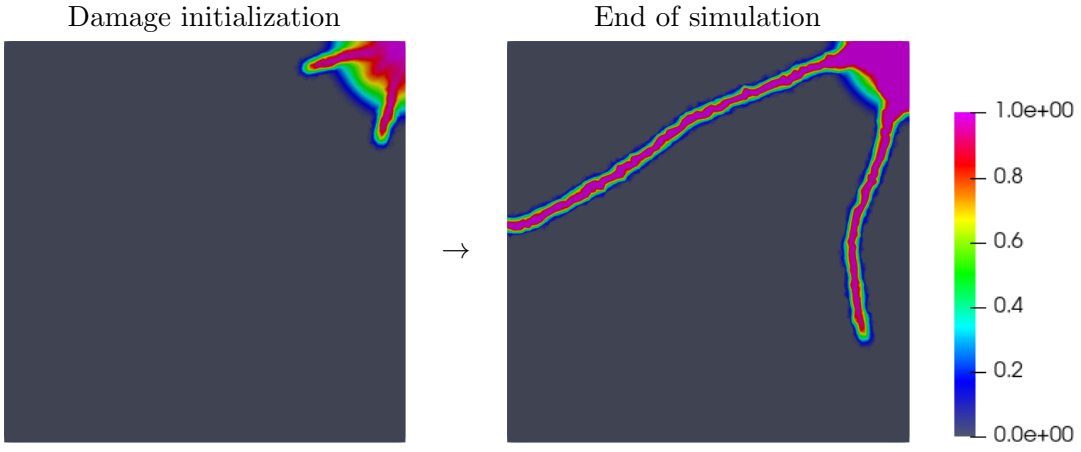

FIGURE 7.9: Damage evolution for single glass ply with adjusted initial tensile strength

multiple directions. On the other hand, we see a notable mismatch in the descending part of the measured and predicted contact force, Figure 7.7(b). This can be attributed to the fact that the impactor gradually penetrates into the already broken fragments. Similar result, derived with the help of LS-DYNA software, has been observed in [156] both in terms of crack pattern and contact force evolution.

7.4 Damage of laminated glass plate

The results presented in the previous section now open the door to the simulation of laminates exploiting the theoretical framework outlined in Section 4.2.

Similar to the experimental program discussed in Section 7.1 we address both types of laminates with their geometrical details provided in Table 7.1. The material properties of the impactor and glass layers are taken from Table 7.5. For the polymer interlayer we set the density $\rho_{\text{int}} = 1100\ \text{kg/m}^3$. The Poisson ratio ν =0.49 is considered to approach a volumetrically incompressible material while avoiding a significant shear locking. Given the room temperature during experiments in the range of 24.9°C to 26.0°C we set T_{act} to 25°C. As suggested in Section 7.2.1 the viscoelastic properties of the interlayer are included only empirically via Eq. (7.11). No other material parameters of the PVB interlayer are needed as damage is expected to occur in the glass layers only.

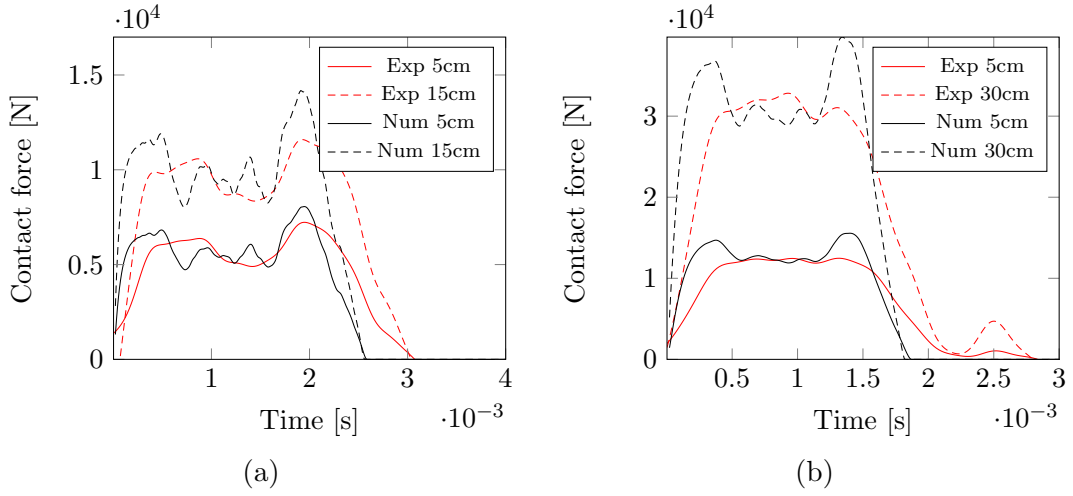

FIGURE 7.10: Comparison of evolution of measured and predicted contact force for nondestructive test: a) 5LG-3 laminate, b) 7LG-2 laminate

To validate implementation of the layered plate theory we begin again with nondestructive tests. For the sake of brevity, attention is limited to 5LG-3 and 7LG-2 samples as these show a similar evolution of gradual damage due to repeating impacts of variable intensity, see Table 7.2. The response of both types of laminates is examined through the distribution of contact force for two impact heights causing no damage. The results plotted in Figure 7.10 indicate a satisfactory agreement between numerical predictions and experimental measurements thus excluding any systematic error potentially linked to

numerical implementation. The observed differences are merely associated with the 8th-pole Butterworth low-pass filter (2× CFC 1000 filter) we used to filter out the frequencies associated with vibrations of the impactor from the measured accelerations [155]. Apart for eliminating the initial data before the largest amplitudes (approximately 0.3–0.4 ms of a signal) and the final part (after 20 ms) with small oscillations affected significantly by the experimental noise, the filter was applied to the entire time domain associated with the experimental measurements. The eliminated data could have affected the initial slope of the experimentally observed contact force so its direct comparison with the numerical predictions might be misleading.

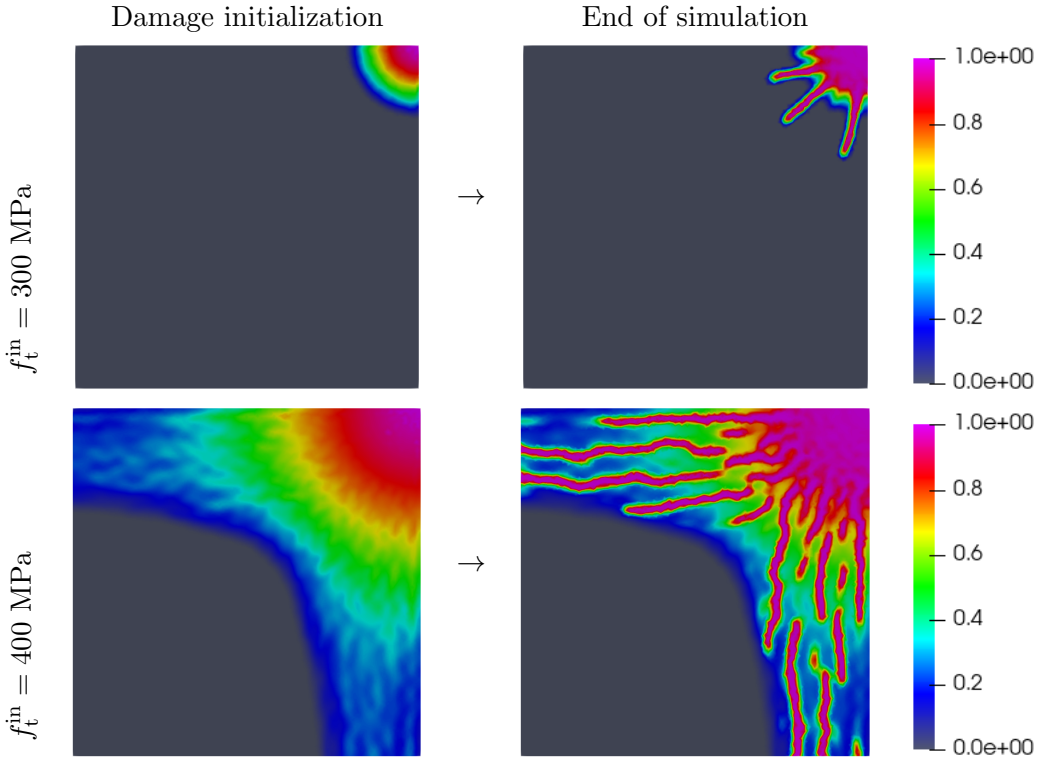

FIGURE 7.11: Damage evolution in back glass layer of 5LG laminate for two values of initial tensile strength f_t^{in}

Moving to damage brings to mind the key role of the initial tensile strength we suggested in the previous section. Its value influences the amount of energy available in the glass to drive the evolution of fractures. This is illustrated in Figure 7.11 assuming two different values of the initial tensile strength f_t^{in}. Similarly to the result presented in Figure 7.9 the strength was reduced to $f_f = 45$ MPa according to Eq. (7.12). The damage patterns at the onset of cracking and at the time when the damage fully localized into isolated cracks are shown for the back glass layer (the furthermost from the impacted one) of a 5LG-laminate loaded by the impact energy of 236 J (impact height of 50 cm). It is evident that the value of the initial tensile strength qualitatively changes the result of the simulation. One may therefore consider this value as another material parameter albeit depending on a given computational model. For $f_t^{in} = 300$ MPa the damage initiated at $t = 0.22$ ms whereas for $f_t^{in} = 400$ MPa it was delayed to $t = 1.2$ ms. While the time to

stabilize the crack growth was in both cases about the same the larger amount of energy dissipated in the latter case resulted in a significantly denser crack pattern. It follows that choosing the value of $f_{\mathrm{t}}^{\mathrm{in}}$ sensitively the model is able to control the branching and development of multiple cracks with no additional ad hoc criteria.

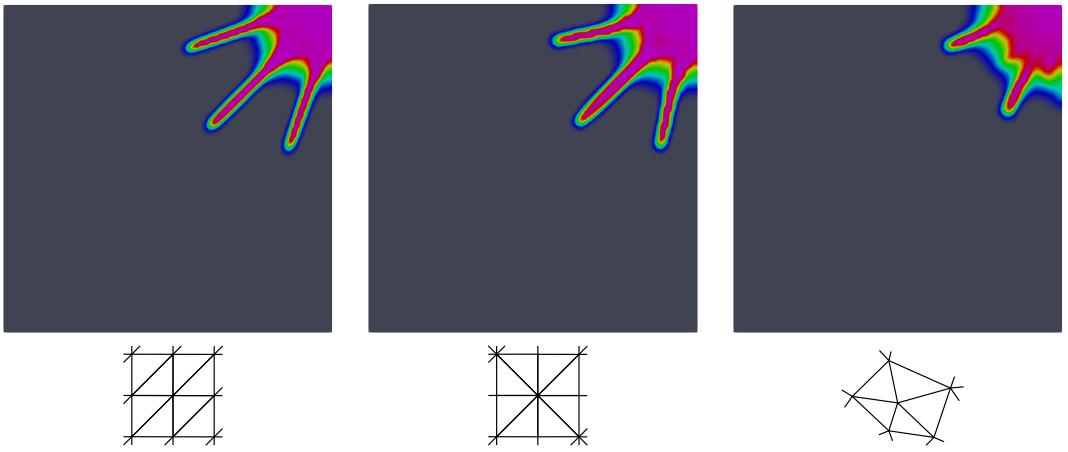

FIGURE 7.12: Damage distribution for three different meshes

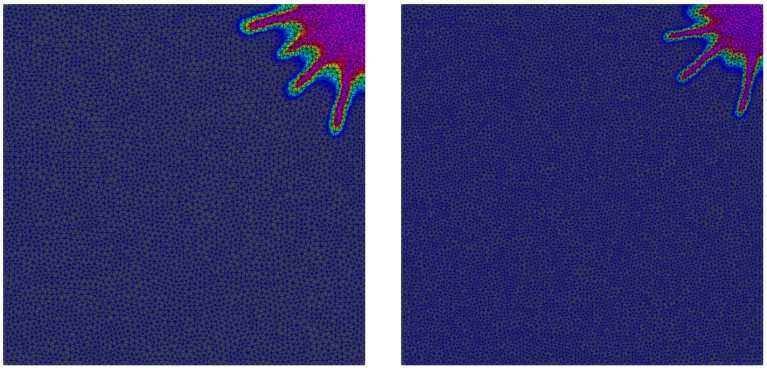

FIGURE 7.13: Impact of mesh density on damage initiation (t^{in}) and subsequent evolution ($t = t^{\mathrm{in}} + 0.02$ ms): coarser mesh left ($t^{\mathrm{in}} = 0.31$ ms), finer mesh right ($t^{\mathrm{in}} = 0.22$ ms)

TABLE 7.7: Time range of damage evolution for different meshes

Name	Mesh	t^{in}	t^{cr}	$\Delta t_{\mathrm{in}}^{\mathrm{cr}}$
C1	100	0.22	0.4048	0.1848
C2	100/2	0.1991	0.2222	0.0231
C3	100/3	0.19635	0.20075	0.0044
C4	100/4	0.19782	0.19971	0.00189
B1	50	0.2024	1.2408	1.0384
B2	75	0.1012	0.3124	0.2112
B3	100	0.099	0.2222	0.1232
B4	100/3	0.05225	0.0649	0.01265

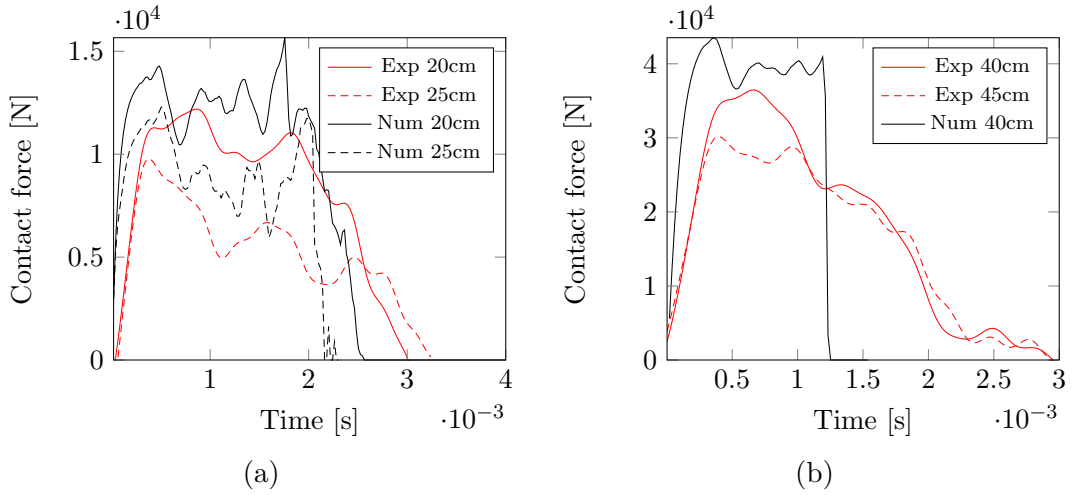

FIGURE 7.14: Comparison of evolution of measured and predicted contact force for destructive test: a) 5LG-3 laminate, b) 7LG-2 laminate

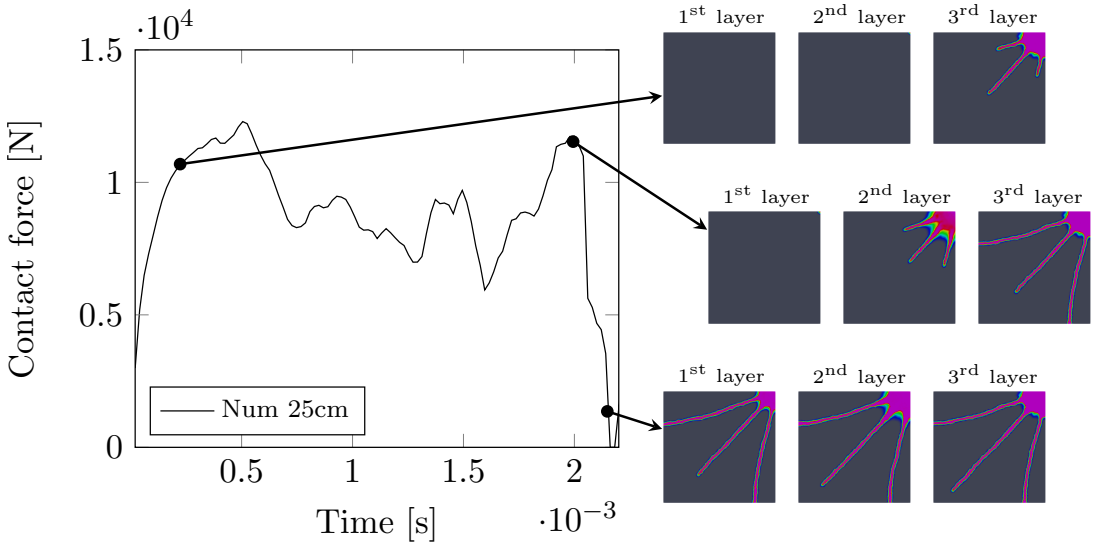

FIGURE 7.15: Evolution of cracks in 5LG laminate due to impact height $h_{\text{imp}} = 25$ cm, the 1st layer is the impacted one

As the solution depends on the length scale parameter l which in turn is estimated from the underlying finite element mesh it appears useful to briefly address this issue. Proceeding with the previously studied 5LG laminate we keep the initial tensile strength $f_{\text{t}}^{\text{in}} = 300$ MPa and assume the impact energy of 236 J (impact height of 50 cm). The first example compares structured and unstructured meshes sketched in Figure 7.12 (bottom figures). Considering a comparable mesh density the length of the process zone is set to $l = 7$ mm for all tested meshes. The damage patterns for the time instant $t = 0.4$ ms are compared in Figure 7.12 (top figures) for two examples of structured meshes and one example of the unstructured mesh, recall Figure 7.4. The evolution of damage along preferential direction associated with the structured meshes is evident.

The second example addresses the effect of mesh refinement considering two mesh densities, a coarser mesh with 9425 elements and the process zone $l = 6$ mm (left) and a finer mesh with 19119 elements and the process zone $l = 4$ mm (right) being essentially the one in Figure 7.4. It has been found that the mesh density influences the onset of damage, i.e., the transition point $f_{\mathrm{t}}^{\mathrm{in}} \to f_{\mathrm{t}}$. The damage initiation is delayed with increasing the element size with the time at the onset of damage $t^{\mathrm{in}} = 0.31$ ms and $t^{\mathrm{in}} = 0.22$ ms for the coarser and finer mesh, respectively. The damage patterns plotted in Figure 7.13 correspond to time $t = t^{\mathrm{in}} + 0.02$ ms. While the onset of damage and partially also the crack pattern differ, the crack growth velocity appears similar for both meshes. A potential reason for decreasing the initiation time t^{in} with increasing the mesh refinement can be attributed to the reduction of the fracture process zone leading to a brittle failure when this parameter approaches zero. This issue is under current investigation.

The above findings are finally exploited in the simulation of gradual damage caused by several consecutive impacts for the selected laminates. The finer element mesh in Figure 7.13, recall also Figure 7.4, was used since it provides a satisfactory agreement between the measured and the predicted contact force. Note that with repeating impacts the new calculation always started from the damage state associated with the previous loading step. We begin with the 5LG-3 sample. To correctly predict the onset of damage for the impact height $h_{\mathrm{imp}} = 20$ cm the initial tensile strength $f_{\mathrm{t}}^{\mathrm{in}} = 250$ MPa was used. The distribution of the contact forces is presented in Figure 7.14(a).

In agreement with the experiment, the back layer fractured first. To force the damage to propagate to another glass layer required to increase the impact height to 25 cm. Similarly to the experiment the layers cracked gradually from the back layer towards the impacted one. Unlike the experiment, however, both remaining layers cracked at this simulation step. The evolution of damage in individual layers is displayed in Figure

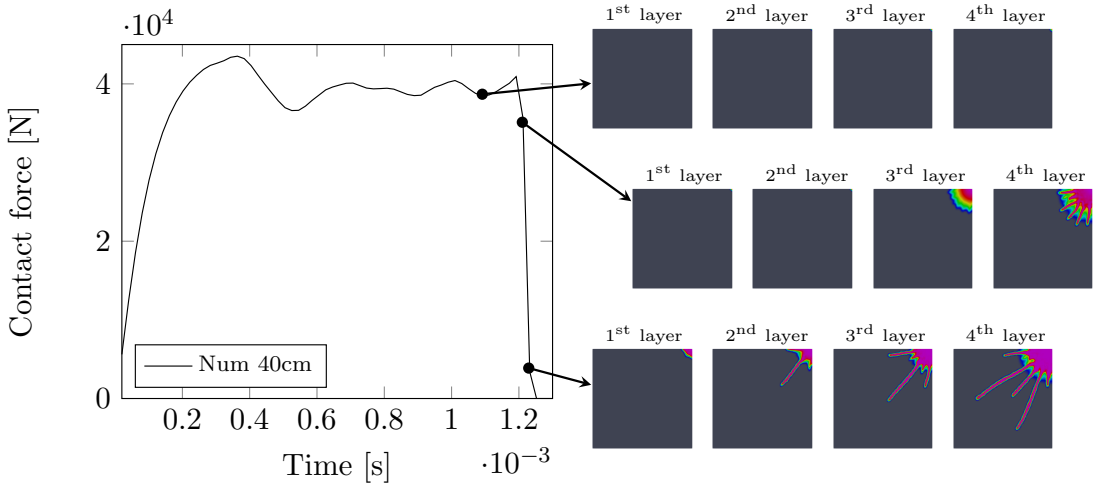

FIGURE 7.16: Evolution of cracks in 7LG laminate due to impact height $h_{\mathrm{imp}} = 40$ cm, the 1st layer is the impacted one

7.15 for the selected time instances. It is worth mentioning that the same value of $f_{\mathrm{t}}^{\mathrm{in}}$ was prescribed to all layers whereas in [155] each layer was assigned a different value of $f_{\mathrm{t}}^{\mathrm{in}}$ to follow the experimentally observed cracking sequence as close as possible. Since this was not the principal objective of this study, primarily focusing on the potential applications of phase-field to model fracture in laminated glass, we did not investigated this topic any further.

Similar conclusions can be drawn from the simulations of the 7LG laminate as only the onset of damage was meant to be captured in agreement with the experiment performed on 7LG-2 sample. To this end, the value of $f_{\mathrm{t}}^{\mathrm{in}} = 300$ MPa was considered. As the same value was again assigned to all layers, it is not surprising, point out a relatively large impact energy, that all layers fractured within this single simulation step. This is also why only one numerically generated contact force is presented in Figure 7.14(b). The corresponding evolution of cracks at specific simulation times is available in Figure 7.16.

To arrive at better agreement with experiment, both in terms of the contact force variation and fracture sequence, would require more gentle tuning of the initial tensile strength on the one hand and assigning a different value of this parameter to individual layers on the other hand. The latter option would cause the contact force to decay more gradually [155]. But as already mentioned, this goes beyond the present scope.

7.5 Future extension

The results presented above are the result of the application of the phase field model for simulating the initiation and development of damage in laminated glass under low-velocity impact. The results were published in the author's article [130]. What follows is a direct continuation of the investigation of such models and presented are unpublished results.

To test the model further, we can focus on the effect of mesh size around the impact point. Consistent results are not obtained for the model above. Shall changes do not have a significant effect on crack development, but a very fine mesh already concentrates the stress on a very small area and the model starts to behave differently. It is therefore necessary to distribute the loading force, especially for the fine meshes. The Hertz's law gives a direct relation for impacted area radius a according to the indentation d as $a = \sqrt{Rd}$, which induces unsustainably fine mesh for our needs and thus an inconsistent relation was used.

FIGURE 7.17

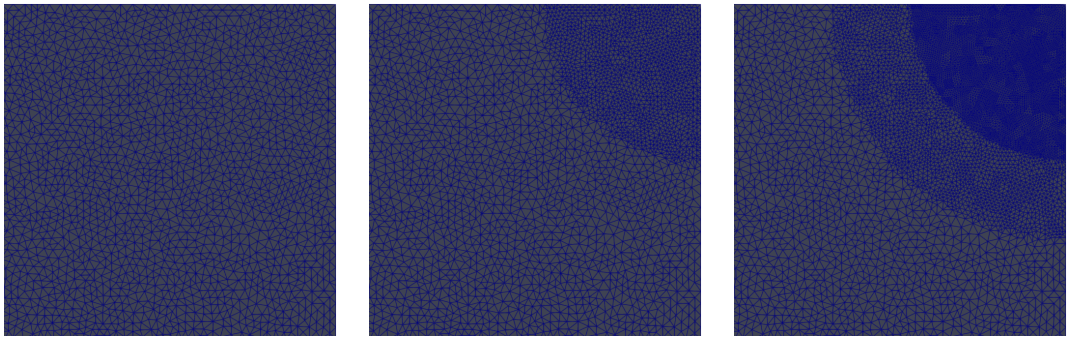

FIGURE 7.18

7.6 Conclusion

The paper described the application of the phase-field model to the modeling of gradual evolution of damage in laminated glass structures subjected to a low-velocity impact of increasing intensity. To reduce the computational complexity, the theory was introduced in the framework of the layered Mindlin plate theory with piecewise constant distribution of out-of-plane shear stresses. Further simplifications included the transfer of the kinetic energy from the impactor into the glass layer through the linear Hertz law (7.8), calculation of the instantaneous shear modulus via the $t/2$ rule (7.11), and the use of $f_{\mathrm{t}} \rightarrow G_f$ relation (7.5) in 3D simulations, albeit strictly valid for 1D setting only. Such model allowed us to perform all calculations very efficiently with the help of a fully explicit dynamic solver. The principal observations are:

- Introducing a properly selected initial tensile strength to accommodate sufficient energy prior to the onset of cracking appears crucial to correctly track the evolution of damage thus supporting our observations presented in [155]. This was demonstrated by comparing the distribution of the contact force and gradually evolving the crack patterns with the experimental results. The phase field model then proved its ability to predict the expected sequence of fracture of individual glass layers as well as crack branching within these layers. Owing to a random behavior of glass laminates, partially associated with random nature of the initial

defects in the glass, this parameter, hardly deterministic, reduces the predictive capability of any damage model applied to the modeling of impact resistance of such structures. To promote the current approach in predictive or parametric studies, the simulations should be potentially presented in the stochastic framework once data from a sufficiently broad experimental program are available.

- Given the presence of the length scale parameter to provide regularization, these models are mesh dependent both in terms of the element size and mesh orientation. But because the leading equation (4.38) follows from the minimization of total energy, the convergence of the solution can be expected upon a sufficient mesh refinement. In this regard, an unstructured mesh made of 3-node triangular elements with degraded contribution of out-of-plane shear was found optimal.

- Unlike the predicted density of cracks, the crack orientations and paths, turning towards the plate edges, is fully compatible with experimental observations. To arrive at improved prediction of the crack pattern might require more accurate rule for the glass-impactor contact. The linear model based on the Hertz law is too much localized and cannot accurately describe the contact between the glass fragments and the impactor head and thus to ensure proper transition of the kinetic energy into the plate.

Chapter 8

Summary and conclusions

The mathematical description of fragile beams and plates exposed to bending presents a mathematical singularity, making it difficult to achieve efficient implementation and description. However, modern phase-field damage theory provides an opportunity to simulate the initiation and progression of cracks in brittle materials while maintaining variational consistency. Consequently, this study explores the feasibility of applying such a model to laminated glass.

This research investigates the advantages and limitations of employing phase-field damage models in simulating structural elements, specifically focusing on their application to laminated glass. The main observations are as follows:

- The phase-field damage model is based on an energy approach, which ensures an objective method capable of simulating crack initiation and development without relying on additional ad-hoc criteria. Crack propagation and branching in dynamic regimes are directly determined through minimization. Despite its objectivity, experimental results do not always align with the predictions of this approach. In experiments, the cracks tend to branch even under quasi-static loading, which is rarely observed in the models. The phase-field model favors a solution with one-point localization.
- By utilizing the principles of damage mechanics and leveraging the capabilities of the modern finite element package FEniCS, the phase-field approach enables effective fracture simulations even on personal computers, eliminating the need for extensive calculations on supercomputers. The method does not introduce new implementation techniques; it simply harnesses the ingenuity of its formulation, making it widely applicable. This work also emphasizes the benefits of such an approach.

In addition, we present the contributions of this study to the field of mechanics, along with an outline of potential future research.

- While exact agreement with experimental results has not always been achieved, it can still be concluded that the phase-field model serves as a highly effective tool for qualitative failure analysis. Despite certain quantitative limitations, the model accurately predicts the initiation of cracks at specific points and their subsequent development in expected directions. This work demonstrates the immense potential of the phase-field model in practical engineering applications.

- Furthermore, the research also explores the application of the phase-field damage model to spatialy reduced models, such as beams and plates. These models offer substantial computational efficiency while still providing significant predictive value, as demonstrated in this study.

Appendix A

Fragile beam model

The spatially reduced beam model with implemented phase-field damage approach is tested in this Appendix. The validity of numerical results for some basic cases is verified and also the connectivity between longitudinal deflection and cross-section rotation is validated.

A.1 Damage localization

The first test is based on simply supported beam loaded by prescribed rotations at the ends, which generates constant bending moment along the beam. The loading scheme is depicted in Figure A.1.

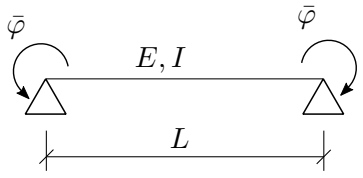

FIGURE A.1: Loading scheme for constant bending moment, where $\bar{\varphi}$ is prescribed cross-section rotation.

This is sufficient benchmark which play the same role for beam validation as longitudinally stretched 1D beam for testing behavior in tension-compression. Moreover the damage evolution can be derived analytically under some simplified assumptions. Consider for a moment that the damage at a given point is controlled by the driving force at that point, which corresponds to the entire accumulated energy, not only its active part. There is no decomposition into a tensile and a compress part. If we also consider Pham version of the phase-field model ($\alpha(d) = d, c_\alpha = 3/8$), we get the following identity for damage depending on prescribed rotation $\bar{\varphi}$

$$d(\bar{\varphi}) = 1 - \frac{3bhG_{\mathrm{f}}L^2}{8EIl_{\mathrm{c}}\bar{\varphi}} \tag{A.1}$$

Material parameters of this task with similar values as for laminated glass follows the physically reasonable assignment, see Table A.1. The length of the process zone l_c and

Parameter	Value
E	70 GPa
L	1.1 m
b	0.36 m
h	0.02 m
f_t	45 MPa

TABLE A.1: Parameters for beam benchmark.

numerical parameters (number of unknowns, time step etc.) are not fixed as well as the fracture toughness which is calculated as

$$G_f = \frac{8}{3}\frac{f_t^2 l_c}{E}, \tag{A.2}$$

therefore the ratio between G_f and l_c remains constant if the length l_c is changed. It immediately follows that qualitatively the development of damage remains the same. It can be immediately seen if (A.2) is substituted into (A.1). But the actual behavior is slightly different. This can be seen in the graphs in Figure A.2, where developments of total reaction and maximum damage in the beam are shown. It can be observed

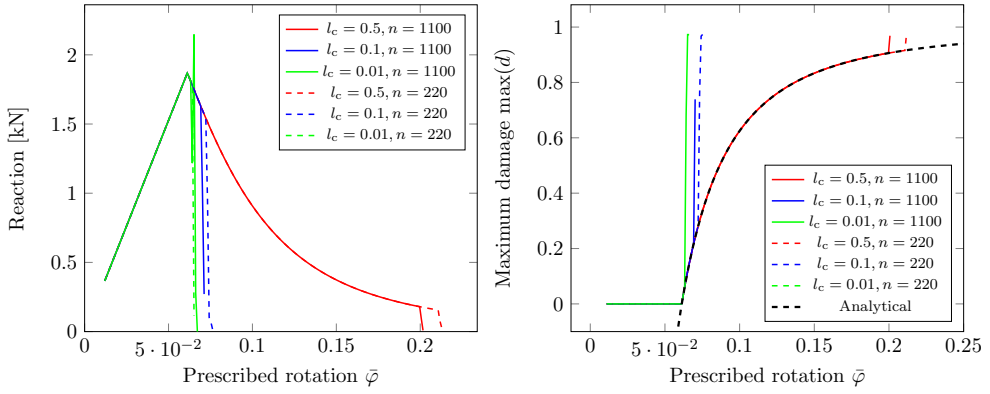

FIGURE A.2: Development of total reaction force (left) and maximum value of damage (right) with respect to the prescribed rotation $\bar{\varphi}$ for time step $\Delta t = 0.001$ s.

that the development of damage in the beam follows exactly the analytical relationship, but at some point instability occurs and the damage localizes. It can be seen from the results that the change in length scale parameter l_c has a great influence on this fact. By reducing the parameter l_c, we do not qualitatively change the theoretical development of damage, but we increase the susceptibility to localization and thus increase fragility.

Another observed phenomenon was the unstable response of the beam with $l_c = 0.01$ m, when the reaction force value oscillated around the time of crack initiation. Most likely, it was a phenomenon related to a excessively large time step. When the step was decreased, the response stabilized. This is shown in Figure A.3.

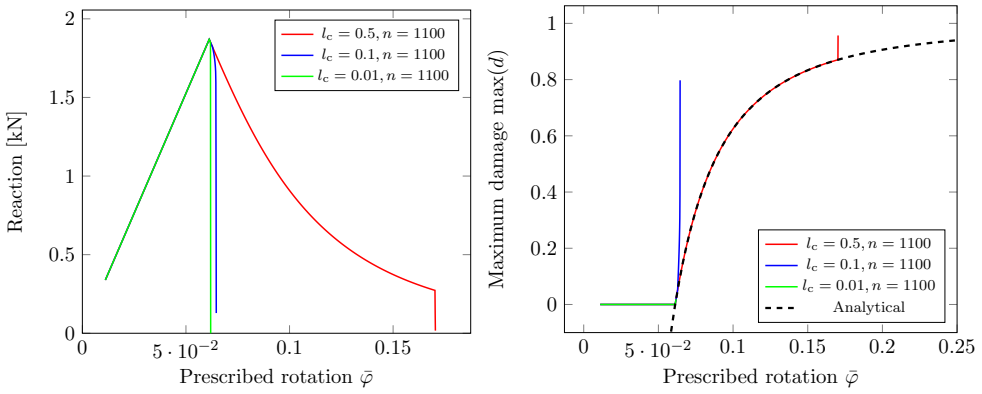

FIGURE A.3: Development of total reaction force (left) and maximum value of damage (right) with respect to the prescribed rotation $\bar{\varphi}$ for time step $\Delta t = 0.0001$ s.

A.2 Interpenetration

Numerical integration across thickness brings an advantage in the form of correct calculation of cross-sectional characteristics even after shifting the neutral axis. The integrals $\int_0^L \mathrm{d}x$, $\int_0^L z\,\mathrm{d}x$ and $\int_0^L z^2\,\mathrm{d}x$ are equal to area A, static moment $S = 0$ and moment of inertia I, but it is true for precracked stage only. Numerical integration correctly (within the numerical error) evaluates these characteristics also in the post-breakage state, thus ties the kinematic variables u and w together. Correct behavior of numerical model can be benchmarked by simple one-layer test with geometrical and numerical parameters given in Section 6.1.

To validate our numerical results, the analytical solution is derived. The analytical solution follows directly from elementary theory of thin beams and corresponding relationship between prescribed deflection $\bar{w}$ and maximum surface stress $\sigma_{\max}$ is

$$\overline{w} = \frac{l^2}{3Eh}\left(3\left(\frac{a}{l}\right) - 4\left(\frac{a}{l}\right)^2\right)\sigma_{\max}, \tag{A.3}$$

where $E = 70$ GPa, $h = 20$ mm, $l = 1,000$ mm, and $a = 400$ mm stands for the location of the loading cylinders relative to supports, recall Figure 6.2.

When the layer is broken, two parts of the beam behave as rigid bodies with zero deformation. Without the binding of kinematic variable the interpenetration of cross sections is allowed, see left part of Figure A.4, on which right part shows correct behavior. Whether the model behave correctly can be verifiied by evaluating of longitudinal displacement in middle of beam u_{middle} with respect to transverse deflection in middle w_{middle}:

$$u_{\text{middle}} = \frac{w_{\text{middle}} h}{l - 100}, \tag{A.4}$$

where $h = 0.02$ mm is beam thickness. The relationship is derived directly from the geometry of rigid body deformations.

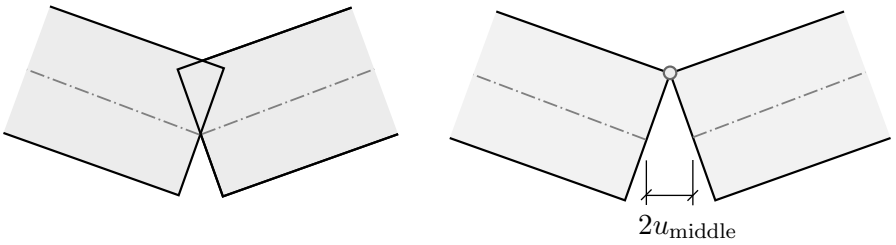

FIGURE A.4: Impenetrability of cross-sections

In this benchmark we set glass strength to the mean value $f_{\text{t}} = 45$ MPa, therefore the equation (A.3) induces the need to prescribe deflection $\bar{w} = 0.006$ m. Using equation (A.4) the predicted longitudinal movement is $u_{\text{middle}} = 0.00015$ m which is in accordance with numerical result. We obtained the values of $\overline{w}_{\text{f}}^{\text{FE}} \doteq 6.006$ mm and $2u_{\text{middle}}^{\text{FE}} \doteq 0.30031$ mm. Among others, these results confirm the correct implementation of the cross-section impenetrability conditions, without which $u^{\text{FE}} = 0$ mm.

Bibliography

[1] CEN EN572-1: 2004 Glass in building-Basic soda lime silicate glass products-Part 1. Technical report, Deutsches Institut für Bautechnik, Berlin, Germany, 2004.

[2] DIN 18008-1:2010-12 Glass in Building - Design and construction rules - Part 1: Terms and general bases. Technical report, German Institute for Standardisation, Berlin, Germany, 2010.

[3] M. L. Aenlle and F. Pelayo. Frequency Response of Laminated Glass Elements : Analytical Modeling and Effective Thickness. *ASME. Appl. Mech. Rev.*, 65(2):1–13, 2013.

[4] M. L. Aenlle and F. Pelayo. Dynamic effective thickness in laminated-glass beams and plates. *Composites Part B: Engineering*, 67:332–347, 2014.

[5] R. Alessi and F. Freddi. Phase-field modelling of failure in hybrid laminates. *Composite Structures*, 181:9–25, 2017.

[6] M. S. Alnæs, J. Blechta, J. Hake, A. Johansson, B. Kehlet, A. Logg, C. Richardson, J. Ring, M. E. Rognes, and G. N. Wells. The FEniCS Project Version 1.5. *Archive of Numerical Software*, 3(100), 2015.

[7] C. Alter, S. Kolling, and J. Schneider. An enhanced non–local failure criterion for laminated glass under low velocity impact. *International Journal of Impact Engineering*, 109:342–353, 2017.

[8] M. Ambati, T. Gerasimov, and L. De Lorenzis. A review on phase-field models of brittle fracture and a new fast hybrid formulation. *Computational Mechanics*, 55(2):383–405, 2014.

[9] L. Ambrosio and V. M. Tortorelli. Approximation of functional depending on jumps by elliptic functional via Γ-convergence. *Communications on Pure and Applied Mathematics*, 43(8):999–1036, 1990.

[10] F. Amiri, D. Millan, Y. Shen, T. Rabczuk, and M. Arroyo. Phase-field modeling of fracture in linear thin shells. *Theoretical and Applied Fracture Mechanics*, 69:102–109, 2014.

[11] H. Amor, J. J. Marigo, and C. Maurini. Regularized formulation of the variational brittle fracture with unilateral contact: numerical experiments. *Journal of the Mechanics and Physics of Solids*, 57(8):1209–1229, 2009.

[12] L. Andreozzi, S. B. Bati, M. Fagone, G. Ranocchiai, and F. Zulli. Dynamic torsion tests to characterize the thermo-viscoelastic properties of polymeric interlayers for laminated glass. *Construction and Building Materials*, 65:1–13, 2014.

[13] I. S. Aranson, V. A. Kalatsky, and V. M. Vinokur. Continuum field description of crack propagation. *Physical Review Letters*, 85(1):118–121, 2000.

[14] M Audy. *Localization of inelastic deformation in problems freeof initial stress concentrators*. PhD thesis, Czech Technical University in Prague, Faculty of Civil Engineering, Prague, 2003.

[15] Daniele Baraldi. A simple mixed finite element model for laminated glass beams. *Composite Structures*, 194:611–623, 2018.

[16] G. I. Barenblatt. The Mathematical Theory of Equilibrium Cracks in Brittle Fracture. *Advances in Applied Mechanics*, 1962.

[17] Z. P. Bažant and M. Jirásek. *Creep and hygrothermal effects in concrete structures*. Springer, 2018.

[18] T. Belytschko, Y. Krongauz, D. Organ, M. Fleming, and P. Krysl. Meshless methods: An overview and recent developments. *Computer Methods in Applied Mechanics and Engineering*, 139(1-4):3–47, 1996.

[19] L. Biolzi, S. Cattaneo, M. Orlando, L. R. Piscitelli, and P. Spinelli. Post-failure behavior of laminated glass beams using different interlayers. *Composite Structures*, 202:578–589, 2018.

[20] J. Bleyer, C. Roux-Langlois, and J. F. Molinari. Dynamic crack propagation with a variational phase-field model: limiting speed, crack branching and velocity-toughening mechanisms. *International Journal of Fracture*, 204(1):79–100, 2017.

[21] A. Bonati, G. Pisano, and G. Royer Carfagni. Redundancy and robustness of brittle laminated plates. Overlooked aspects in structural glass. *Composite Structures*, 227(2):111288, 2019.

[22] M. J. Borden. *Isogeometric analysis of phase-field models for dynamic brittle and ductile fracture*. PhD thesis, 2012.

[23] M. J. Borden, T. J. R. Hughes, C. M. Landis, A. Anvari, and I. J. Lee. A phase-field formulation for fracture in ductile materials: Finite deformation balance law derivation, plastic degradation, and stress triaxiality effects. *Computer Methods in Applied Mechanics and Engineering*, 312:130–166, 2016.

[24] P. O. Bouchard, F. Bay, and Y. Chastel. Numerical modelling of crack propagation: Automatic remeshing and comparison of different criteria. *Computer Methods in Applied Mechanics and Engineering*, 192(35-36):3887–3908, 2003.

[25] B. Bourdin. *Une méthode variationelle en mécanique de la rupture, théorie et applications numériques*. PhD thesis, 1998.

[26] B. Bourdin, G. A. Francfort, and J. J. Marigo. Numerical experiments in revisited brittle fracture. *Journal of the Mechanics and Physics of Solids*, 48(4):797–826, 2000.

[27] B. Bourdin, G. A. Francfort, and J. J. Marigo. The variational approach to fracture. *Journal of elasticity*, 91:5–148, 2008.

[28] B. Bourdin, C. J. Larsen, and C. L. Richardson. A time-discrete model for dynamic fracture based on crack regularization. *Boll. Un. Mat. Ital. B*, 168(8):105–123, 2011.

[29] M Brocca. *Analysis of cracking localization and crack growth based on thermomechanical theory of localization*. PhD thesis, University of Tokyo, Tokyo, 1997.

[30] P. Carrara, M. Ambati, R. Alessi, and L. De Lorenzis. A novel framework to model the fatigue behavior of brittle materials based on a variational phase-field approach. (11), 2018.

[31] S. Chen, M. Zang, D. Wang, S. Yoshimura, and T. Yamada. Numerical analysis of impact failure of automotive laminated glass: A review. *Composites Part B: Engineering*, 122:47–60, 2017.

[32] Shunhua Chen, Mengyan Zang, Di Wang, Shinobu Yoshimura, and Tomonori Yamada. Numerical analysis of impact failure of automotive laminated glass: A review. *Composites Part B: Engineering*, 122:47–60, 2017.

[33] H. Chih Chen, E. Bouchbinder, and A. Karma. Instability in dynamic fracture and the failure of the classical theory of cracks. *Nature Physics*, 13(12):1186–1190, 2017.

[34] I. H. Choi. Contact force history analysis of composite sandwich plates subjected to low-velocity impact. *Composite Structures*, 75(1-4):582–586, 9 2006.

[35] Richard Christensen. *Theory of viscoelasticity: an introduction*. Academic press, 1982.

[36] P. Del Linz, X. Liang, P. A. Hooper, L. Z. Wang, and J. P. Dear. An analytical solution for pre-crack behaviour of laminated glass under blast loading. *Composite Structures*, 144(5):156–164, 2016.

[37] R. Desmorat and F. Gatuingt. Introduction of an internal time in nonlocal integral theories. *Computational Modelling of Concrete Structures*, (3):121–128, 2010.

[38] D. S. Dugdale. Yielding of steel sheets containing slits. *Journal of the Mechanics and Physics of Solids*, 1960.

[39] A V Duser, A Jagota, and S J Bennison. Analysis of glass/polyvinyl butyral laminates subjected to uniform pressure. *Journal of Engineering Mechanics*, 125(4):435–442, 1999.

[40] L. Euler. *Institutiones Calculi Integralis*, volume 1. 1792.

[41] M. Fassin, R. Eggersmann, S. Wulfinghoff, and S. Reese. Gradient-extended anisotropic brittle damage modeling using a second order damage tensor – Theory, implementation and numerical examples. *International Journal of Solids and Structures*, 167:93–126, 2019.

[42] J. D. Ferry. *Viscoelastic Properties of Polymers*. John Wiley and Sons, 1980.

[43] A. G. Fischer and J. J. Marigo. Gradient damage models applied to dynamic fragmentation of brittle materials. *International Journal of Fracture*, 2019.

[44] P. Foraboschi. Analytical model for laminated-glass plate. *Composites Part B: Engineering*, 43(5):2094–2106, 2012.

[45] G. A. Francfort and J. J. Marigo. Revisiting brittle fracture as an energy minimization problem. *Journal of the Mechanics and Physics of Solids*, 46(8):1319–1342, 1998.

[46] F. Freddi and G. Royer-Carfagni. Regularized variational theories of fracture: A unified approach. *Journal of the Mechanics and Physics of Solids*, 58(8):1154–1174, 2010.

[47] L. Galuppi and G. Royer-Carfagni. Effective thickness of laminated glass beams: New expression via a variational approach. *Engineering Structures*, 38:53–67, 2012.

[48] L. Galuppi and G. Royer-Carfagni. Laminated beams with viscoelastic interlayer. *International Journal of Solids and Structures*, 49(18):2637–2645, 2012.

[49] L. Galuppi and G. Royer-Carfagni. The effective thickness of laminated glass plates. *Journal of Mechanics of Materials and Structures*, 7(4):375–400, 2012.

[50] L. Galuppi and G. Royer-Carfagni. The design of laminated glass under time-dependent loading. *International Journal of Mechanical Sciences*, 68:67–75, 2013.

[51] L. Galuppi and G. Royer-carfagni. Buckling of three-layered composite beams with viscoelastic interaction. *Composite Structures*, 107:512–521, 2014.

[52] L. Galuppi and G. Royer-carfagni. Localized contacts, stress concentrations and transient states in bent-lamination with viscoelastic adhesion. An analytical study. *International Journal of Mechanical Sciences*, 103:275–287, 2015.

[53] L. Galuppi and G. Royer-Carfagni. A homogenized model for the post-breakage tensile behavior of laminated glass. *Composite Structures*, 154:600–615, 2016.

[54] L. Galuppi and G. Royer-Carfagni. The post-breakage response of laminated heat-treated glass under in plane and out of plane loading. *Composites Part B: Engineering*, 147:227–239, 2018.

[55] Laura Galuppi and Gianni Royer-Carfagni. Enhanced effective thickness of multi-layered laminated glass. *Composites Part B: Engineering*, 64:202–213, 2014.

[56] M. G. D. Geers, R. De Borst, W. A.M. Brekelmans, and R. H.J. Peerlings. Strain-based transient-gradient damage model for failure analyses. *Computer Methods in Applied Mechanics and Engineering*, 160(1-2):133–153, 1998.

[57] T. Gerasimov and L. De Lorenzis. A line search assisted monolithic approach for phase-field computing of brittle fracture. *Computer Methods in Applied Mechanics and Engineering*, 312:276–303, 12 2016.

[58] T. Gerasimov and L. De Lorenzis. On penalization in variational phase-field models of brittle fracture. *Computer Methods in Applied Mechanics and Engineering*, 354:990–1026, 11 2019.

[59] R. Giovanna, F. Zulli, L. Andreozzi, and M. Fagone. Test Methods for the Determination of Interlayer Properties in Laminated Glass. *Journal of Materials in Civil Engineering*, 29(4), 2016.

[60] A. A. Griffith. The Phenomena of Rupture and Flow in Solids. *Philosophical Transactions of the Royal Society A: Mathematical, Physical and Engineering Sciences*, 221(582-593):163–198, 1921.

[61] Petr Hála, Alena Zemanová, Jan Zeman, and Michal Šejnoha. Numerical Study on Failure of Laminated Glass Subjected to Low-Velocity Impact. *Glass Structures & Engineering*, 2022.

[62] T Hána, M Eliášová, and Z Sokol. For point bending tests of double laminated glass panels. In *Proc. 24th International Conference Engineering Mechanics 2018*, volume 24, pages 285–288, 2018.

[63] T. Hána, T. Janda, J. Schmidt, A. Zemanová, M. Šejnoha, M. Eliášová, and M. Vokáč. Experimental and Numerical Study of Viscoelastic Properties of Polymeric Interlayers Used for Laminated Glass : Determination of Material Parameters. *Materials*, 12(14), 2019.

[64] T. Hána, T. Janda, J. Schmidt, A. Zemanová, M. Šejnoha, M. Eliášová, and M. Vokáč. Experimental and numerical study of viscoelastic properties of polymeric interlayers used for laminated glass: Determination of material parameters. *Materials*, 12(14), 2019.

[65] T. Hatada, T. Kobori, M. Ishida, and N. Niwa. Dynamic analysis of structures with Maxwell model. *Earthquake engineering & structural dynamics*, 29(2):159–176, 2000.

[66] Q. C. He and Q. Shao. Closed-Form Coordinate-Free Decompositions of the Two-Dimensional Strain and Stress for Modeling Tension-Compression Dissymmetry. *Journal of Applied Mechanics, Transactions ASME*, 86(3):1–6, 2019.

[67] H. Hertz. Über die Berührung fester elastischer Körper. *Journal für die reine und angewandte Mathematik*, 92:156–171, 1881.

[68] Hirshikesh, S. Natajaran, and R. K. Annabattula. Modeling crack propagation in variable stiffness composite laminates using the phase field method. *Composite Structures*, 209(10):424–433, 2019.

[69] Hirshikesh, S. Natarajan, and R. K. Annabattula. A FEniCS implementation of the phase field method for quasi-static brittle fracture. *Frontiers of Structural and Civil Engineering*, pages 1–17, 6 2018.

[70] M. Hofacker and C. Miehe. Continuum phase field modeling of dynamic fracture: variational principles and staggered FE implementation. *International Journal of Fracture*, 178(1-2):113–129, 2012.

[71] M. Hofacker and C. Miehe. A phase field model of dynamic fracture: Robust field updates for the analysis of complex crack patterns. *International Journal for Numerical Methods in Engineering*, 93(3):276–301, 2013.

[72] G W Hunt and G Baker. Principles of localization in the fracture of quasi-brittle structures. *Journal of the Mechanics and Physics of Solids*, 43(7):1127–1150, 1995.

[73] Jaroslav Schmidt. PhD thesis Gitlab repository. `https://gitlab.com/js_workdir`, 2022.

[74] J. Jaśkowiec, P. Pluciński, and J. Pamin. Thermo-mechanical XFEM-type modeling of laminated structure with thin inner layer. *Engineering Structures*, 100:511–521, 2015.

[75] M. Jirásek. Nonlocal damage mechanics. *Revue européenne de génie civil*, 11(7-8):993–1021, 2007.

[76] M. Jirásek. Regularized continuum damage formulations acting as localization limiters. *Proceedings of the conference on Computational Modelling of Concrete*, (1984):25–42, 2018.

[77] M. Jirásek and J. Zeman. Localization study of a regularized variational damage model. *International Journal of Solids and Structures*, 69-70(9):131–151, 9 2015.

[78] K. L. Johnson. *Contact mechanics*. Cambridge University Press, 1985.

[79] L. M. Kachanov. *Introduction to continuum damage mechanics*. 1987.

[80] L. M. Kachanov. Rupture time under creep conditions. *International Journal of Fracture*, 97(1-4), 1999.

[81] Nathan D Kaiser, Richard A Behr, Joseph E Minor, Lokeswarappa R Dharani, Fangsheng Ji, and Paul A Kremer. Impact resistance of laminated glass using "sacrificial ply" design concept. *Journal of Architectural Engineering*, 6(1):24–34, 2000.

[82] C. Kane, J. E. Marsden, M. Ortiz, and M. West. Variational integrators and the Newmark algorithm for conservative and dissipative mechanical systems. *International Journal for Numerical Methods in Engineering*, 49(10):1295–1325, 2000.

[83] A. Karma, D. A. Kessler, and H. Levine. Phase-Field Model of Mode III Dynamic Fracture. *Physical Review Letters*, 87(4):045501, 2001.

[84] J. Kiendl, M. Ambati, L. De Lorenzis, H. Gomez, and A. Reali. Phase-field description of brittle fracture in plates and shells. *Computer Methods in Applied Mechanics and Engineering*, 312:374–394, 2016.

[85] G Kikis, M Ambati, Laura De Lorenzis, and S Klinkel. Phase-field model of brittle fracture in reissner–mindlin plates and shells. *Computer Methods in Applied Mechanics and Engineering*, 373:113490, 2021.

[86] J. Kim, G. F. Dargush, and Y. K. Ju. Extended framework of Hamilton's principle for continuum dynamics. *International Journal of Solids and Structures*, 50(20-21):3418–3429, 2013.

[87] S. Krenk. Energy conservation in Newmark based time integration algorithms. *Computer Methods in Applied Mechanics and Engineering*, 195(44-47):6110–6124, 9 2006.

[88] C. Kuhn, A. Schlüter, and R. Müller. On degradation functions in phase field fracture models. *Computational Materials Science*, 108:374–384, 2015.

[89] W. Lai, J. Gao, Y. Li, M. Arroyo, and Y. Shen. Phase field modeling of brittle fracture in an Euler–Bernoulli beam accounting for transverse part-through cracks. *Computer Methods in Applied Mechanics and Engineering*, 361:112787, 2020.

[90] G. Lancioni and G. Royer-Carfagni. The variational approach to fracture mechanics. a practical application to the french panthéon in Paris. *Journal of Elasticity*, 95, 2009.

[91] C. J. Larsen, C. Ortner, and E. Süli. Existence of solutions to a regularized model of dynamic fracture. *Mathematical Models and Methods in Applied Sciences*, 20(7):1021–1048, 7 2010.

[92] A. A. León Baldelli, J. F. Babadjian, B. Bourdin, D. Henao, and C. Maurini. A variational model for fracture and debonding of thin films under in-plane loadings. *Journal of the Mechanics and Physics of Solids*, 70(1):320–348, 2014.

[93] A. Lew, J. E. Marsden, M. Ortiz, and M. West. Variational time integrators. *International Journal for Numerical Methods in Engineering*, 60(1):153–212, 2004.

[94] T. Li, J. J. Marigo, D. Guilbaud, and S. Potapov. Gradient damage modeling of brittle fracture in an explicit dynamics context. *International Journal for Numerical Methods in Engineering*, 108:1381–1405, 2016.

[95] D. Lin, D. Wang, S. Chen, and M. Zang. Numerical simulations of impact fracture behavior of an automotive windshield glazing: An intrinsic cohesive approach. *Composite Structures*, 186(November):79–93, 2018.

[96] Qipeng Ma, Liwei Wu, and Dan Huang. An extended peridynamic model for dynamic fracture of laminated glass considering interfacial debonding. *Composite Structures*, 290:115552, 2022.

[97] P. Mann. *Lagrangian and Hamiltonian Dynamics*. Oxford University Press, 2018.

[98] J. E. Marsden and M. West. Discrete mechanics and variational integrators. *Acta Numerica 2001*, 10:357–514, 2001.

[99] S. T. Mau. A Refined Laminated Plate Theory. *Journal of Applied Mechanics*, 40(2):606–607, 1973.

[100] A. Mesgarnejad, B. Bourdin, and M. M. Khonsari. A variational approach to the fracture of brittle thin films subject to out-of-plane loading. *Journal of the Mechanics and Physics of Solids*, 61(11):2360–2379, 2013.

[101] C. Miehe, M. Hofacker, L.-M. Schänzel, and F. Aldakheel. Phase field modeling of fracture in multi-physics problems. Part II. Coupled brittle-to-ductile failure criteria and crack propagation in thermo-elastic–plastic solids. *Computer Methods in Applied Mechanics and Engineering*, 294:486–522, 9 2015.

[102] C. Miehe, M. Hofacker, and F. Welschinger. A phase field model for rate-independent crack propagation: Robust algorithmic implementation based on operator splits. *Computer Methods in Applied Mechanics and Engineering*, 199(45-48):2765–2778, 2010.

[103] C. Miehe and S. Mauthe. Phase field modeling of fracture in multi-physics problems. Part III. Crack driving forces in hydro-poro-elasticity and hydraulic fracturing of fluid-saturated porous media. *Computer Methods in Applied Mechanics and Engineering*, 304:619–655, 6 2016.

[104] C. Miehe, L. Schänzel, and H. Ulmer. Phase field modeling of fracture in multi-physics problems. Part I. Balance of crack surface and failure criteria for brittle crack propagation in thermo-elastic solids. *Computer Methods in Applied Mechanics and Engineering*, 294:449–485, 9 2015.

[105] C. Miehe, F. Welschinger, and M. Hofacker. Thermodynamically-Consistent Phase Field Models of Fracture : Variational Principles and Multi-Field FE Implementations. *International Journal for Numerical Methods in Engineering*, 83(10):1273–1311, 2010.

[106] N. Moës, J. Dolbow, and T. Belytschko. A Finite Element Method for Crack Growth without Remeshing. *International Journal for Numerical Methods in Engineering*, 46(1):131–150, 1999.

[107] N. Moës, J. E. Dolbow, and N. Sukumar. Extended Finite Element Methods. *Encyclopedia of Computational Mechanics Second Edition*, pages 1 – 21, 2017.

[108] N. Moës, C. Stolz, P. E. Bernard, and N. Chevaugeon. A level set based model for damage growth : The thick level set approach. *International Journal for Numerical Methods in Engineering*, 86(3):358–380, 2011.

[109] N. Moës, C. Stolz, and N. Chevaugeon. Coupling local and non-local damage evolutions with the Thick Level Set model. *Advanced Modeling and Simulation in Engineering Sciences*, 1(1):1–21, 2014.

[110] I. Mohagheghian, Y. Wang, J. Zhou, L. Yu, X. Guo, Y. Yan, M. N. Charalambides, and J. P. Dear. Deformation and damage mechanisms of laminated glass windows subjected to high velocity soft impact. *International Journal of Solids and Structures*, 109:46–62, 2017.

[111] A. Muixí, A. Rodríguez-Ferran, and S. Fernández-Méndez. A hybridizable discontinuous Galerkin phase-field model for brittle fracture with adaptive refinement. *International Journal for Numerical Methods in Engineering*, (10):1–23, 2019.

[112] D. Mumford and J. Shah. Optimal approximations by piecewise smooth functions and associated variational problems. *Communications on Pure and Applied Mathematics*, 42(5):577–685, 1989.

[113] V. P. Nguyen, T. Rabczuk, S. Bordas, and M. Duflot. Meshless methods: A review and computer implementation aspects. *Mathematics and Computers in Simulation*, 79(3):763–813, 2008.

[114] Vinh Phu Nguyen and Jian-ying Wu. Modeling dynamic fracture of solids with a phase-field regularized cohesive zone model Modeling dynamic fracture of solids with a phase-field regularized cohesive zone model. (June), 2018.

[115] Jorge Nocedal and Stephen J Wright. *Numerical Optimization*. Springer, New York, NY, USA, 2e edition, 2006.

[116] R. H.J. Peerlings, R. De Borst, W. A.M. Brekelmans, and J. H.P. De Vree. Gradient enhanced damage for quasi-brittle materials. *International Journal for Numerical Methods in Engineering*, 39(19):3391–3403, 1996.

[117] Z. Pei, L. Wang, P. Wu, J. Zhang, and D. Zhou. Analytical Solution of Deformations for Two-Layer Timoshenko Beams Glued by a Viscoelastic Interlayer. *Mathematical Problems in Engineering*, 2019.

[118] J. Pelfrene, J. Kuntsche, S. Van Dam, W. Van Paepegem, and J. Schneider. Critical assessment of the post-breakage performance of blast loaded laminated glazing: Experiments and simulations. *International Journal of Impact Engineering*, 88:61–71, 2016.

[119] J. Pelfrene, S. Van Dam, and W. Van Paepegem. Numerical analysis of the peel test for characterisation of interfacial debonding in laminated glass. *International Journal of Adhesion and Adhesives*, 62:146–153, 2015.

[120] K. Pham, H. Amor, J. J. Marigo, and C. Maurini. Gradient Damage Models and Their Use to Approximate Brittle Fracture. *International Journal of Damage Mechanics*, 20(4):618–652, 2011.

[121] K H Pham, K Ravi-Chandar, and C M Landis. Experimental validation of a phase-field model for fracture. *International Journal of Fracture*, 205(1):83–101, 2017.

[122] M. S. Pigazzini, D. Kamensky, D. A.P. van Iersel, M. D. Alaydin, J. J.C. Remmers, and Y. Bazilevs. Gradient-enhanced damage modeling in Kirchhoff-Love shells: Application to isogeometric analysis of composite laminates. *Computer Methods in Applied Mechanics and Engineering*, 346:152–179, 2019.

[123] G. Pijaudier-Cabot and Z. P. Bažant. Nonlocal Damage Theory. *Journal of engineering mechanics*, 113(10):1512–1533, 1987.

[124] L. H. Poh and G. Sun. Localizing gradient damage model with decreasing interactions. *International Journal for Numerical Methods in Engineering*, 00(7):1–21, 2017.

[125] T. Pyttel, H. Liebertz, and J. Cai. Failure criterion for laminated glass under impact loading and its application in finite element simulation. *International Journal of Impact Engineering*, 38(4):252–263, 2011.

[126] E. Reissner and Y. Stavsky. Bending and Stretching of Certain Types of Heterogeneous Aeolotropic Elastic Plates. *Journal of Applied Mechanics*, 28(3):402–408, 1961.

[127] H. L. Ren, X. Y. Zhuang, C. Anitescu, and T. Rabczuk. An explicit phase field method for brittle dynamic fracture. *Computers and Structures*, 217(4):45–56, 2019.

[128] J. M. Sargado, E. Keilegavlen, I. Berre, and J. M. Nordbotten. High-accuracy phase-field models for brittle fracture based on a new family of degradation functions. *Journal of the Mechanics and Physics of Solids*, 111:458–489, 2018.

[129] J. M. Sargado, E. Keilegavlen, I. Berre, and J. M. Nordbotten. A combined finite element-finite volume framework for phase-field fracture. 2019.

[130] J. Schmidt, T. Janda, and M. Šejnoha. Prediction of pre-and post-breakage behavior of laminated glass using a phase-field damage model. *Applied Sciences*, 13(3):1708, 2023.

[131] Jaroslav Schmidt and Alena Zemanová. EULER AND EXPONENTIAL ALGORITHM IN VISCOELASTIC ANALYSES OF LAMINATED GLASS. *Acta Polytechnica CTU Proceedings*, 26:86–93, 2020.

[132] Jaroslav Schmidt, Alena Zemanová, Jan Zeman, and Michal Šejnoha. Phase-field fracture modelling of thin monolithic and laminated glass plates under quasi-static bending. *Materials*, 13(22):1–29, 11 2020.

[133] S. H. Schulze, M. Pander, K. Naumenko, and H. Altenbach. Analysis of laminated glass beams for photovoltaic applications. *International Journal of Solids and Structures*, 49(15-16):2027–2036, 2012.

[134] Y. Shen, M. Mollaali, Y. Li, W. Ma, and J. Jiang. Implementation Details for the Phase Field Approaches to Fracture. *Journal of Shanghai Jiaotong University (Science)*, 23(1):166–174, 2 2018.

[135] S. A. Silling. Reformulation of elasticity theory for discontinuities and long range forces. *Journal of the Mechanics and Physics of Solids*, 48:175–209, 2000.

[136] J. C. Simo and T. J. R. Hughes. *Interdisciplinary Applied Mathematics, Volume 7. Computational Inelasticity*, volume 79. 2004.

[137] N. Sukumar, N. Moës, B. Moran, and T. Belytschko. Extended Finite Element Method for three-dimensional crack modelling. *International Journal for Numerical Methods in Engineering*, 48(11):1549–1570, 2000.

[138] Z. Sun, G. Ma, Y. Zhang, and X. Zhuang. Cracking elements method for simulating complex crack growth. *Journal of Applied and Computational Mechanics*, 5:552 – 562, 2019.

[139] Meenu Teotia and RK Soni. Applications of finite element modelling in failure analysis of laminated glass composites: A review. *Engineering Failure Analysis*, 94:412–437, 2018.

[140] M. Timmel, S. Kolling, P. Osterrieder, and P. A. Du Bois. A finite element model for impact simulation with laminated glass. *International Journal of Impact Engineering*, 34(8):1465–1478, 2007.

[141] H. Ulmer, M. Hofacker, and C. Miehe. Phase Field Modeling of Fracture in Plates and Shells. *Pamm*, 12(1):171–172, 2012.

[142] F A Veer, P C Louter, and F P Bos. The strength of annealed, heat-strengthened and fully tempered float glass. *Fatigue & Fracture of Engineering Materials & Structures*, 32(1):18–25, 2009.

[143] J. Vignollet, S. May, R. de Borst, and C. V. Verhoosel. Phase-field models for brittle and cohesive fracture. *Meccanica*, 49(11):2587–2601, 2014.

[144] X. Wang, J. Yang, Q. Liu, Y. Zhang, and C. Zhao. A comparative study of numerical modelling techniques for the fracture of brittle materials with specific reference to glass. *Engineering Structures*, 152:493–505, 12 2017.

[145] X. Wang, J. Yang, F. Wang, Q. Liu, and H. Xu. Simulating the impact damage of laminated glass considering mixed mode delamination using FEM/DEM. *Composite Structures*, 202:1239–1252, 10 2018.

[146] Xing-er Wang, Jian Yang, Qing-feng Liu, Yang-mei Zhang, and Chenjun Zhao. A comparative study of numerical modelling techniques for the fracture of brittle materials with specific reference to glass. *Engineering Structures*, 152:493–505, 2017.

[147] T. Wick. Modified Newton methods for solving fully monolithic phase-field quasi-static brittle fracture propagation. *Computer Methods in Applied Mechanics and Engineering*, 325:577–611, 2017.

[148] S.M. Wiederhorn. Fracture Surface Energy of Glass. *Journal of the American Ceramic Society*, 52(2):99–105, 1969.

[149] M. L. Williams, R. F. Landel, and J. D. Ferry. The Temperature Dependence of Relaxation Mechanisms in Amorphous Polymers and Other Glass-forming Liquids. 77(14):3701–3707, 1955.

[150] J. Wu, V. P. Nguyen, C. T. Nguyen, D. Sutula, S. Bordas, and S. Sinaie. Phase field modelling of fracture. *Advances in Applied Mechanics*, 52, 2019.

[151] J. Y. Wu. A unified phase-field theory for the mechanics of damage and quasi-brittle failure. *Journal of the Mechanics and Physics of Solids*, 103:72–99, 2017.

[152] J. Y. Wu and V. P. Nguyen. A length scale insensitive phase-field damage model for brittle fracture. *Journal of the Mechanics and Physics of Solids*, 119:20–42, 2018.

[153] X. Xu, J. Xu, J. Chen, P. Li, B. Liu, and Y. Li. Investigation of dynamic multi-cracking behavior in PVB laminated glass plates. *International Journal of Impact Engineering*, 100:62–74, 2017.

[154] A. Zemanová. *Numerical Modeling of Laminated Glass*. PhD thesis, Czech technical university in Prague, 2014.

[155] A. ZemanovÁ, P. Hála, P. Konrád, R. Sovjak, and M. Šejnoha. Gradual Fracture of Layers in Laminated Glass Plates under Low-Velocity Impact. *Computers and Structures*, 2022. Under review.

[156] A. ZemanovÁ, P. Hála, P. Konrád, and M. Šejnoha. Smeared Fixed Crack Model for Numerical Modelling of Glass Fracture in LS-DYNA. In K. Kotrasová and E. Kormaníková, editors, *5th international conference on Structural and Physical Aspects of Construction Engineering*, Štrbské Pleso, Slovakia, 2022.

[157] A. Zemanová, J. Schmidt, and M. Šejnoha. On pre- And post-fracture behaviour of laminated glass under bending. *International Journal of Computational Methods and Experimental Measurements*, 8(3), 2020.

[158] A. Zemanová, J. Zeman, T. Janda, J. Schmidt, and M. Šejnoha. On modal analysis of laminated glass: Usability of simplified methods and enhanced effective thickness. *Composites Part B: Engineering*, 151:92–105, 2018.

[159] A. Zemanová, J. Zeman, and M. Šejnoha. Simple Numerical Model of Laminated Glass Beams. *Acta Polytechnica*, 48(6):22–26, 2008.

[160] A. Zemanová, J. Zeman, and M. Šejnoha. Numerical model of elastic laminated glass beams under finite strain. *Archives of Civil and Mechanical Engineering*, 14(4):734–744, 2014.

[161] A. Zemanová, J. Zeman, and M. Šejnoha. Finite element model based on refined plate theories for laminated glass units. *Latin American Journal of Solids and Structures*, 12(6):1158–1181, 2015.

[162] A. Zemanová, J. Zeman, and M. Šejnoha. Comparison of viscoelastic finite element models for laminated glass beams. *International Journal of Mechanical Sciences*, 131:380–395, 2017.

[163] Xue Zhang, Chet Vignes, Scott W Sloan, and Daichao Sheng. Numerical evaluation of the phase-field model for brittle fracture with emphasis on the length scale. *Computational Mechanics*, 59(5):737–752, 2017.

[164] Y. Zhang and X. Zhuang. Cracking elements method for dynamic brittle fracture. *Theoretical and Applied Fracture Mechanics*, 102:1–9, 2019.

[165] S. Zhao, L. R. Dharani, L. Chai, and S. D. Barbat. Analysis of damage in laminated automotive glazing subjected to simulated head impact. *Engineering Failure Analysis*, 13(4):582–597, 6 2006.